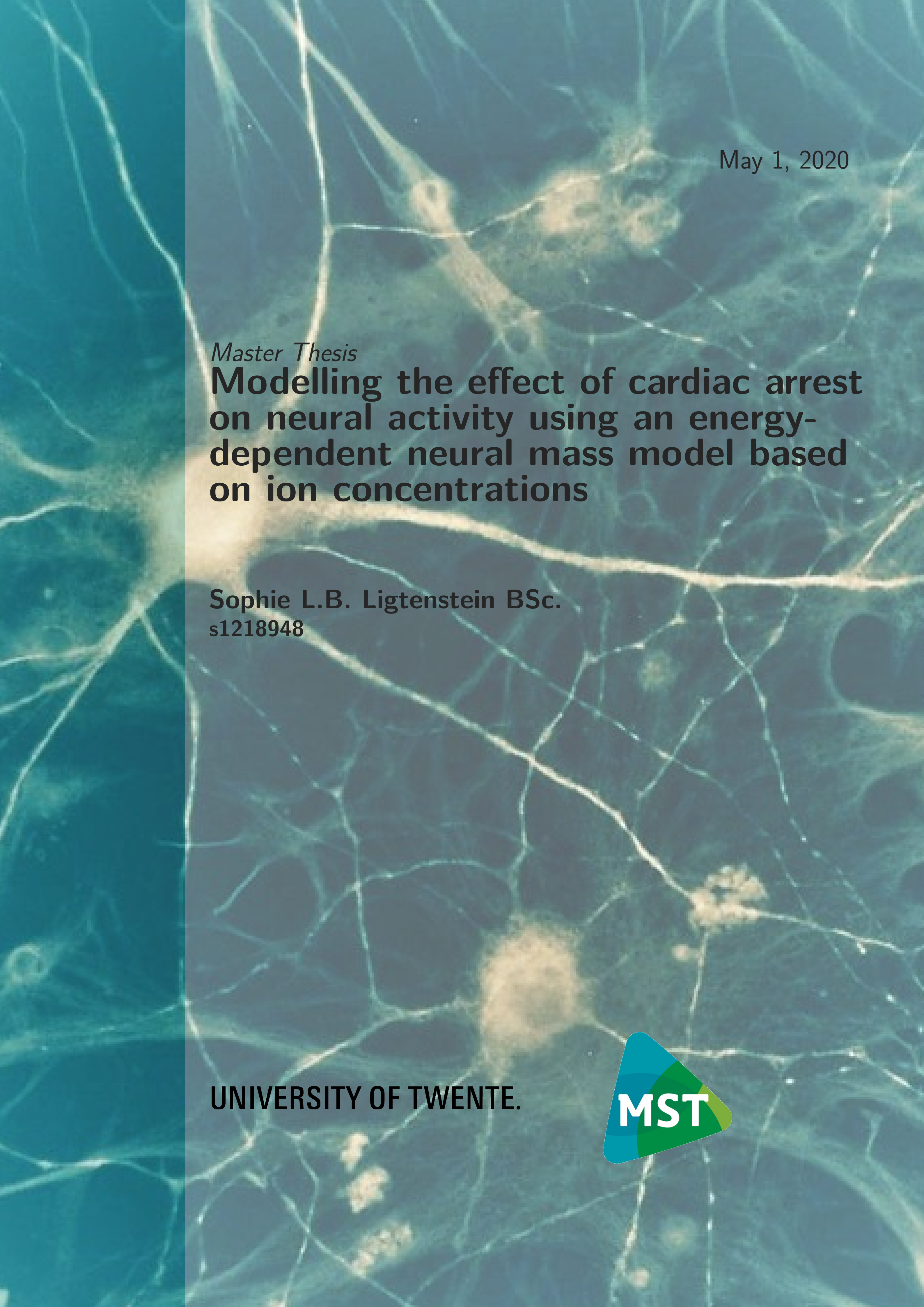

May 1, 2020

Master Thesis

Modelling the effect of cardiac arrest on neural activity using an energy-dependent neural mass model based on ion concentrations

Sophie L.B. Ligtenstein BSc.
s1218948

UNIVERSITY OF TWENTE.

MST

To obtain the master degrees in Applied Mathematics and Technical Medicine

University of Twente
Faculty of Electrical Engineering, Mathematics and Computer Science
Master's programme: Applied Mathematics
Specialisation: Systems Theory, Applied Analysis and Computational Science
Chair: Applied Analysis

Faculty of Science and Technology
Master's programme: Technical Medicine
Track: Medical Sensing and Stimulation

Clinical Neurophysiology Group

Medisch Spectrum Twente
Department of Neurology and Clinical Neurophysiology

Graduation Committee

Prof. dr. ir. M.J.A.M. van Putten	Clinical Neurophysiology Group, MST
Dr. H.G.E. Meijer	Applied Analysis
Prof. dr. S.A. van Gils	Applied Analysis
Drs. B.J.C.C. Hessink-Sweep	Technical Medicine
Dr. M.C. Tjepkema-Cloostermans	Clinical Neurophysiology Group, MST
Dr. ir. G. Meinsma	Hybrid Systems (University of Twente)

Graduation Date
May 1, 2020

Thanks to Dr. M. Frega for providing the image used on the title page. The image shows inhibitory and excitatory neurons during hypoxia.

Abstract

Background Significant changes in rhythm are visible on electroencephalography (EEG) recordings during cardiac arrest. Our aim is to improve the understanding of underlying pathophysiological mechanisms causing these EEG changes using computational modelling. To couple the computational outcomes to clinical EEG recordings, we use a neural mass model. Hence, the primary objective of this study is to construct and analyse an energy-dependent neural mass model based on ion concentrations to examine the effect of energy depletion during cardiac arrest on neural activity.

Methods We constructed an ion-based neural mass model comprising an excitatory and inhibitory neural population and excitatory external input. Energy (adenosine triphosphate (ATP)) dependency was accomplished by including ATP-dependent Na^+-K^+-ATPase (NKA) and an adapted firing rate function for the two neural populations. In addition, a network of coupled spiking single cells was constructed to which the outcome of the neural mass model was compared. NKAs were included in this second model as well, offering the possibility to tune the strength of these pumps during simulation. We studied the responses of both models to an excitatory external input, to different levels of ATP deprivation and to recovery after deprivation and restoration of the ATP supply. We also investigated a mechanism to promote this recovery. Furthermore, the outcome of both models was compared to the EEG signal of a patient recorded during cardiac arrest. Lastly, both models were analysed to gain more insight into the dynamic behaviour of the models.

Results Periodic behaviour is observed in both models as a response to transient external input indicating normal behaviour of the models under physiological conditions. The strength of the external input determines the qualitative dynamics of the models. The response of the models to ATP deprivation depends on the depth of this deprivation. ATP levels below a critical point lead to depolarization of the membrane potential, which is visible on the simulated EEG signals as a large slow wave. Based on the real EEG signal, the hypothesis was to observe slowing of the simulated EEG signals during ATP deprivation. However, the frequency of the periodic behaviour initially increased in both models. In case of total ATP cessation, this was followed by EEG suppression. Besides, the membrane potentials of the network model recovered after ATP deprivation only if voltage-gated sodium channels were blocked. The membrane potentials of the neural mass model recovered as soon as ATP levels increased, even without blocking voltage-gated sodium channels.

Conclusion The newly constructed models provide a unique extension in the field of computational neuroscience by including NKAs and ATP dependency at a macrosopic level. Both models show similar behaviour as other computational models. However, complete ATP cessation results in changes of the EEG rhythm in both models which do not correspond to the changes seen in the real EEG. We recommend further research to extend the models e.g. by incorporating more ATP-dependent processes, to improve the understanding of the EEG changes visible during cardiac arrest. Although there is still a gap between the models and clinical use, this study provides a starting point for future models to investigate and understand pathophysiological mechanisms of neural diseases caused by ATP deprivation and/or imbalance of ion concentrations.

Keywords Cardiac arrest, ATP, Na^+-K^+-ATPase, neural mass model, ion-based, Gibbs-Donnan, membrane depolarization

Preface

Before you lies my master thesis entitled ‘modelling the effect of cardiac arrest on neural activity using an energy-dependent neural mass model based on ion concentrations’. I conducted this research to obtain my MSc title in both Technical Medicine and Applied Mathematics at the University of Twente. I worked at the Neurology and Clinical Neurophysiology department of Medisch Spectrum Twente, the Applied Analysis group of the University of Twente and the Clinical Neurophysiology group of the University of Twente. During the past year, I created a so-called neural mass model to gain insight into the effects of a cardiac arrest on neural activity.

This report marks the end of my time as a student which started back in August 2011 when I moved all the way from the west to the east of the Netherlands. The past eight and a half years, I have experienced a lot of different and exciting things! I joined student association Audentis and sorority Spooky, did a fulltime board year at the Student Union, lived in Enschede, Groningen, Amsterdam, Boston and Almelo, decided to fulfill my desire for more math by enrolling in the master programme of Applied Mathematics, prepared over 1000 high school students for their final math exam, travelled around the world, and much more. Although I gave myself a hard time once in a while as I did not always have confidence in my own abilities, I look back on a wonderful time and I am proud of my achievements!

I would like to thank my supervisors for their guidance and support. Hil, thank you for sharing your broad knowledge on computational modelling with me and teaching me how to create my own model(s). Michel, thank you for welcoming me into the Clinical Neurophysiology group and supporting my desire to combine Technical Medicine and Applied Mathematics. Marleen, thank you for all your advice and food for thought in both the technical and medical field. Stephan, thank you for welcoming me into the Applied Analysis group and responding to my wish to combine both masters as well. Bregje, and Paul, thank you for guiding me the past two and a half year, while offering me a listening ear and teaching me valuable life lessons. Gjerrit, thank you for joining the committee as the independent member. Also, I would like to mention Manu and Jeannette. Thank you both for your time and advice and sharing your thoughts on my model and research.

Moreover, there are a lot more people without whom I would not be where I am today. Thank you to all my office mates for the (lunch)breaks, ‘bakkies’ and laughs. Tanja, thank you for all your heart-warming advice and the chats we have had (plus providing me my weekly serving of liquorice). Wietske, thank you for holding my hand while I jumped into the mathematical roller coaster, and being my study buddy and dear friend. I would also like to thank my friends, in particular those from Spooky, for all the fun we have had, always supporting each other and travelling with me to numerous places to discover the world. I cannot wait to see and hug you again after this corona crisis and I am looking forward to making new memories with you! And last but not least, a big shout out to my parents and boyfriend. Mum and dad, thank you for your endless support and patience, all your help and advice and always being there for me. I cannot thank you enough in words, so I promise I will thank you with lots of homemade cakes and chocolates. Bram, thank you for always having faith in me, making me laugh and teaching me how to see the positive side of everything.

I hope you enjoy your reading!

Sophie

List of Abbreviations

		Introduced at page
AMPA	α-amino-3-hydroxy-5-methyl-4-isoxazolepropionic acid	17
ATP	Adenosine triphosphate	3
CBF	Cerebral blood flow	3
DE	Differential equation	65
ECS	Extracellular space	3
EEG	Electroencephalography	1
EPSC	Excitatory postsynaptic current	23
EPSP	Excitatory postsynaptic potential	12
GABA	γ-aminobutyric acid	17
GD	Gibbs-Donnan	4
GHK	Goldman-Hodgkin-Katz	25
HH	Hodgkin-Huxley	8
ICS	Intracellular space	17
IPSC	Inhibitory postsynaptic current	23
IPSP	Inhibitory postsynaptic potential	12
NKA	Na^+-K^+-ATPase (= sodium-potassium pump)	1
NMM	Neural mass model	1
NVC	Neurovascular coupling	48
ODE	Ordinary differential equation	8
OGD	Oxygen and glucose deprivation	1
PSC	Postsynaptic current	29
PSP	Postsynaptic potential	29
SN	Saddle-node	10

List of Figures

		Page
Figure 2.1	Relation between CBF, EEG and cellular response	5
Figure 3.1	Equivalent circuit representation of a cell membrane	7
Figure 3.2	Dynamics of Hodgkin-Huxley model	9
Figure 3.3	EEG recordings of nine rats during and after decapitation	9
Figure 3.4	Mean membrane potential and corresponding EEG signal	10
Figure 3.5	Bifurcation diagram of NKA strength, membrane potential and neuronal volume	11
Figure 3.6	Wilson-Cowan model	13
Figure 3.7	Jansen-Rit model	14
Figure 3.8	Liley model	15
Figure 4.1	Schematic overview of a representative neuron	18
Figure 4.2	Example overview of network model of coupled spiking single cells	19
Figure 4.3	Overview of ATP-dependent neural mass model	24
Figure 4.4	Overview of constructing F(I)-curve	28
Figure 4.5	Quality of threshold fitting	28
Figure 4.6	Examples of influence of E_{Na} and E_K on F(I)-curve	29
Figure 5.1	Response of network model to external input	36
Figure 5.2	Response of NMM to external input	36
Figure 5.3	Response of network model to ATP depletion	38
Figure 5.4	Response of NMM to ATP depletion	38
Figure 5.5	Response of network model to external input during ATP deprivation	39
Figure 5.6	Response of NMM to external input during ATP deprivation	39
Figure 5.7	EEG recording of a (second) cardiac arrest	40
Figure 5.8	Effect of complete ATP depletion on EEG frequency	41

Page

Figure 5.9 Recovery of network model after complete ATP depletion 42

Figure 5.10 Recovery of NMM after complete ATP depletion 42

Figure 5.11 Response frequency to external input 43

Figure 5.12 Bifurcation diagram of ATP-dependent NMM with f_{ext} a free parameter 44

Figure D.1 Structure of neuron 63

Figure E.1 Schematic overview of the conversion operators of a neural mass model 65

Figure E.2 Examples of both conversion operators of a neural mass model 66

List of Tables

Page

Table 4.1 Overview of values used for conducting tests with network of single cells 33

Table 4.2 Overview of values used for conducting test with NMM 33

Table A.1 Overview of model parameters, symbols and values of network of single cells 57

Table A.2 Overview of model parameters, symbols and values of NMM 58

Table A.3 Coefficients of polynomials I_{th}, κ and I_{th2} 59

Table B.1 Variations per neuron relative to mean applied current and mean pump strength 60

Table D.1 Ion concentrations and Nernst equilibrium potentials 63

Contents

1 Introduction **1**

2 Clinical Background **3**
2.1 Cardiac arrest and neural consequences **3**
2.2 Electroencephalography **4**

3 Computational modelling of neurons and neural networks **7**
3.1 Single cell models **7**
  3.1.1 Hodgkin-Huxley model 8
  3.1.2 Modelling 'Wave of Death' 9
  3.1.3 Modelling cytotoxic cell swelling 10
3.2 Neural mass models **11**
  3.2.1 Overview of neural mass models 12
  3.2.2 ATP-dependent neural mass model 14

4 Methods **17**
4.1 Cell biology **17**
4.2 Network of coupled spiking single cells **17**
  4.2.1 Model assumptions, choices and requirements 18
  4.2.2 Model components 19
  4.2.3 Model overview 22
4.3 Neural mass model based on ion concentrations **24**
  4.3.1 Model assumptions, choices and requirements 24
  4.3.2 Model components 24
  4.3.3 Model overview 31
4.4 Model validation **32**

5 Results **35**
5.1 External input **35**
5.2 ATP depletion **37**
5.3 External input plus ATP depletion **37**
5.4 Recovery after ATP depletion **40**
5.5 Model analysis **43**

6 Discussion **45**
6.1 Limitations **47**
6.2 Clinical relevance **48**
6.3 Recommendations **48**

7 Conclusion **51**

Bibliography **53**

A Model Parameters **57**

B Additional information: network of coupled spiking single cells **60**

C Additional information: ATP-dependent neural mass model **61**

D Additional background information: cell biology **62**
D.1 Introduction to human brain and neurons **62**
D.2 Nernst potentials **62**
D.3 Action potentials **63**
D.4 Neurotransmitters **64**
D.5 Types of neurons **64**

E General principles of neural mass model **65**

1 | Introduction

Cardiac arrest is a catastrophic event causing abrupt cessation in delivery of oxygen and glucose affecting the human brain almost immediately[81]. Inadequate supply of oxygen and glucose can lead to severe damage of brain tissue and a state of unconsciousness called postanoxic coma[48]. Incidence rate of out-of-hospital cardiac arrest in Europe is 84 per 100,000 persons per year. Approximately 50% of the patients in postanoxic coma never regain consciousness due to severe brain damage[22,64].

Hypoxia results in reversible, and ultimately irreversible, damage to neurons. The outcome depends on the duration and severity of oxygen and glucose deprivation (OGD) leading to insufficient energy supply to the brain[47]. During cardiac arrest, significant rhythmic changes are visible on electroencephalography (EEG) recordings. Nowadays, physicians use EEG more frequently to assist in outcome prediction for comatose patients after cardiac arrest[72]. For approximately 50% of the patients, a reliable prediction based on visual assessment of the EEG by experienced clinical neurophysiologist cannot be made[68]. Up to now, neural processes underlying the EEG changes observable during energy depletion caused by cardiac arrest, remain largely unknown. A better understanding of underlying pathophysiological mechanisms can contribute to an improved understanding of these changes and an improved outcome prediction. Enlarged pathophysiological knowledge can also be of added value for more targeted treatment of patients suffering cardiac arrest.

Gaining more pathophysiological knowledge can be accomplished using neural mass models (NMMs). These computational models allow for simulation and investigation of macrosopic neural behaviour, which is reflected by EEG signals. Previously, a NMM was constructed by Ruijter et al. (2017) to relate neural dynamics in the postanoxic brain to EEG observations[58]. Although multiple computational models exist to investigate the immediate effects of energy deprivation on a microscopic scale, no NMM describing these effects at a macroscopic level has been constructed yet[17,79]. Such a macroscopic model can link the computational outcomes to clinical EEG results. Moreover, diminished levels of energy cause malfunctioning of multiple energy dependent processes like Na^+-K^+-ATPase (NKA), which, in turn, affects neural activity. It is important to keep track of ion concentrations to study the resulting effects. To the best of our knowlegde, no NMM exists that comprises these ion concentrations. The primary objective of this study is to construct and analyse an energy-dependent NMM based on ion concentrations to examine the effect of energy depletion during cardiac arrest on neural activity. Based on clinical EEG results, we expect the simulated EEG signals to show slowing of the signal frequencies during energy depletion[20].

Chapters 2 and 3 provide clinical and mathematical background information. Our energy-dependent NMM is introduced in Chapter 4. Also, we elaborate on an additional network model consisting of coupled spiking single cells. Both models are described in detail in this chapter. The results of the models are presented in Chapter 5. In Chapter 6, results, limitations and clinical relevance of this study are discussed and recommendations for further research are given. We finish with our conclusion of this study in Chapter 7.

2 | Clinical Background

The human brain consumes almost 20% of the total body oxygen, although its weight accounts for only 2% of the total body weight[56]. As our brain highly depends on oxygen to maintain normal function, global anoxia can cause severe brain damage. This chapter elaborates on cardiac arrest and neural consequences of this event. In addition, information about EEG and EEG changes visible during cardiac arrest is provided. Furthermore, Appendix D contains more background information about cell biological topics relevant for this research.

2.1 Cardiac arrest and neural consequences

Cardiac arrest is defined as functional cardiac mechanical activity loss together with an absence of systemic circulation[48]. There are several causes for an unexpected cardiac arrest like sudden failure of the heart due to infarction, cardiac arrhythmia, acute circulatory obstruction and cardiovascular rupture[39]. Yearly, approximately 8000 cases of out-of-hospital cardiac arrest occur in the Netherlands[24]. Even after successful return of spontaneous circulation, a majority of the patients remain comatose[64].

Postanoxic encephalopathy is one of the main determinants of the outcome after cardiac arrest and is associated with considerable neurological damage[61]. Cerebral blood flow (CBF) provides oxygen and glucose to neurons. The mitochondria of the neurons use this oxygen and glucose for the production of adenosine triphosphate (ATP), which is the primary energy carrier in the human body. OGD following cardiac arrest therefore inevitably results in a decrease of cellular ATP levels in the brain[78]. Levels of ATP of 95% of baseline value can still be provided in early stages of ischemia[35]. ATP buffers are spent in five minutes leading to ATP levels dropping below 10% of baseline and eventually becoming 0%.

Multiple neuronal processes require ATP to function properly. Experimental studies show that mild to moderate hypoxia results in synaptic failure due to presynaptic and/or postsynaptic failure[27]. A shortage of ATP also diminishes the strength of NKAs. The primary role of these enzymes, located in the membrane of neurons, is to maintain specific ion gradients of sodium (Na^+) and potassium (K^+). If hypoxia persists and perfusion rates drop to approximately 18 mL/100g/min, NKAs can no longer maintain ion gradients[20,62]. Neurons reach their threshold potential resulting in anoxic oscillations and release of large amounts of neurotransmitters, which is toxic in high concentrations. Furthermore, the loss of control of influx of sodium and efflux of potassium can lead to cell swelling[25]. Especially the ion exchanger SLC26A11 is thought to play a significant role in this neuronal swelling. It is highly expressed in cortical neurons of the central nervous system and acts as a voltage-gated chloride (Cl^-) channel. Opening of this channel occurs when the membrane potential depolarizes. The efflux of potassium can, to some extend, compensate the osmotic imbalance caused by the inflow of sodium. However, the influx of chloride cannot be counteracted as the anionic intracellular environment mainly consists of impermeable anions. The resulting increase of the intracellular osmolarity leads to water entering the cell[59]. The extracellular space (ECS) is now depleted from sodium, chloride and water and the gradients of these molecules across the capillary membranes change. As a result, constituents from the intravascular space enter the brain and the neuronal tissue swells[40]. This so-called cerebral edema is observed in some patients and considered to indicate severe brain injury[18].

If all energy-dependent (active) ion transport is absent, a new distribution of the diffusible ions takes place and the membrane potential of neurons evolves to another equilibrium potential. This so-called Gibbs-Donnan (GD) equilibrium is independent of specific ion permeabilities. The Nernst potentials of all permeant ions equal the (new) membrane potential. The GD equilibrium is usually around -20mV. This is due to the presence of impermeant charged ions[17,36,63].

Although a decrease of ATP affects multiple processes in the brain, we decided to focus on the effect of ATP deprivation on NKAs and the resulting effects of failure of these pumps. The NKA is an electrogenic ion transporter of sodium and potassium. Ion gradients of sodium and potassium are disturbed during an action potential as there is influx of sodium and efflux of potassium. The NKA consumes ATP while restoring the gradients of these ions[11]. At the cost of one ATP molecule, the pump exports three sodium ions and imports two potassium ions per pump cycle, thereby generating a net transmembrane current[17]. In physiological state, the KCl cotransporter KCC2 maintains low intracellular chloride concentrations[49]. The protein is expressed throughout the central nervous system. This transporter uses the potassium gradient generated by NKA to extrude chloride from the neurons. Problems with NKAs thus affect KCC2 as well. The extracellular potassium concentration can influence the working direction of the symporter. The transport of both potassium and chloride can be reversed by a moderate or high increase of the potassium concentration in the ECS[10].

2.2 Electroencephalography

EEG measures the electrical brain activity. The EEG signal shows waveforms of several μV reflecting the weighted sum of dendritic currents. These currents originate from cortical pyramidal cells close to the EEG electrodes on the scalp. EEG has multiple clinical applications such as detection of seizures, investigation of sleep disorders and monitoring coma and brain death. Changes in the EEG rhythm are closely connected to levels of CBF. The relation between CBF, EEG and cellular response was summarized by Foreman et al. (2012) (See Figure 2.1)[20]. During cerebral ischemia, loss of faster frequencies can be observed on the EEG. When CBF levels drop below 18 mL/100g/min, the EEG shows a gradual increase of slower frequencies. Below this ischemic threshold, NKAs begin to fail which results in loss of membrane gradients and the consequences of this.

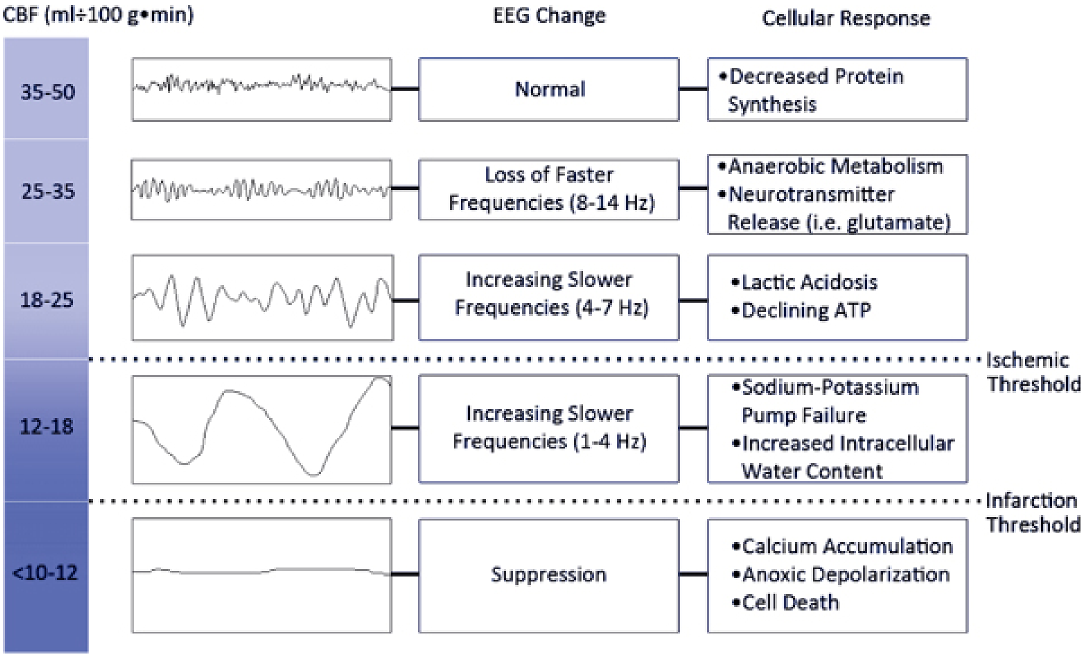
CBF (ml÷100 g•min)
EEG Change
Cellular Response
35-50
Normal
•Decreased Protein Synthesis
25-35
Loss of Faster Frequencies (8-14 Hz)
•Anaerobic Metabolism
•Neurotransmitter Release (i.e. glutamate)
18-25
Increasing Slower Frequencies (4-7 Hz)
•Lactic Acidosis
•Declining ATP
Ischemic Threshold
12-18
Increasing Slower Frequencies (1-4 Hz)
•Sodium-Potassium Pump Failure
•Increased Intracellular Water Content
Infarction Threshold
<10-12
Suppression
•Calcium Accumulation
•Anoxic Depolarization
•Cell Death

Figure 2.1: **Relation between CBF, EEG and cellular responses.** EEG changes are observed when CBF declines, leading to different cellular responses. CBF levels below the ischemic threshold of approximately 18 mL/100 g/min result in failure of NKAs. Figure from Foreman et al. (2012)[20].

3 | Computational modelling of neurons and neural networks

Computational models shed light on fundamental mechanisms underlying neural processes. We investigate multiple existing computational models to gain a better understanding of the models suitable as a base for this study. These computational models exist at different spatial scales. We considered several single cell models (microscopic scale) and NMMs (macroscopic scale) relevant for our research and provide more information about these models in this chapter. Single cell models are detailed and focus on the level of information exchange between single neurons, while NMM describe brain dynamics at the scale of large populations of neurons.

3.1 Single cell models

A range of single cell models describing the spiking behaviour and dynamics of single cortical neurons, exist. We aim to mimic the effect of ATP depletion on the brain, for which a so-called conductance based model is preferable. Such a model is based on an equivalent circuit representation of a cell membrane as shown in Figure 3.1. Conductors represent ion channels, batteries represent concentration gradients of ions, and capacitors represent the ability of cell membranes to store charge. A conductance-based model is chosen when a biophysically detailed model is desired. A drawback of this type of model is the intrinsic complexity making it harder to analyze the model[31].

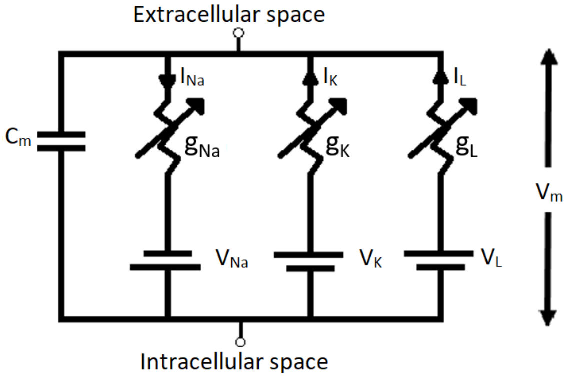

Figure 3.1: **Equivalent circuit representation of a cell membrane**. A conductance-based model is based on an equivalent circuit representation. The circuit consists of membrane capacitance C_m, membrane potential V_m, conductance g_X of ion X, ion current I_X through ion channels of ion X and equilibrium potential V_X of ion X with $X \in \{Na^+, K^+\}$. I_L is the leak current and g_L and V_L are the corresponding conductance and equilibrium potential, respectively. Conductors represent ion channels, batteries represent concentration gradients of ions, and the capacitor represents the ability of the cell membrane to store charge.

As a start, this section discusses the model of Hodgkin and Huxley. This is a highly acclaimed example of a conductance-based model and often serves as a base for other models such as those of Zandt et al. (2011)[79] and Dijkstra et al. (2016)[17]. These two models focus on the effect of ATP depletion on the behaviour of a single cell. Secondly, we provide more information about these two models as well and come back to this at the end of Section 3.2.

3.1.1 Hodgkin-Huxley model

The Hodgkin-Huxley (HH) model is a computation model describing the voltage changes across a single cell membrane which can result in the generation of action potentials. Three major currents are incorporated in the HH model: voltage-gated sodium current I_{Na}, voltage-gated potassium current I_K and leak current I_L, mostly representing chloride[31]. The following coupled ordinary differential equations (ODEs) describe the dynamics of membrane potential V_m:

$$\begin{aligned}
C_m \frac{dV_m}{dt} &= I_m - I_K - I_{Na} - I_L, \\
&= I_m - g_K n^4 (V_m - V_K) - g_{Na} m^3 h (V_m - V_{Na}) - g_L (V_m - V_L), \\
\frac{dn}{dt} &= \alpha_n(V_m)(1-n) - \beta_n(V_m)n, \\
\frac{dm}{dt} &= \alpha_m(V_m)(1-m) - \beta_m(V_m)m, \\
\frac{dh}{dt} &= \alpha_h(V_m)(1-h) - \beta_h(V_m)h,
\end{aligned}$$

where g_X and V_X denote the maximal conductance and Nernst potential of ion X, respectively, with $X \in \{Na^+, K^+\}$. Furthermore, there is a maximum leak conductance g_L and equilibrium potential of the leak population V_L, activation variable n for potassium, activation variable m for sodium, inactivation variable h of sodium and voltage-dependent rate constants α_z and β_z with $z \in \{n, m, h\}$[26,31]. Equations for α_z and β_z are provided in Chapter 4. I_{Na} is transient as the corresponding channel contains both activation and inactivation gates. Potassium channels do not have inactivation gates. This result in a persistent I_K[31].

The HH model allows for simulation of action potentials. A constant input current $I(t) = I_0$ for t $>$ 0 can be applied to the model. Spiking activity can be observed when I_0 exceeds a specific threshold current I_{th}. This critical value is the minimal current necessary to reach a depolarization threshold. However, it should be kept in mind that the HH model can be a bistable model. A bistable model has two stable coexisting attractors (also called equilibrium states or stable solutions). The initial values of the system determine if the HH model exhibits bistability because trajectories starting from different initial conditions are attracted by different solutions of the system[8]. Figure 3.2 shows examples of the HH model dynamics.

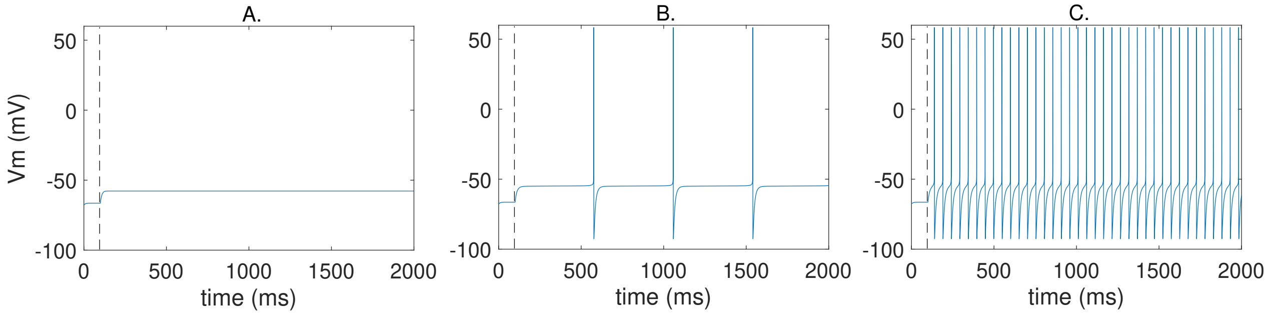

Figure 3.2: **Dynamics of Hodgkin-Huxley model.** A continuous external input current I is provided to the model starting at $t = 200$ ms (dashed grey line). Action potentials are generated when input current I exceeds threshold current I_{th}. A. $I < I_{th}$ and no action potentials are generated. B. $I \approx I_{th}$ and a spike train is observed. Each action potential is followed by an absolute and relative refractory period. C. $I > I_{th}$ leads to rhythmic generation of action potentials.

3.1.2 Modelling 'Wave of Death'

Zandt et al. (2011) simulated a high amplitude slow brain wave as observed in the EEG of rats (Figure 3.3)[79]. As this pattern occurs one minute following decapitation, potentially reflecting the synchronous death of neurons, it is called the 'Wave of Death'. The model is based on the HH model. Dynamics of sodium and potassium channels are incorporated, as well as a leak current for sodium, potassium and chloride. There is preservation of the total amount of sodium in the model. The extracellular potassium concentration changes due to buffering by glial cells and diffusion from and into the capillaries. Chloride concentrations are kept constant under physiological conditions, but not under pathophysiological conditions. Furthermore, the NKA maintains ion homeostasis. OGD is simulated by setting the pump current to zero and stopping glial uptake and diffusion of potassium simultaneously. ATP dependency of the NKA is not modelled explicitly.

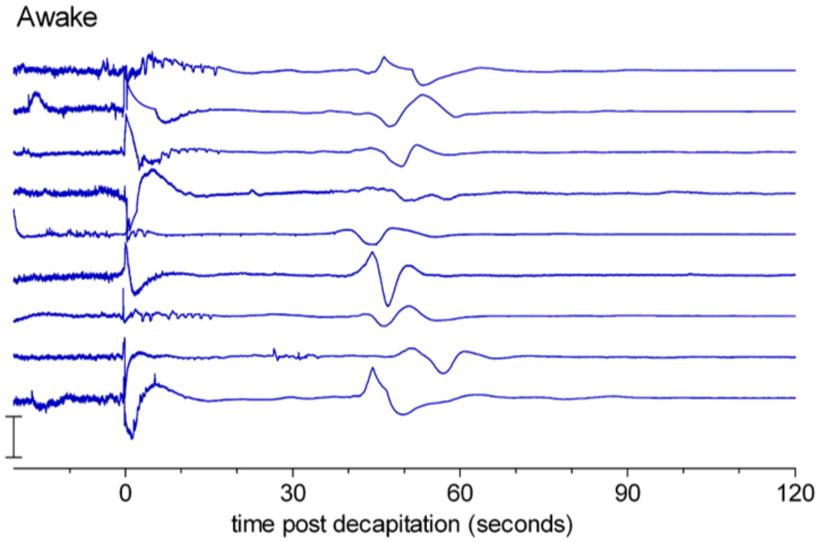

Figure 3.3: **EEG recordings of nine rats during and after decapitation.** The EEG is recorded from 10 seconds before decapitation till 120 seconds after. The 'Wave of Death' is visible as a large, slow wave between 40 and 60 seconds post decapitation. Movements artifacts due to decapitation result in amplitude changes at $t = 0$. Figure adapted from Van Rijn et al. (2011)[73].

Interaction between neurons is important in the determination of neural behaviour. Therefore, modelling a realistic EEG signal is usually not possible with only one single cell model. However, the neurons receive no input from other neurons as synaptic transmission stops in the model of Zandt et al. (2011) and so, it is stated that the dynamics can be simulated by a single cell, assuming that most neurons show similar behaviour as the modelled one[79]. In this case, the mean membrane potential serves as a proxy for the raw EEG signal as shown in Figure 3.4. Zandt et al. (2011) showed that a sudden depolarization of the membrane voltage is indeed visible after severe OGD. However, this depolarization does not necessarily imply irreversible damage or neuronal death. Thus, it is disputable if the name, 'Wave of Death', is appropriate as restoring the ATP levels can revive cell dynamics[79]. ATP reserves are not incorporated in the model. Including ATP reserves probably would have led to a delayed onset of the simulated wave.

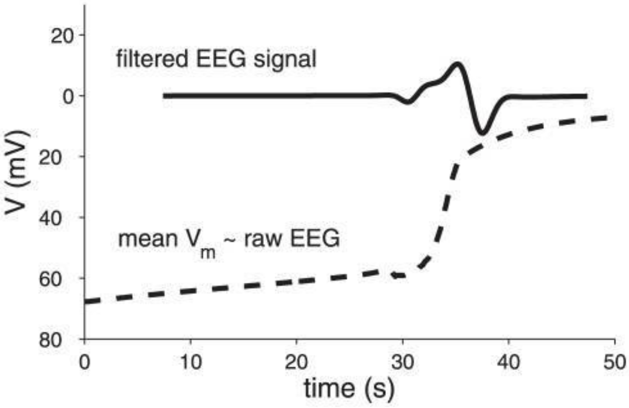

Figure 3.4: **Mean membrane potential and corresponding EEG signal**. The dashed line shows the mean membrane potential V. A flat distribution with a width of 300 ms was chosen. Applying a second order Butterworth filter with a cut-off frequency of 0.1 Hz leads to the EEG signal shown by the solid line. Figure from Zandt et al. (2011)[79].

3.1.3 Modelling cytotoxic cell swelling

Tissue swelling, following swelling of neurons, leads to cerebral cytotoxic edema. This happens as a result of OGD as described in Section 2.1. Dijkstra et al. (2016) developed a biophysical model to simulate cytotoxic cell swelling and to study key determinants[17]. The model consists of one neural compartment surrounded by an infinite ECS. Intracellular chloride levels and remaining activity of the NKA turn out to play a crucial role in the emergence of cytotoxic edema. Cell volume increases enormously when the strength of the NKA exceeds a critical value. This leads to a GD equilibrium from which recovery of the neuron is not possible. Transitioning from rest to GD equilibrium follows the shutdown of the NKA. Cytotoxic edema can only be reversed by restoration of energy together with blocking the voltage-gated sodium channels, leading to functional recovery[17].

The dependence of the model on the strength of the NKA is studied using bifurcation analysis. A bifurcation of a dynamical system is a qualitative change in dynamical behaviour of the system, caused by varying a single or multiple parameter(s). The critical value of the pump strength turns out to be approximately 65% of the initial pump strength. Further decreasing of the pump strength leads to disappearance of the physiological state via a so-called saddle-node (SN) bifurcation. A stable equilibrium collides with an unstable equilibrium at a SN bifurcation. Near such a bifurcation, sudden and huge shifts in the systems behaviour can occur as a response to small changes. Figure 3.5A shows the corresponding bifurcation diagram. Furthermore, the size of the neuron has a high dependency on the strength of the pump when the cell converges to the pathological equilibrium. A change of the strength leads to major differences in the level of cell swelling. The pathological state is stable for pump strengths below 185% of baseline strength. A subcritical Hopf bifurcation occurs at approximately 185%. The system loses its stability and returns to the physiological state at this point (Figure 3.5B)[17].

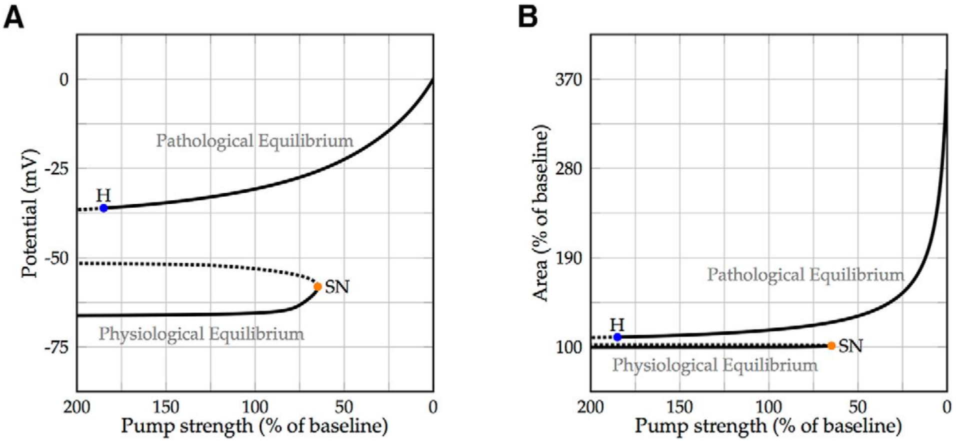

Figure 3.5: **Bifurcation diagram of NKA strength, membrane potential and neuronal volume.** The strength of the NKA was taken as the free parameter. The solid lines indicate stable equilibria and the dotted lines indicate unstable equilibria. A. The physiological resting state is lost via a saddle-node bifurcation (SN, orange) when the pump strength is approximately 65% of its baseline strength. Further decrease of the pump strength leads to convergence of the cell to a depolarized GD equilibrium. The pathological state is stable for pump strengths below 185% of the baseline strength. At approximately 185%, there is a subcritical Hopf bifurcation (H, blue) and the system loses stability. B. When the cell is in the physiological resting state, its volume is almost constant regardless of pump strength. However, when the cell converges to the pathological equilibrium, changes in the pump strength lead to large differences in cell volume. Figure from Dijkstra et al. (2016)[17].

3.2 Neural mass models

The brain consists of a large number of neurons. We would encounter several difficulties when trying to accurately capture the behaviour of a population of neurons by simulating each neuron individually. First, the model would be computationally very expensive. Secondly, a high number of parameters would be involved in the model. Analyzing the influence of the parameters and setting the initial values is, therefore, very complicated[21]. An alternative is to model the average behaviour of large populations of neurons with a NMM. The principle behind these models is comparable to how EEG measures the brain: EEG focuses on voltage measurements of synchronously firing populations of neurons in the brain (called neural masses). This allows us to gain more insight into the communication between different brain regions[4]. An advantage of this approach is the possibility to greatly reduce the dimensionality of the model. An important step in this reduction in NMMs is replacement of all individual spikes by a population firing rate. This macrosopic variable reflects the average spiking behaviour of all neurons within a population[70]. A limitation of current NMMs is the absence of details regarding underlying neurophysiological processes.

Separate masses describing multiple neural populations are the building blocks of NMMs. The masses are coupled to each other to simulate the behaviour of larger brain structures. Each mass within a NMM has an average membrane potential $V(t)$, which is the state variable. This average membrane potential results from different inputs received by the neural mass. These inputs are described as average pulse densities (mean pre-synaptic firing rate) and result from external inputs and other neural masses. Hence, the output of a neural mass is also an average pulse density, i.e. mean firing rate. With a NMM we focus on synaptic activity at a large scale. A NMM can be seen as a slow filter overlying fast dynamics (e.g. action potentials of individual neurons). Capturing fast dynamics with a NMM is therefore not possible.

The next section starts with a brief overview followed by a description of the NMMs that we considered as a base for our own NMM. The section finishes with a summary of the most important aspects of the existing NMMs for the construction of an ATP-dependent NMM. Appendix E contains more information about the general principles of a NMM.

3.2.1 Overview of neural mass models

NMMs were introduced in the 1970s. Nowadays, a wide variety of NMMs exists. The models are used to examine large-scale brain dynamics in health and disease. The model of Wilson and Cowan (1972) is seen as one of the most influential NMMs. It describes the activity of an excitatory population coupled to an inhibitory one[76]. In 1974, Lopes da Silva et al. developed an initial model to simulate α-rhythms (8 - 13 Hz)[43]. This work was followed by the Zetterberg model (1978) which gained more attention thanks to Jansen and Rit[32,33,82]. Wendling et al. (2002) extended the model of Jansen and Rit with slow inhibition and focused on simulating dynamics of an epileptic brain[75]. Another important model to mention is the model of Liley which incorporates the role of the (synaptic) equilibrium potential[12].

Wilson-Cowan model

The Wilson-Cowan model describes the evolution of mean activity of neuronal populations over time[76]. The model consists of one excitatory population and one inhibitory population which is the minimum representation of a NMM[13,60]. The measure of activity of the populations is the key quantity. Interactions between the neural masses are represented by a sigmoidal function (Equation E.2)[15]. Either one or both neural masses receive external input. The masses are synaptically coupled to each other and themselves. Due to reciprocal connections, the model can produce oscillations (see Figure 3.6B)[65]. Mainly the recurrent projection of the excitatory population to itself is important for these oscillations[50].

Jansen-Rit model

The Jansen-Rit model is a type of NMM that simulates cortical columns. Cortical columns are considered to be the basic functional units of the cerebral cortex. The model consists of three neural masses: pyramidal neurons, excitatory interneurons and inhibitory interneurons as shown schematically in Figure 3.7A[32]. All connections between the neural masses are excitatory, except for the input from inhibitory interneurons received by pyramidal cells. Pyramidal cells also receive (excitatory) external input. This input originates from other cortical columns and background activity. The mathematical description of the model consists of a system of three second order DEs: 1). for the excitatory postsynaptic potential (EPSP) from the pyramidal neurons to both masses of interneurons, 2). for the EPSP entering the mass of pyramidal neurons, and 3). for the inhibitory postsynaptic potential (IPSP) entering the mass of pyramidal neurons. The difference between the EPSP and IPSP entering the pyramidal cell population is proportional to an EEG signal[65]. The Jansen-Rit model simulates different types of activity, like a (noisy) α-rhythm (see Figure 3.7B), slow periodic activity and evoked potentials. The type of activity simulated with the model can be tuned by the strength of inhibition[23].

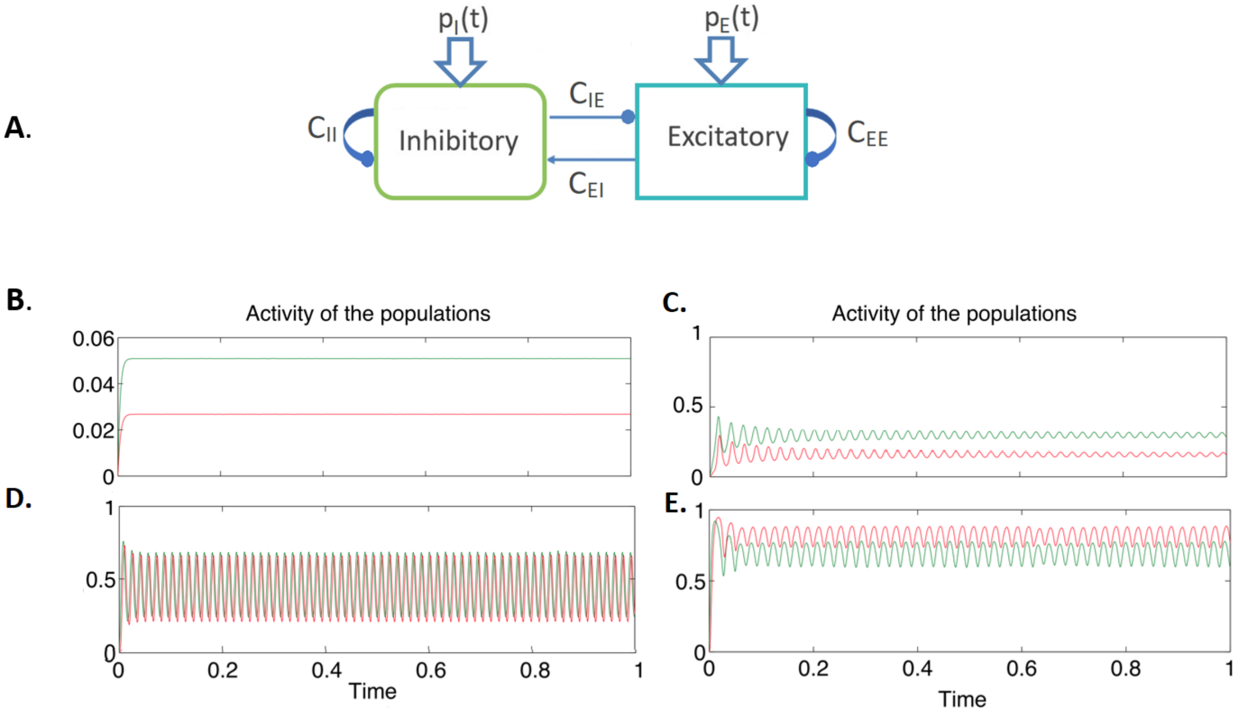

Figure 3.6: **Wilson-Cowan model.** A. Schematic overview of the Wilson-Cowan model. The model consists of two coupled neural masses: one excitatory (E) and one inhibitory (I) mass. The strength of the synaptic connections between two neural populations is modelled with constants C_{lk} with $l, k \in \{I, E\}$. The double subscripts depict the presynaptic population followed by the postsynaptic population. Arrows indicate excitatory connections and spheres indicate inhibitory connections. External inputs to both masses are represented by $p_E(t)$ for the excitatory population and $p_I(t)$ for the inhibitory population. Figures B.-E. show output activity of the excitatory population (red) and inhibitory population (green) for different inputs (B. 0.2, C. 0.4, D. 0.7, E. 1.18) received by the excitatory population only. Figures B.-E. adapted from Onslow et al. (2014) [50].

Liley model

Liley et al. (2002) proposed an electrocortical model, constructed at the scale of cortical columns[41]. This is a spatially homogeneous neural field model. NMMs describe how neural activity evolves over time, while neural field models characterize activity over time and space[55]. Figure 3.8A shows the topology of the Liley model. The Liley model consists of an excitatory and inhibitory population which are interconnected. All neural populations receive external (subcortical) input. The mean excitatory membrane potential is taken as a proxy for the EEG signal[6]. The neural populations are modelled as conductance-based neurons, while the populations of the Wilson-Cowan model and Jansen-Rit model are convolution-based [46,54]. The fundamental difference between convolution-based and conductance-based models is that the latter have nonlinear dynamics. Moreover, modelling of synaptic currents is biologically more realistic in conductance-based models. The Liley model reproduces key features of the human EEG e.g. chaotic and noise driven oscillatory activity at the frequency of the α-rhythm, cortical evoked potentials, travelling waves and threshold type spike activity (see Figure 3.8B)[41]. The model is used to gain a better understanding of e.g. the effect of anesthesia on the EEG or burst suppression[5,6]. Furthermore, Ruijter et al. (2017) used an adapted version of the Liley model to investigate the underlying pathophysiological mechanisms of EEG abnormalities in postanoxic patients[58].

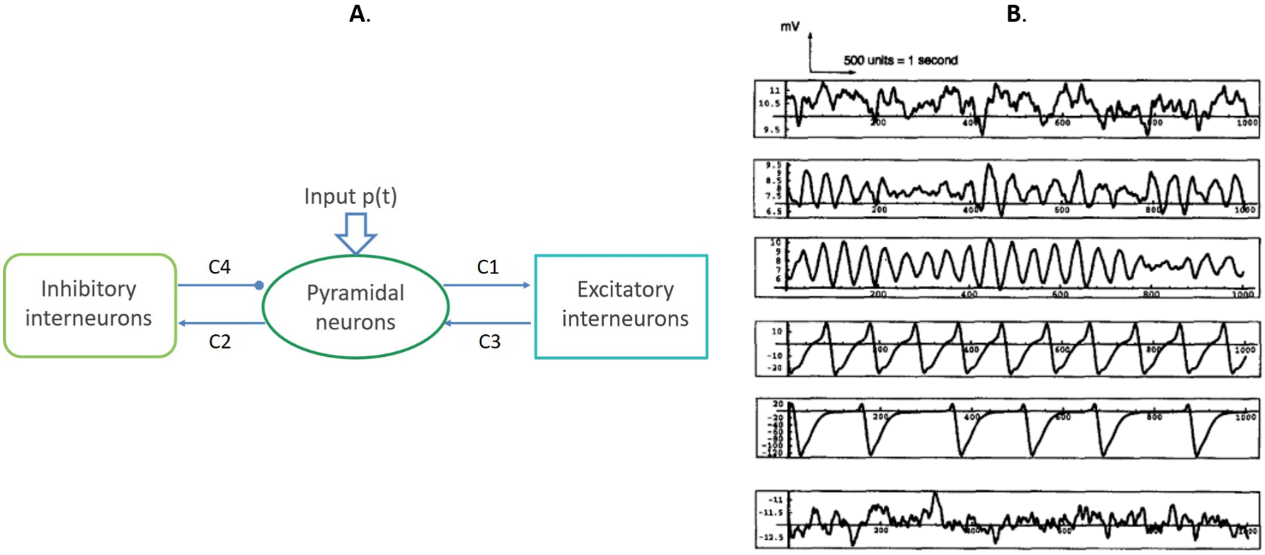

Figure 3.7: **Jansen-Rit model.** A. Schematic overview of the Jansen-Rit model. The strength of the synaptic connections between two neural populations is modelled with constants C_i with $i \in \{1{,}2{,}3{,}4\}$. Arrows indicate excitatory connections and spheres indicate inhibitory connections. External input to pyramidal neurons is represented by $p(t)$. B. Examples of activity curves simulated with the Jansen-Rit model for multiple values of C, with $C = C1$, $C2 = 0.8C$, $C3 = 0.25C$ and $C4$ $=0.25C$. From top to bottom: C equals 68, 128, 135, 270, 675. The input was uniform noise between 120 and 320 Hz. Alpha-like activity shows for $C = 135$ (third curve). Figure from Jansen and Rit (1995)[32].

3.2.2 ATP-dependent neural mass model

To study the effects of ATP shortage on neural behaviour, we would like to gain more insight into changes in ion concentrations. These concentrations depend heavily on the strength of ATP-dependent NKAs as shown by Zandt et al. (2011)[79] and Dijkstra et al. (2016)[17]. We considered using one of the previously discussed NMMs and variants of these NMMs as a base for our ATP-dependent NMM. All of these NMMs are based on membrane potentials and, as desired, the output of all models can be compared to EEG signals. An important feature of NMMs is the population firing rate replacing the individual spikes of single cell models. This rate is influenced by the Nernst equilibrium potential of sodium and potassium. Current NMMs assume that ion concentrations and thus the Nernst equilibrium potentials, remain constant. This is indeed the case if supply of ATP is sufficient, but it no longer holds during ATP deprivation[80]. As far as we know, none of the existing NMM is formulated in terms of ion concentrations and adapting the Nernst equilibrium potential and firing rate in not possible in these models. However, this is required to study the neural response to ATP depletion. Moreover, we prefer a biophysiologically plausible model like the Liley model to understand the effect of ATP depletion on neural dynamics and to link the outcome to real EEG results of patients. As none of the existing NMM met our requirements, we constructed a new NMM.

From the previously described single cell models we learned how ion concentrations are modelled and what behaviour to expect at a single cell level during ATP depletion as shown by Zandt et al. (2011)[79] and Dijkstra et al. (2016)[17]. Both the strength of the NKAs and levels of intracellular chloride are important in the emergence of cytotoxic edema. Chloride levels and pump strength were included in our model. However, we decided to disregard any volume changes to limit the complexity of the model. Based on existing NMMs we know which components are essential to incorporate in our model and which components should be adapted. For example, the sigmoidal activation function (or firing rate function) is adjusted in our model to simulate membrane depolarization. After depolarization, the firing rate should

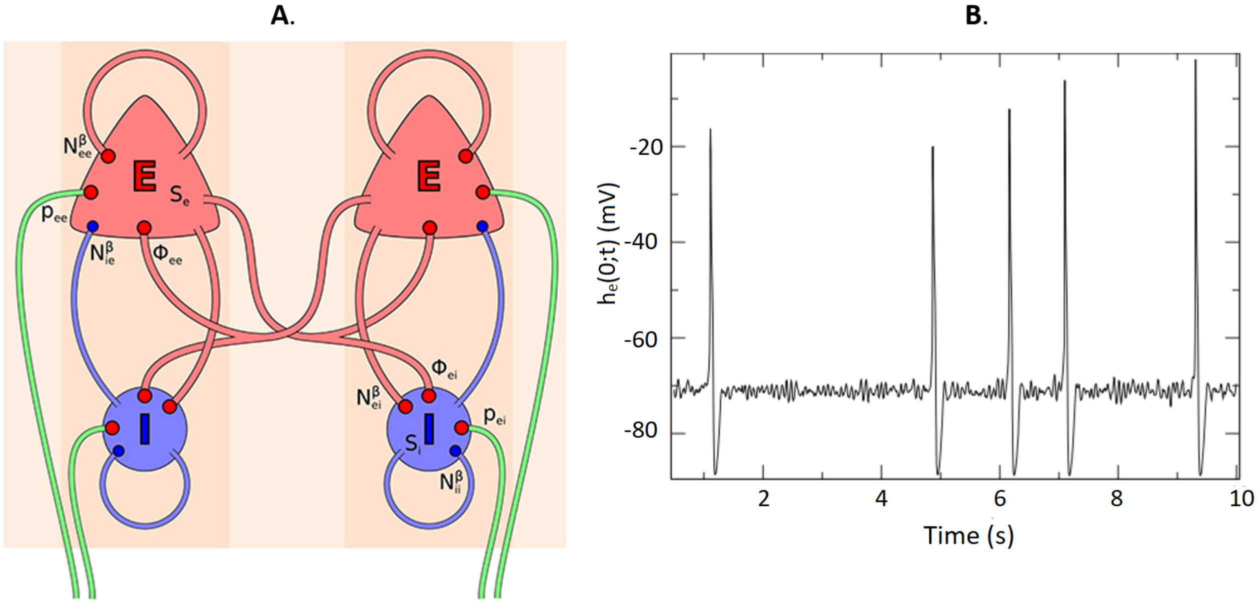

Figure 3.8: **Liley model.** A. Topology of the Liley model. The model consists of two neural populations: one excitatory (E) and one inhibitory (I) population. Both the left and right side of the picture represent a single cortical column. All neural populations receive external input. The excitatory and inhibitory connections are marked by red and blue circles, respectively. The number of synaptic connections is denoted by N_{lk} with $l, k \in \{i, e\}$. The double subscripts depict the presynaptic population followed by the postsynaptic population. Connections between two cortical columns are represented by Φ_{ek}. External (subcortical) inputs are marked by p_{ek} and local (intracortical) connections are indicated by S_l. Figure from Bojak et al. (2015)[6]. B. Example of activity generated with the Liley model: wave-spike activity of the mean excitatory soma membrane potential $h_e(t)$ for a mean external input of 2975s^{-1}. Figure adapted from Liley et al. (2002)[41].

become zero and long-lasting depolarizations (depolarization block) should occur. This requires the firing rate to become zero after reaching its maximal value. In accordance with the Wilson-Cowan model and Liley model, EEG signals can already be reproduced by including one excitatory and one inhibitory neural mass. Lastly, at least the excitatory neural mass should receive an external (excitatory) input and reciprocal connections should be included to produce oscillations. The production of oscillations as a response to external input is used as a check of the model behaviour at physiological ATP levels.

4 | Methods

Before explaining the newly constructed NMM, we provide more information about cell biological topics relevant for this research. Computational models are often compared to experimental data. As experimental data were not available for this study, we created a network model of coupled spiking single cells prior to the NMM and compared the outcome of both models to each other. This chapter provides a detailed description of both models. The NMM is linked to the underlying microscopic neurodynamics of a single cell. This allows for adjusting the strength of the NKAs based on the amount of available ATP, while tracking the changes in ion concentrations at population level. An important part of our work involved deriving a new equation for the firing rate based on (varying) Nernst equilibrium potentials. Although the model is largely based on single cell dynamics, heterogeneity is created within the firing rate. This chapter describes the derivation of this new firing rate function as well. Lastly, we elucidate the validation of the NMM.

N.B. To distinguish between excitatory, inhibitory, extracellular and intracellular, the following notation is used throughout this report: excitatory (E), inhibitory (I), extracellular (e) and intracellular (i).

4.1 Cell biology

The most important ion species present in the intracellular space (ICS) and ECS are sodium, potassium, chloride and calcium. These ion species were incorporated in the models, except for calcium. Calcium mostly plays a role in secondary processes which were not considered in this study. Ion currents are yielded by leak channels and voltage-gated channels. Ion pumps and other transporters in the cellular membrane maintain specific ion gradients. Figure 4.1 shows a schematic overview of one neuron including the components considered in this study. The components are leak channels of sodium, potassium and chloride, voltage-gated channels of sodium, potassium and chloride, NKA and KCL cotransporter KCC2. These components were incorporated in the network model of coupled spiking single cells and the NMM.

The neurotransmitters involved in chemical synaptic transmission in the central nervous system are glutamate and γ-aminobutyric acid (GABA). Glutamate is an excitatory neurotransmitter which activates the fast α-amino-3-hydroxy-5-methyl-4-isoxazolepropionic (AMPA) receptors. The inhibitory neurotransmitter GABA activates the fast GABA$_A$ receptors[38]. The AMPA and GABA$_A$ receptors are incorporated in the NMM.

4.2 Network of coupled spiking single cells

This model consists of a network of coupled spiking single cells. Firstly, this section discusses all assumptions, choices and requirements relevant for this network model. Secondly, it elaborates on the different model components and how to combine them into this network.

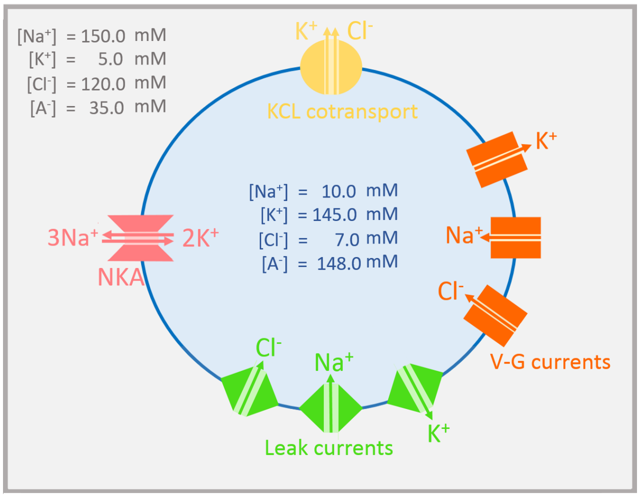

Figure 4.1: **Schematic overview of a representative neuron.** The cellular membrane (blue line) surrounds th ICS (blue circle). The grey square represents the (finite) ECS. The ICS and ECS are electroneutral. Typical intracellular and extracellular ion concentrations of sodium, potassium and chloride are shown. A^- denotes negatively charged impermeable anions. Leak channels (green) and voltage-gated channels (orange) result in ion currents. The Na^+-K^+-ATPase (NKA, pink), and the KCL cotransporter KCC2 (yellow) counterbalance these currents. NKA consumes ATP to pump sodium and potassium against their electrochemical gradient. The KCL cotransporter uses the resulting potassium gradient to move chloride to the ECS.

4.2.1 Model assumptions, choices and requirements

The following assumptions and choices were incorporated in the design of the model:

- The ECS is finite.
- All neurons share the same ECS.
- Excitatory and inhibitory cells have the same size.
- Volume changes are not considered in the model.
- The number of excitatory and inhibitory cells (and connections) is not equal. An E:I-ratio of approximately 80:20 was chosen[37,77].

The new model had to meet the following requirements:

- As a closed system is considered in which ions cannot leave nor enter, conservation of ions is guaranteed.
- To check stability of the model during rest, the resting membrane potential of the neurons is approximately -65 mV when the firing rate is zero.
- Applying external input results in rhythmic behaviour.
- The system settles at a nonzero GD equilibrium after depolarization following ATP deprivation.
- A high amplitude slow wave is visible in the simulated EEG signal after complete ATP cessation.

4.2.2 Model components

The network was based on the work of Zandt et al. (2011)[79] and Hübel et al. (2014)[30]. To get a network model of twenty HH-based neurons with an E:I-ratio of 80:20, we created sixteen excitatory neurons and four inhibitory neurons. All neurons were interconnected, but there was no self-connection. Figure 4.2 shows an example of a smaller network of four neurons. Each excitatory neuron received external input. This input varied slightly per neuron to create a heterogeneous neural population. Table B.1 summarizes the values of these inputs.

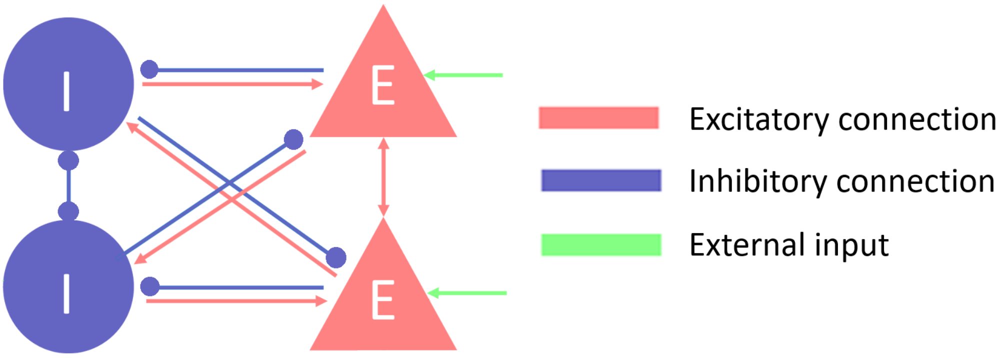

Figure 4.2: **Example overview of network model of coupled spiking single cells**. The model consisted of two types of spiking neurons: excitatory (E) and inhibitory (I) cells. In total, the model contained sixteen excitatory neurons and four inhibitory ones. All neurons were interconnected and each excitatory neuron received external input.

Ion concentrations

The total amount of each ion species N_X, with $X \in \{Na^+, K^+, Cl^-\}$, was conserved in the model:

$$N_X = W_e[X]_e^0 + W_i \sum_{l=1}^{20} [X]_{i,l}^0, \tag{4.1}$$

where $[X]_e^0$ and $[X]_i^0$ were the initial extracellular and intracellular concentrations of ion X, respectively. Subscript l referred to each individual cell, W_e denoted the extracellular volume and W_i denoted the intracellular volume, which was equal for all neurons.

The intracellular concentrations $[X]_i$ of sodium, potassium and chloride were determined with the DEs as described in subsection 4.2.3. Knowing the values of these intracellular concentrations, we calculated the extracellular concentrations $[X]_e$, as follows:

$$[X]_e = \frac{N_X - W_i \sum_{l=1}^{20} [X]_{i,l}}{W_e}. \tag{4.2}$$

Ion currents

The sodium and potassium currents consisted of a voltage-gated current and a leak current. The chloride current consisted of a leak current only. The equations for each neuron were as follows:

$$
\begin{aligned}
I_{Na} &= g_{Na} m_\infty(V)^3 h(t)(V - E_{Na}(t)) + g_{NaL}(V - E_{Na}(t)), &(4.3)\\
I_K &= g_K n(t)^4 (V - E_K(t)) + g_{KL}(V - E_K(t)), &(4.4)\\
I_{Cl} &= g_{ClL}(V - E_{Cl}(t)), &(4.5)
\end{aligned}
$$

where g_X and g_{XL} denoted the maximum conductances for the voltage-gated currents and leak currents, respectively. The Nernst equilibrium potentials E_X of sodium, potassium and chloride were determined with

$$E_X = \frac{RT}{z_X F} \ln\left(\frac{[X]_e}{[X]_i}\right), \tag{4.6}$$

where R was the universal gas constant, F was the Faraday constant, T was the absolute temperature and z_X was the valence of ion X.

The gating variables were modeled similar as in Zandt et al. (2014)[81]:

$$
\begin{aligned}
\alpha_m &= \frac{0.1(V+30)}{1-\exp\left(-\left(\frac{V+30}{10}\right)\right)}, & \beta_m &= 4\exp\left(-\left(\frac{V+55}{18}\right)\right),\\
\alpha_h &= 0.07\exp\left(-\left(\frac{V+44}{20}\right)\right), & \beta_h &= \frac{1}{1+\exp\left(-\left(\frac{V+14}{10}\right)\right)},\\
\alpha_n &= \frac{0.01(V+34)}{1-\exp\left(-\left(\frac{V+34}{10}\right)\right)}, & \beta_n &= 0.125\exp\left(-\left(\frac{V+44}{80}\right)\right),
\end{aligned} \tag{4.7}
$$

The gates n and h were described by

$$
\begin{aligned}
\frac{dn}{dt} &= \phi[\alpha_n(V)(1-n) - \beta_n(V)n],\\
\frac{dh}{dt} &= \phi[\alpha_h(V)(1-h) - \beta_h(V)h].
\end{aligned} \tag{4.8}
$$

where ϕ was the gating time constant.

The activation variable m has very fast dynamics. By setting the gating variable to its steady state value, we obtained a reduced amount of dynamical variables while preserving the dynamical features of the model[29]:

$$m = m_\infty(V) = \frac{\alpha_m(V)}{\alpha_m(V) + \beta_m(V)}. \tag{4.9}$$

KCl cotransporter KCC2

The KCL cotransporter KCC2 is an electroneutral symporter responsible for maintaining low intracellular concentrations of chloride. It uses the potassium gradient generated by the NKA to extrude chloride ions. Therefore, it influences the amount of intracellular and extracellular concentrations of potassium and chloride. The molar transmembrane ion flux J_{KCL} generated by KCC2 was determined as follows[17]:

$$J_{KCl} = U_{KCl}\frac{RT}{F}\ln\left(\frac{[K]_i[Cl]_i}{[K]_e[Cl]_e}\right), \tag{4.10}$$

where U_{KCl} was the strength of the cotransport. This strength depended on the flux parameter of the KCL cotransporter g_{KCL} and Faraday's constant, as follows[17,67]:

$$U_{KCl} = \frac{g_{KCl}}{F}. \tag{4.11}$$

Na$^+$K$^+$-ATPase

The NKA depends on the concentration of intracellular sodium and extracellular potassium as follows[3]:

$$I_p = \rho_p A\left(1+\exp\left(\frac{25-[Na]_i}{3}\right)\right)^{-1}\left(1+\exp\left(\frac{5.5-[K]_e}{1}\right)\right)^{-1}, \tag{4.12}$$

where ρ_p was the maximal pump current and A was the membrane surface of a neuron.

As mentioned earlier in this chapter, the external input varied moderately per neuron. To maintain a heterogeneous neuronal population, even when no external input is applied, each neuron had a slightly different maximal pump current. Table B.1 summarizes the values of the maximal pump currents.

It is not fully known how the NKA depends on the amount of available ATP. We assumed there is a linear relationship between the strength of the pump and ATP. A decrease of ATP influences the strength of the NKA which, in turn, leads to changes in intracellular and extracellular ion concentrations. The amount of ATP was incorporated in variable δ as follows:

$$\delta = \frac{ATP}{ATP + K_{ATP}}, \tag{4.13}$$

where ATP was the amount of available ATP and K_{ATP} was the dissociation constant of the ATP binding with the pump[11].

Synaptic coupling

All neurons were coupled via synaptic connections. Following Dayan et al. (2001), this type of coupling was modeled with[14]

$$I_{syn,k} = \sum_l \epsilon_{kl} r_l(t)(V_{k,syn} - V_k), \tag{4.14}$$

where ϵ_{kl} was the coupling strength between neurons k and l for $1 \leq (k,l) \leq N$ with N the total number of neurons in the network, r_l was the fraction of open receptors of neuron l, $V_{k,syn}$ was the synaptic reverse potential and V_k was the membrane potential of neuron k at time t[14]. If neuron l was coupled to neuron k, $\epsilon_{kl} > 0$, else $\epsilon_{kl} = 0$. If both neurons were excitatory $\epsilon_{kl} = \epsilon^{EE}$, while if both neurons were inhibitory $\epsilon_{kl} = \epsilon^{II}$. Moreover, we set $\epsilon_{kl} = \epsilon^{EI}$ if neuron k was excitatory and neuron l was inhibitory and $\epsilon_{kl} = \epsilon^{IE}$ if neuron k was inhibitory and neuron l was excitatory.

$V_{k,syn}$ was either equal to the Nernst equilibrium potential of AMPA $V^{eq}_{k,AMPA}$ or GABA$_A$ $V^{eq}_{k,GABA_A}$. $V^{eq}_{k,AMPA}$ was sensitive to changes in the Nernst equilibrium potentials of both sodium and potassium and determined as follows:

$$V^{eq}_{k,AMPA} = \frac{E_{Na,k} + E_{K,k}}{2}. \tag{4.15}$$

The Nernst equilibrium potential of chloride strongly influenced $V^{eq}_{k,GABA_A}$. Thus,

$$V^{eq}_{k,GABA_A} = E_{Cl,k}. \tag{4.16}$$

To determine the fraction of open receptors, the following equation was used:

$$\frac{dr_l}{dt} = \left(\frac{1}{\tau_r} - \frac{1}{\tau_d}\right) \frac{1}{1 + \exp\left(-\left(\frac{V_l - 10}{k_s}\right)\right)} (1 - r_l) - \frac{1}{\tau_d} r_l, \tag{4.17}$$

where k_s was the slope parameter and τ_r and τ_d were the rise and decay time constant of the synapse, respectively.

4.2.3 Model overview

We combined all equations described above to determine the ODEs of the model, keeping in mind that the first four neurons were inhibitory and the other sixteen were excitatory. Each neuron consisted of the following set of equations:

$$\begin{cases} C_m \dfrac{dV_k}{dt} &= -I_{Na,k} - I_{K,k} - I_{Cl,k} - I_{p,k} + I_{app,k} + \dfrac{1}{N^I} \displaystyle\sum_{l=1}^{4} \epsilon_{kl} r_l(t) (V_{k,GABA_A} - V_k) \\ & \quad + \dfrac{1}{N^E} \displaystyle\sum_{l=5}^{20} \epsilon_{kl} r_l(t) (V_{k,AMPA} - V_k), \\ \dfrac{dn_k}{dt} &= \phi[\alpha_{n_k}(V_k)(1 - n_k) - \beta_{n_k}(V_k) n_k], \\ \dfrac{dh_k}{dt} &= \phi[\alpha_{h_k}(V_k)(1 - h_k) - \beta_{h_k}(V_k) h_k], \\ \dfrac{dr_k}{dt} &= \left(\dfrac{1}{\tau_r} - \dfrac{1}{\tau_d}\right) \dfrac{1}{1 + \exp\left(-\left(\frac{V_k - 10}{k_s}\right)\right)} (1 - r_k) - \dfrac{1}{\tau_d} r_k, \\ \dfrac{d[Na]_{i,k}}{dt} &= -\dfrac{\gamma}{W_i} \left(I_{Na,k} + 3\delta I_{p,k}\right), \\ \dfrac{d[K]_{i,k}}{dt} &= -\dfrac{\gamma}{W_i} \left(I_{K,k} - 2\delta I_{p,k} + F J_{KCl}\right), \\ \dfrac{d[Cl]_{i,k}}{dt} &= \dfrac{\gamma}{W_i} \left(I_{Cl,k} - F J_{KCl}\right), \end{cases} \tag{4.18}$$

where C_m was the specific membrane capacitance, $I_{app,k}$ was the external current applied to neuron k, N^I was the total number of inhibitory neurons and N^E was the total number of excitatory neurons. Conversion of the ion currents to ion fluxes was denoted by γ. This value depended on A and F [30]:

$$\gamma = \frac{A}{F}. \tag{4.19}$$

We performed all simulations with MATLAB, using the stiff solver ODE15s for solving the DEs. Table A.1 contains all parameter values used in the network model.

Changes in ATP were modeled with sigmoid curves to avoid sudden changes. The initial amount of ATP ATP^0, the fraction of ATP depletion f_{ATP} and the duration of the ATP depletion influenced the shape of the curve as follows:

$$ATP = ATP^0 \left[1 - f_{ATP}\left(1 + \exp\left(0.1\left(-t + t_{ATP}^{start}\right)\right)\right)^{-1}\left(1 + \exp\left(0.1\left(t - t_{ATP}^{end}\right)\right)\right)^{-1}\right], \tag{4.20}$$

where t_{ATP}^{start} was the time at which the ATP depletion started and t_{ATP}^{end} was the time at which the amount of ATP was restored.

An external current was applied to the model using a similar equation:

$$I_{app} = I_{app}^{max}\left(1 + \exp\left(0.1\left(-t + t_{app}^{start}\right)\right)\right)^{-1}\left(1 + \exp\left(0.1\left(t - t_{app}^{end}\right)\right)\right)^{-1}, \tag{4.21}$$

where I_{app}^{max} was the maximal applied current and t_{app}^{start} and t_{app}^{end} were the start and end times between which the external current was applied to the model.

Gibbs-Donnan equilibrium

Explicitly including intracellular anions was not necessary to attain a GD equilibrium with this model. Although the ion rate equations implied that all ion currents should disappear to settle at an equilibrium, there was also a constraint on the charge concentration $Q_{i,k}$ for the ICS[30]. This constraint was based on Equation 4.18 for $I_{app,k} = 0$ and $I_{p,k} = 0$:

$$\begin{aligned} \Delta Q_{i,k} &:= \Delta Na_{i,k} + \Delta K_{i,k} - \Delta Cl_{i,k} \\ &= \frac{\gamma}{W_i} C_m \Delta V_k, \end{aligned} \tag{4.22}$$

where the difference between the initial and final value of each variable is denoted by Δ.

Simulating EEG

Instead of taking the difference between EPSP and IPSP as for example done in the Jansen-Rit model, we determined the EEG of the network of coupled spiking single cells by taking the difference between the mean excitatory postsynaptic current (EPSC) and mean inhibitory postsynaptic current (IPSC) of the excitatory neurons. The EPSC and IPSC were the ion flows causing an EPSP and IPSP to occur, respectively:

$$\begin{aligned} \text{EPSC} &= \frac{1}{N^E}\sum_{k=5}^{20}\left(\frac{1}{N^E}\sum_{l=5}^{20}\epsilon_{kl} r_l(t)[V_{k,AMPA} - V_k]\right), \\ \text{IPSC} &= \frac{1}{N^E}\sum_{k=5}^{20}\left(\frac{1}{N^I}\sum_{l=1}^{4}\epsilon_{kl} r_l(t)[V_{k,GABA_A} - V_k]\right), \\ \text{EEG} &= \text{EPSC - IPSC}. \end{aligned} \tag{4.23}$$

We filtered the simulated EEG signal using a second order Butterworth bandpass filter with cut-off frequencies at 0.5 and 30 Hz.

4.3 Neural mass model based on ion concentrations

The newly constructed NMM was based on the dynamics of a single HH neuron. This section discusses all essential parts of this model. The structure of this section is similar to the previous one. Also, we elaborate on the derivation of the new firing rate function.

4.3.1 Model assumptions, choices and requirements

The new NMM had to meet the same requirements as the previously discussed network model and the same assumptions and choices applied to the NMM. Several additional assumptions and choices were important for the NMM model, namely:

- The neurons have a semi-permeable membrane and impermeant anions are present. This was required such that the neurons settled at a nonzero GD equilibrium when all energy-dependent ion transport was absent.
- The EEG signal of patients with postanoxic coma after cardiac arrest showed no visible differences between the EEG channels. Thus, a spatially homogeneous model was assumed to be appropriate.
- It was assumed that each neuron, on average, shows the same behaviour. Hence, the NMM was based on the dynamics of a single neuron, while heterogeneity was created within the firing rate.

4.3.2 Model components

Similar to the Wilson-Cowan model and Liley model, this NMM consisted of one excitatory population, representing the pyramidal neurons, and one inhibitory population, representing the interneurons (Figure 4.3). The two neural populations were connected to each other and themselves via excitatory and inhibitory projections. The excitatory mass received external excitatory input.

This section starts by introducing each component of the model individually. Next, all components are combined to construct the NMM.

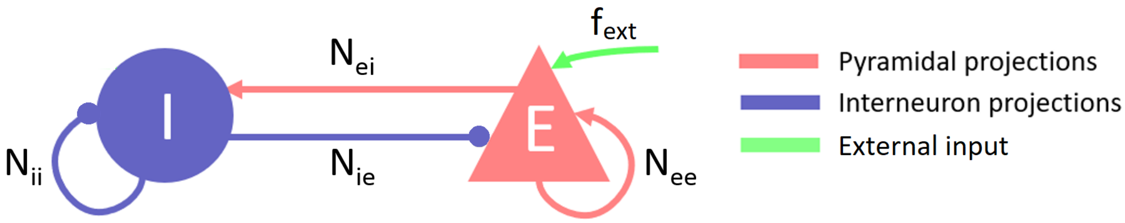

Figure 4.3: **Overview of ATP-dependent neural mass model**. The model consists of two neural masses: one excitatory (E) and one inhibitory (I) mass. The number of synaptic connections is denoted by N_{lk} with $l, k \in \{e, i\}$. The double subscripts depict the presynaptic population followed by the postsynaptic population. External excitatory input to the excitatory neural mass is marked with f_{ext}. Table A.2 provides more information about model parameters.

Ion concentrations

The total amount of each ion was conserved in this model and calculated with

$$N_X = [X]_e^0 W_e + ([X]_i^{E,0} + [X]_i^{I,0}) W_i. \tag{4.24}$$

Similar to the network model, we determined intracellular concentrations of sodium, potassium and chloride with DEs, as shown in subsection 4.3.3.

Based on the intracellular concentrations, we determined the extracellular concentrations with

$$[X]_e = \frac{N_X - \left([X]_i^E + [X]_i^I\right) W_i}{W_e}. \tag{4.25}$$

Leak currents

The HH equations for the leak and voltage-gated currents are derived from the Goldman-Hodgkin-Katz (GHK) flux equations. As we used these latter equations in the NMM, this NMM is called an ion-based model instead of the previously explained conductance based model.

The cell membrane is considered to be a homogeneous plate which can be crossed instantaneously by (permeable) ions. The flux inside this cell membrane depends on two 'forces': the difference in ion concentrations in ICS and ECS (leading to diffusion of ions from high to low concentration) and the potential difference across the membrane (resulting in an electrical field and drift of ions). The diffusion component is described by Ficks law, and the electrical drift is described by Ohm's law. These processes together lead to the GHK flux equation, which was used to determine the leak currents[19,45]:

$$I_X^{L,q} = P_X^{L,q} \frac{z_X^2 F^2 V^q}{RT} \frac{[X]_i^q - [X]_e^q \exp\left(-\frac{z_X F V^q}{RT}\right)}{1 - \exp\left(-\frac{z_X F V^q}{RT}\right)}, \tag{4.26}$$

where $P_X^{L,q}$ was the fixed leak permeability with $q \in \{E, I\}$. This equation should not be confused with the GHK voltage equation.

Voltage-gated currents

Besides the leak currents, we also included voltage-gated currents. We focused on the dynamics of the synapses by describing the mean behaviour of the neurons as a result of the mean membrane potential and mean inputs. Incorporation of fast dynamics of the activation and inactivation gates was therefore not possible in the NMM. Instead, steady state versions of all gates were implemented. The equations for the opening (α) and closing (β) rates of the activation gates m for sodium and n for potassium and the inactivation gate h for sodium were equal to those used in the network model (Equation 4.7). Steady states were determined with

$$n_\infty^q = \frac{\alpha_n^q}{\alpha_n^q + \beta_n^q}, \quad m_\infty^q = \frac{\alpha_m^q}{\alpha_n^q + \beta_m^q}, \quad h_\infty^q = \frac{\alpha_h^q}{\alpha_h^q + \beta_h^q}. \tag{4.27}$$

The model contained a transient sodium current $I_{Na}^{T,q}$, a delayed rectifier potassium current $I_K^{D,q}$, and a voltage-gated chloride current $I_{Cl}^{G,q}$. Dijkstra et al. (2016) fitted a function to the experimental data of Rungta et al. (2015), who discovered that the ion exchanger SLC26A11 acts as a voltage-gated chloride channel[59]. The equations for the voltage-gated currents were adapted versions from the model of Dijkstra et al. (2016)[17]:

$$I_{Na}^{T,q} = P_{Na}^{T,q} m_\infty^3 h_\infty \frac{F^2 V^q}{RT} \frac{[Na]_i^q - [Na]_e \exp\left(-\frac{FV^q}{RT}\right)}{1 - \exp\left(-\frac{FV^q}{RT}\right)}, \tag{4.28}$$

$$I_K^{D,q} = P_K^{D,q} n_\infty^4 \frac{F^2 V^q}{RT} \frac{[K]_i^q - [K]_e \exp\left(-\frac{FV^q}{RT}\right)}{1 - \exp\left(-\frac{FV^q}{RT}\right)}, \tag{4.29}$$

$$I_{Cl}^{G,q} = \frac{P_{Cl}^{G,q}}{1 + \exp\left(-\frac{V^q+10}{10}\right)} \frac{F^2 V^q}{RT} \frac{[Cl]_i^q - [Cl]_e \exp\left(\frac{FV^q}{RT}\right)}{1 - \exp\left(\frac{FV^q}{RT}\right)}, \tag{4.30}$$

where $P_{Na}^{T,q}$ was the maximal transient sodium permeability, $P_K^{D,q}$ was the maximal delayed potassium permeability and $P_{Cl}^{G,q}$ was the maximal voltage-gated chloride permeability.

Na$^+$K$^+$-ATPase and KCL cotransporter KCC2

Both NKA and KCC2 were explained in subsection 4.2.2. However, the corresponding equations are slightly different as the NMM consisted of an excitatory and inhibitory population instead of single cells. The equations of the pump and cotransporter for the NMM were

$$I_p^q = \rho_p^q \left(1 + \exp\left(\frac{25 - [Na]_i^q}{3}\right)\right)^{-1} \left(1 + \exp\left(\frac{5.5 - [K]_e}{1}\right)\right)^{-1}, \tag{4.31}$$

$$J_{KCl}^q = U_{KCl} \frac{RT}{F} \ln\left(\frac{[K]_i^q [Cl]_i^q}{[K]_e [Cl]_e}\right). \tag{4.32}$$

Note that we used the same extracellular concentrations for both neural masses, but different intracellular concentrations of sodium, potassium and chloride as these were specific for each neural mass.

Firing rate

The firing rate, often modelled with a sigmoid curve, is influenced by three factors: the synaptic current I, the Nernst equilibrium potential of sodium E_{Na} and the Nernst equilibrium potential of potassium E_K[80,81]. As most modelers consider the Nernst equilibrium potentials to be constant, adapting the sigmoid curve is not necessary. However, we were interested in the effects of a decreased ATP level on the ion concentrations, which causes the Nernst equilibrium potentials of sodium and potassium to change which can lead to a depolarization block. Therefore, we determined a new expression for the firing rate curve including I, E_{Na} and E_K. Note that E_{Cl} was not included. To determine the firing rate curve, the same single HH cell was used as mentioned by Zandt et al. (2011)[79]. It was decided to consider only continuous spiking activity and to disregard transient spikes. Continuation of periodic orbits in MatCont offered a fast option to filter the stationary spikes from the transient spikes as the latter are non-periodic[16]. The period between consecutive spikes was determined with this method. Next, the firing frequency was calculated by taking the reciprocal of the period.

Before performing this continuation, we defined the range of values of I, E_{Na} and E_K for which the curve was valid. This decision was based on so-called Hopf branches. An (Andronov-)Hopf bifurcation is a critical point where the stability of a system switches and a limit cycle (periodic solution) is born. Limit cycles, and thus stationary spikes, cannot arise for values of I, E_{Na} and E_K lying outside the area of the Hopf branches. Hence, we set the firing rate function to zero for these values. The firing rate function was valid for $I \in \{-100, 500\}$, $E_{Na} \in \{-20, 80\}$ and $E_k \in \{-95, 25\}$. Figure 4.4A shows an example of a bifurcation diagram of the HH model. A supercritical Hopf bifurcation gives rise to a stable limit cycle, resulting in periodic behaviour of the model. Moreover, the firing rate became zero when I exceeded the value at which the Hopf bifurcation occurred. This corresponded to simulation of a depolarization block.

Based on all simulations and continuations with the HH neuron, the following form of the equation was chosen:

$$FR^q(I^q, E_K^q, E_{Na}^q) = \begin{cases} \kappa^q \sqrt{I^q - I_{th}^q}(1 - H(I^q - I_{th2}^q)) & \text{for } I^q \geq I_{th}^q, \\ 0 & \text{for } I^q < I_{th}^q, \end{cases} \tag{4.33}$$

where H denoted a Heaviside step function. The two thresholds I_{th}^q and I_{th2}^q were the cut-off points as shown in Figure 4.4B. The first threshold I_{th}^q corresponds to a homoclinic bifurcation of the HH cell. At this point, the firing rate decreased to 0.

The firing rate curve was smoothed to avoid numerical instabilities and to create neural heterogeneity. This was achieved by convoluting with the kernel:

$$g(x) = \frac{1}{\sqrt{2\pi}\sigma} e^{\left(-\frac{x^2}{\sigma}\right)}, \tag{4.34}$$

with standard deviation σ.

This resulted in

$$\begin{aligned} FR_{smooth}^q(I^q, E_K^q, E_{Na}^q) &= (g * FR^q)(I^q) \\ &= \int_{I_{th}^q}^{\infty} g(I^q - \tau) FR^q(\tau) d\tau \text{ for } FR, g : [I_{th}, \infty) \to [0, \infty)\,. \end{aligned} \tag{4.35}$$

To find appropriate values for our function, we performed curve fitting with the curve fitting toolbox of MATLAB (Matlab R2018b, Mathworks Inc., Massachusetts, USA). This resulted in

$$\begin{aligned} \kappa^q(E_{Na}^q, E_K^q) = {} & q_{00} + q_{10}E_K^q + q_{01}E_{Na}^q + q_{20}(E_K^q)^2 + q_{11}E_K^q E_{Na}^q + q_{02}(E_{Na}^q)^2 + q_{30}(E_K^q)^3 \\ & + q_{21}(E_k^q)^2 E_{Na}^q + q_{12}E_K^q(E_{Na}^q)^2 + q_{03}(E_{Na}^q)^3, \end{aligned} \tag{4.36}$$

$$\begin{aligned} I_{th}^q(E_{Na}^q, E_K^q) = {} & p_{00} + p_{10}E_K^q + p_{01}E_{Na}^q + p_{20}(E_K^q)^2 + p_{11}E_K^q E_{Na}^q + p_{02}(E_{Na}^q)^2 + p_{30}(E_K^q)^3 \\ & + p_{21}(E_k^q)^2 E_{Na}^q + p_{12}E_K^q(E_{Na}^q)^2 + p_{03}(E_{Na}^q)^3, \end{aligned} \tag{4.37}$$

$$\begin{aligned} I_{th2}^q(E_{Na}^q, E_K^q) = {} & r_{00} + r_{10}E_K^q + r_{01}E_{Na}^q + r_{20}(E_K^q)^2 + r_{11}E_K^q E_{Na}^q + r_{02}(E_{Na}^q)^2 + r_{30}(E_K^q)^3 \\ & + r_{21}(E_k^q)^2 E_{Na}^q + r_{12}E_K^q(E_{Na}^q)^2 + r_{03}(E_{Na}^q)^3. \end{aligned} \tag{4.38}$$

The values of the coefficients of the polynomials κ, I_{th} and I_{th2} are provided in Table A.3. Figure 4.5 shows the quality of the fit of the two thresholds.

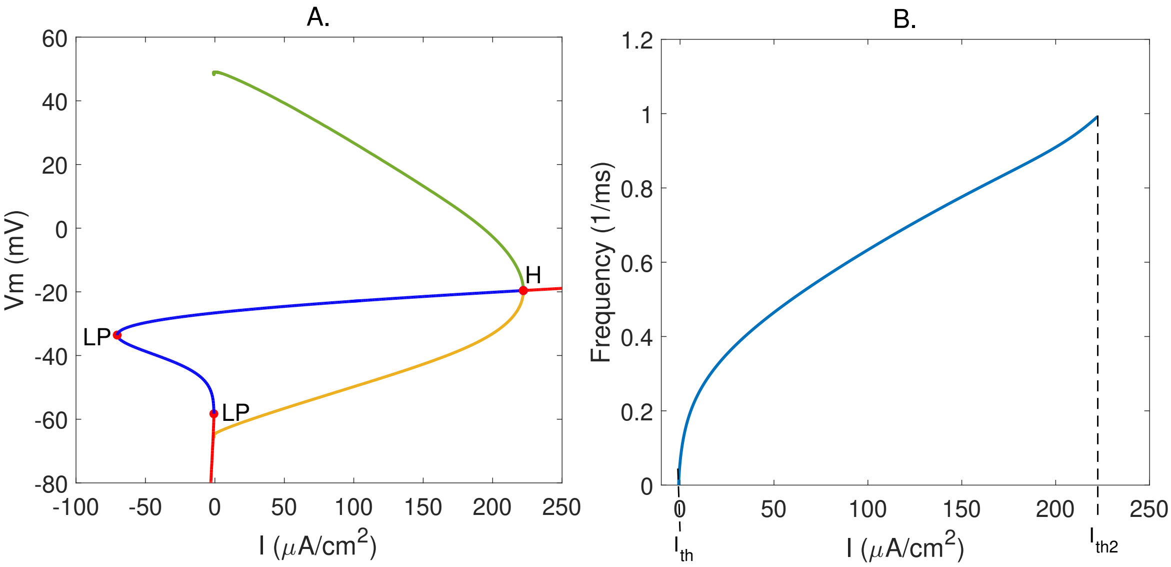

Figure 4.4: **Overview of constructing F(I)-curve.** A. Bifurcation diagram of the HH model as a function of external input I, for E_K = -65 mV and E_{Na} = 50 mV. Solid red lines denote stable equilibria. The dotted blue line denotes unstable equilibria. The green and yellow line indicate the maximum and minimum values of V_m at the stable limit cycle, respectively. The H indicates a supercritical Hopf bifurcation (first Lyapunov coefficient of -9.67e-3), corresponding to I_{th2}. B. Example of an F(I)-curve with E_K = -65 mV, E_{Na} = 50 mV and thresholds I_{th} and I_{th2}. The frequency becomes 0 when $I > I_{th2}$ as a depolarization block occurs.

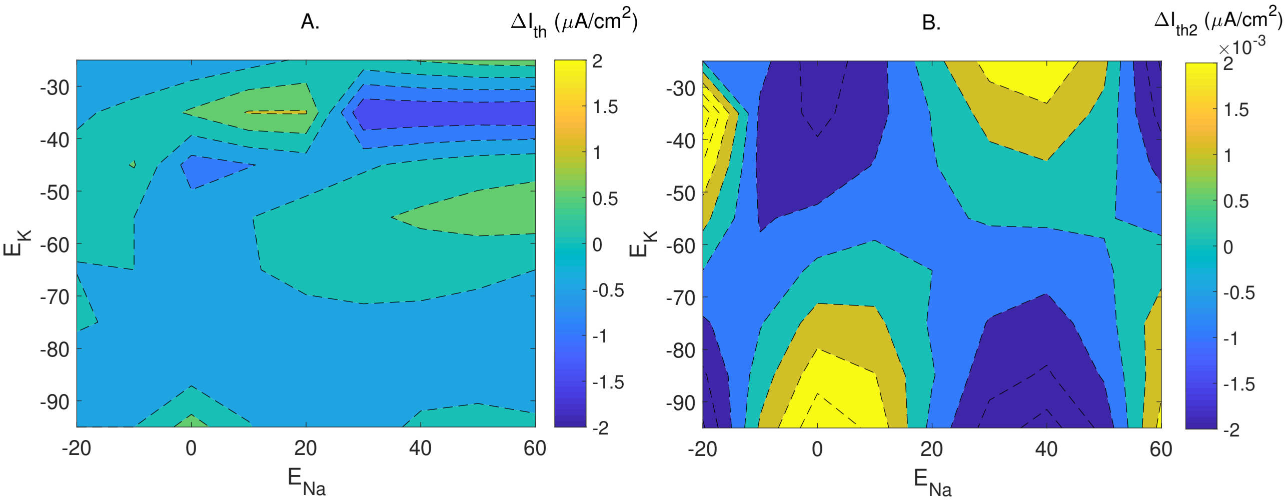

Figure 4.5: **Quality of threshold fitting.** The color bar indicates the difference (Δ) between the threshold value determined with the HH model and the value determined with Equation 4.37 and Equation 4.38 for I_{th} and I_{th2}, respectively. A. Quality of fitting I_{th} with difference $\Delta I_{th} \in \{-2, 2\}$. B. Quality of fitting I_{th2} with $\Delta I_{th2} \in \{-2 \cdot 10^{-3}, 2 \cdot 10^{-3}\}$.

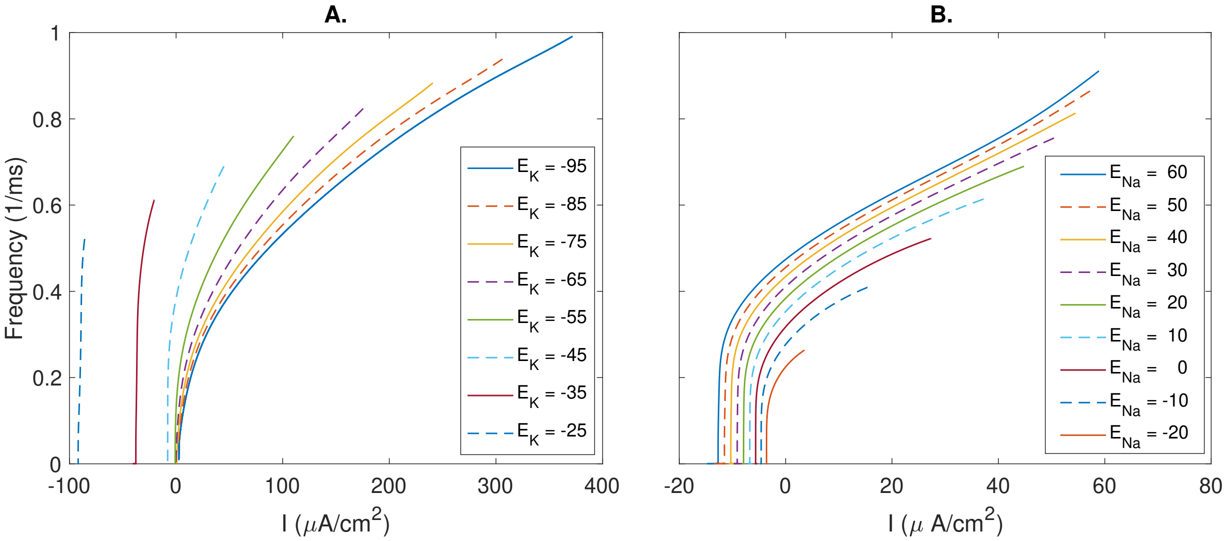

Figure 4.6: **Examples of influence of E_{Na} and E_K on F(I)-curve.** A. F(I)-curves with $E_{Na} = 20$ mV and varying values of E_K in mV. An increased E_K leads to an increased neural excitability. B. F(I)-curves with $E_K =$ -45 mV and varying values of E_{Na} in mV. Decrease of E_{Na} results in a smaller excitability range.

Figure 4.6 shows the effects of changing Nernst potentials on the firing rate. An increase of E_K led to a decrease of I_{th} and an increase of the firing frequency. Thus, the neuron became more excitable. In some cases, I_{th} even became negative indicating spontaneous generation of action potentials. (Figure 4.6A). Only inhibition of the neurons can prevent them from this behaviour. An increase of E_K leads to a smaller value of I_{th2}. Hence, a depolarization block would occur earlier in this case. Similar to an increased E_K, a decrease of E_{Na} led to a lower value of I_{th2}. However, it decreased the firing rate and increased I_{th}. Thus, a decrease of E_{Na} resulted in a smaller excitability range of the neurons (Figure 4.6B).

AMPA and GABA$_A$ receptors

In most NMMs, the postsynaptic currents (PSCs) or postsynaptic potentials (PSPs) are modeled by an alpha function. However, instead of using convolution to transform the pre-synaptic firing rate into a PSC or PSP, we used kinetic models. Although these models are not able to mimic the smallest details of synaptic currents, they are appropriate for building network simulations as they provide a good approximation of most features. Examples of these features are rise, decay and voltage dependence[38].

Kinetics of the fast AMPA receptors at a cellular level can be approximated by the following two-state diagram:

$$\mathrm{C} + \mathrm{T} \underset{\beta}{\overset{\alpha}{\rightleftarrows}} \mathrm{O}, \tag{4.39}$$

where binding of the unbound form of the receptor C to one molecule of transmitter T leads to opening of the receptor. The open form is represented by O and the opening and closure rates are represented by α and β, respectively[38].

These kinetics can be described by a first-order kinetic equation:

$$\frac{dr_A}{dt} = \alpha_A[\mathsf{T}](1 - r_A) - \beta_A r_A, \tag{4.40}$$

where r_A is the fraction of open AMPA receptors[38].

We replaced T by firing rate FR to determine the kinetics at a population level:

$$\frac{dr_A}{dt} = \alpha_A[\mathsf{FR}_A](1 - r_A) - \beta_A r_A, \tag{4.41}$$

$$\alpha_A[\mathsf{FR}_A] = \frac{\alpha_A^{max}\mathsf{FR}_A}{\mathsf{FR}_A + 15}, \tag{4.42}$$

where α_A^{max} was the maximum opening rate of the AMPA receptor and $\mathsf{FR}_A = \mathsf{FR}^E + f_{ext}$.

The postsynaptic current I_A depended on the fraction of open AMPA receptors, as follows:

$$I_A = \bar{g}_A r_A([Na]_e - [Na]_i), \tag{4.43}$$

where $\bar{g}_A$ was the maximal conductance[38]. The opening of the AMPA receptors, and thus the generation of I_A, led to an influx of sodium ions[2].

Similar equations applied to GABA$_A$ receptors as well:

$$\frac{dr_G}{dt} = \alpha_G[\mathsf{FR}_G](1 - r_G) - \beta_G r_G, \tag{4.44}$$

$$\alpha_G[\mathsf{FR}_G] = \frac{\alpha_G^{max}\mathsf{FR}_G}{\mathsf{FR}_G + 100}, \tag{4.45}$$

where α_G^{max} was the maximum opening rate of the GABA$_A$ receptor and $\mathsf{FR}_G = \mathsf{FR}^I$.

The postsynaptic current I_G depended on the fraction of open GABA$_A$ receptors, as follows:

$$I_G = \bar{g}_G r_G([Cl]_e - [Cl]_i), \tag{4.46}$$

where $\bar{g}_G$ was the maximal conductance[38]. The opening of the GABA$_A$ receptors, and thus generation of I_G, led to an influx of chloride ions[42].

Membrane potential

Membrane potential V depended on charge Q and membrane capacitance C as follows:

$$V = \frac{Q}{C} \text{ with } C = C_m \cdot A, \tag{4.47}$$

where C_m was the specific membrane capacitance and A was the surface area of the cell.

Charge Q was determined by multiplying F and intracellular molar amounts N_X of sodium, potassium and chloride. We kept track of the intra- and extracellular ion concentrations and computed the intracellular molar amounts as follows:[17]:

$$N_X = [X]_i \cdot W_i. \tag{4.48}$$

The difference between intra- and extracellular ion concentrations determined the membrane potential:

$$V^q = \frac{FW_i}{C}\Big(([Na^+]^q_i - [Na^+]^q_e) + ([K^+]^q_i - [^+K]^q_e) - ([Cl^-]^q_i - [Cl^-]^q_e) - ([A^-]_i - [A^-]_e)\Big), \tag{4.49}$$

where [A$^-$]$_i$ and [A$^-$]$_e$ were the intracellular and extracellular impermeant anion concentrations, respectively.

The presence of impermeant charged A$^-$ was necessary for the GD effect to occur. Electroneutrality of the bulk cannot be guaranteed as we were specifically interested in the membrane potential, but did not make a distinction between the bulk solution and the ion solution close to the membrane. Nevertheless, the electroneutrality principle was used to determine the order of magnitude of the ion concentrations:

$$[Na^+]^0_i + [K^+]^0_i + [Cl^-]^0_i + [A^-]_i = [Na^+]^0_e + [K^+]^0_e + [Cl^-]^0_e + [A^-]_e. \tag{4.50}$$

By choosing an initial resting membrane potential of -65 mV and fixing the initial concentrations of intra- and extracellular sodium, potassium and chloride and the extracellular concentration of impermeable anions, we determined the new value for the intracellular concentration of impermeable anions [A$^-$]$_i$ as follows:

$$V^0 = \frac{FW_i}{C}\Big(([Na^+]^0_i - [Na^+]^0_e) + ([K^+]^0_i - [K^+]^0_e) - ([Cl^-]^0_i - [Cl^-]^0_r) - ([A^-]_i - [A^-]_e)\Big). \tag{4.51}$$

4.3.3 Model overview

Combining all equations, the ion-based NMM consisted of the following coupled DEs:

$$\begin{cases}
\dfrac{d[Na]^E_i}{dt} &= \dfrac{1}{W_iF}\left(-I^{L,E}_{Na} - I^{T,E}_{Na} - 3\delta I^E_p\right) + \dfrac{1}{C}\left(g_{A,EE}N_{EE}r_A\left([Na]_e - [Na]^E_i\right)\right), \\
\dfrac{d[Na]^I_i}{dt} &= \dfrac{1}{W_iF}\left(-I^{L,I}_{Na} - I^{T,I}_{Na} - 3\delta I^I_p\right) + \dfrac{1}{C}\left(g_{A,EI}N_{EI}r_A\left([Na]_e - [Na]^I_i\right)\right), \\
\dfrac{d[K]^E_i}{dt} &= \dfrac{1}{W_iF}\left(-I^{L,E}_{K} - I^{D,E}_{K} + 2\delta I^E_p\right) - \dfrac{1}{W_i}J^E_{KCL}, \\
\dfrac{d[K]^I_i}{dt} &= \dfrac{1}{W_iF}\left(-I^{L,I}_{K} - I^{D,I}_{K} + 2\delta I^I_p\right) - \dfrac{1}{W_i}J^I_{KCL}, \\
\dfrac{d[Cl]^E_i}{dt} &= \dfrac{1}{W_iF}\left(I^{L,E}_{Cl} + I^{G,E}_{Cl}\right) - \dfrac{1}{W_i}J^E_{KCL} + \dfrac{1}{C}\left(g_{G,IE}N_{IE}r_G\left([Cl]_e - [Cl]^E_i\right)\right), \\
\dfrac{d[Cl]^I_i}{dt} &= \dfrac{1}{W_iF}\left(I^{L,I}_{Cl} + I^{G,I}_{Cl}\right) - \dfrac{1}{W_i}J^I_{KCL} + \dfrac{1}{C}\left(g_{G,II}N_{II}r_G\left([Cl]_e - [Cl]^I_i\right)\right), \\
\dfrac{dr_A}{dt} &= \alpha_A[FR_A](1 - r_A) - \beta_A r_A, \\
\dfrac{dr_G}{dt} &= \alpha_G[FR_G](1 - r_G) - \beta_G r_G,
\end{cases} \tag{4.52}$$

where N_{lk} was the number of synaptic connections between population l and population k with $l, k \in \{E, I\}$. The effective conductances g were: $g_{A,EE} = \bar{g}_A / N_{EE}$, $g_{A,EI} = \bar{g}_A / N_{EI}$, $g_{G,IE} = \bar{g}_G / N_{IE}$ and $g_{G,II} = \bar{g}_G / N_{II}$.

We performed all simulations with MATLAB, using the stiff solver ODE15s for solving the ODEs. Table A.2 contains all parameter values used in the network model. Changes in ATP were modeled with Equation 4.20. We used a similar equation to apply an external input to the NMM:

$$f_{ext} = f_{ext}^{max} \left(1 + \exp\left(0.02\left(-t + t_{ext}^{start}\right)\right)\right)^{-1} \left(1 + \exp\left(0.02\left(t - t_{ext}^{end}\right)\right)\right)^{-1}, \tag{4.53}$$

where f_{ext}^{max} was the maximal external input and t_{ext}^{start} and t_{ext}^{end} were the start and end times between which the external input was applied to the model.

The input currents I^E and I^I to determine FR^E and FR^I, respectively, were:

$$I^E = \frac{FW_i}{500 C A_i} \left(g_A N_{EE} r_A ([Na]_e - [Na]_i^E) - g_G N_{IE} r_G ([Cl]_e - [Cl]_i^E)\right), \tag{4.54}$$

$$I^I = \frac{FW_i}{500 C A_i} \left(g_A N_{EI} r_A ([Na]_e - [Na]_i^I) - g_G N_{II} r_G ([Cl]_e - [Cl]_i^I)\right). \tag{4.55}$$

We considered I^E as a proxy for the EEG signal of the NMM. This simulated EEG signal was filtered with a second order Butterworth bandpass filter using cut-off frequencies at 0.5 and 30 Hz.

4.4 Model validation

To examine the behaviour of the network model and NMM under physiological and pathophysiolocial conditions, the models underwent the following tests:

1. Response to external input,
2. Response to ATP depletion,
3. Response to ATP depletion while receiving external input,
4. Recovery of neurons after ATP depletion plus the response to an external input.

During these tests, we also checked if both models satisfied the requirements summarized in subsections 4.2.1 and 4.3.1. The network of coupled spiking single cells was used to validate the NMM by comparing the behaviour of both models to each other. In addition, this would show if the underlying single cell behaviour of the NMM corresponded to the single cell behaviour of the network model. Similar to Dijkstra et al. (2016), the effect of blockage of voltage-gated sodium channels on neural recovery was also tested during the fourth test. Table 4.1 and 4.2 summarize the specific test values for the network model and NMM, respectively.

Moreover, we collected a 30s epoch from a continuous EEG recording of one patient from Medisch Spectrum Twente (a large hospital in Enschede, The Netherlands). The patient was admitted to the intensive care unit after a cardiac arrest and died after suffering a second cardiac arrest. The EEG was recorded during this second arrest. We selected this patient since the EEG still showed a continuous rhythm after the first arrest. The EEG signal was filtered with a band pass filter between 0.5 Hz and 30 Hz to remove possible artifacts. Furthermore, this EEG sample was used to validate our models by comparing it to the simulated signal of both models during complete ATP depletion. Lastly, we performed bifurcation analysis of the NMM to gain more insight into the dynamic behaviour of the model. This analysis was performed using MatCont[16].

Table 4.1: Overview of values used for conducting tests with network of single cells.

Test	I_{app}^{max} (µA/cm^2)	t_{app}^{start} (ms)	t_{app}^{end} (ms)	f_{ATP}	t_{ATP}^{start} (ms)	t_{ATP}^{end} (ms)
1a	0.9	1000	2000	-	-	-
1b	1.0	1000	2000	-	-	-
2a	-	-	-	0.9	1000	-
2b	-	-	-	1.0	1000	-
3a	0.9	1000	2500	0.2	2000	-
3b	0.9	1000	2500	1.0	2000	-
4a	1.0	20000	20500	1.0	2000	6000
4b*	1.0	20000	20500	1.0	2000	6000

[*] Voltage-gated sodium channels were blocked for $t \in [6000, 17000]$.

Table 4.2: Overview of values used for conducting tests with NMM.

Test	f_{ext}^{max} (ms^{-1})	t_{ext}^{start} (ms)	t_{ext}^{end} (ms)	f_{ATP}	t_{ATP}^{start} (ms)	t_{ATP}^{end} (ms)
1a	0.02	1000	2000	-	-	-
1b	0.05	1000	2000	-	-	-
2a	-	-	-	0.9	1000	-
2b	-	-	-	1.0	1000	-
3a	0.02	1000	2500	0.2	2000	-
3b	0.02	1000	2500	1.0	2000	-
4a	0.02	20000	20500	1.0	2000	6000
4b	0.02	4000	5000	1.0	2000	6000

5 | Results

This chapter shows the results of all tests performed with the network of coupled spiking single cells and the NMM: firstly, the response to external input; secondly, the response to ATP depletion; thirdly, the response to ATP depletion while receiving external input and lastly, the recovery of the neurons after ATP depletion followed by the response to an external input. The simulated EEG results of the third test were compared to a real EEG signal. Moreover, we compared the outcome of both models to each other per test. Next, we present the results of the (bifurcation) analysis of the models.

5.1 External input

Network model

The network of coupled spiking single cells shows a continuous resting membrane potential of -65 mV prior to applying an external input (Figure 5.1). An external input of 0.9 μA/cm^2 results in spike activity with a frequency of 11.5 Hz (Figure 5.1A). Applying a stronger input of 1.0 μA/cm^2 leads to an increased spike frequency of 21 Hz and prolonged spiking behaviour (Figure 5.1B). This difference in frequency is also observed in the EEG signals.

NMM

The membrane potential of both neural masses is stable and has a value of approximately -65 mV during rest. Applying a transient input of 0.02 ms^{-1} to the NMM results in small oscillations of the membrane potentials of both neural populations with a frequency of 11.1 Hz (Figure 5.2A). The frequency of these oscillations increases to 21.8 Hz when a stronger external input of 0.05 ms^{-1} is applied (Figure 5.2B). The oscillations are also visible in the simulated EEG signals. Opening of (a fraction of) the AMPA receptors results in an increase of the firing rate of both neural populations. Inhibition occurs when the GABA$_A$ receptors open.

Comparison

The models show comparable results. They are both stable during rest and, as a requirement, the resting membrane potentials are -65 mV in both models. Moreover, applying an external input results in (alpha-) rhythmic behaviour which is also visible in the simulated EEG signals of the network model and NMM. Due to the sigmoid curves of Equation 4.21 and 4.53, there is a gradual increase and decrease of the external input. As a result, prolonged spiking behaviour occurs for higher external inputs as the threshold for spiking is crossed earlier when the input increases and crossed later when the input decreases. Thus, the longer duration of the spiking behaviour is not solely the result of the stronger external input itself.

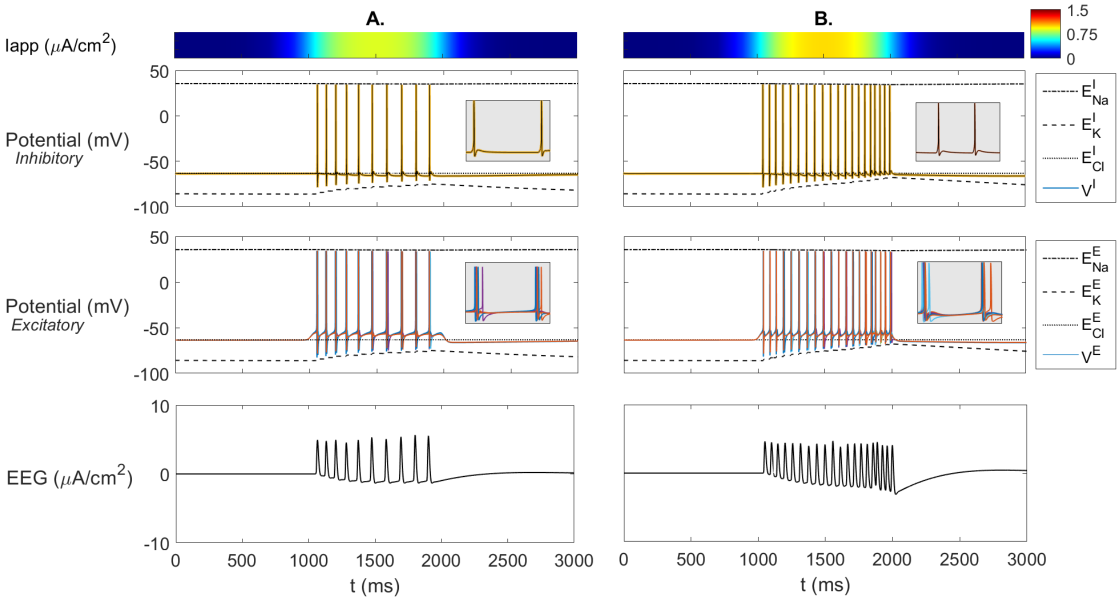

Figure 5.1: **Response of network model to external input.** The color bar indicates the strength of the external input. The upper panels show the behaviour of the inhibitory neurons, the middle panels show the behaviour of excitatory neurons and the bottom panels show the simulated EEG signal. The membrane potential of each single neuron is plotted. The mean values of E_{Na}, E_K and E_{Cl} of the inhibitory and excitatory neurons are shown. Insets show a zoomed-in view of the (heterogenic) spiking behaviour. A. Response to an external input of 0.9 μA/cm^2 applied between 1000 en 2000 ms. The resulting spike frequency is 11.5 Hz. B. Response to an external input of 1.0 μA/cm^2 applied between 1000 en 2000 ms. The resulting spike frequency is 21 Hz.

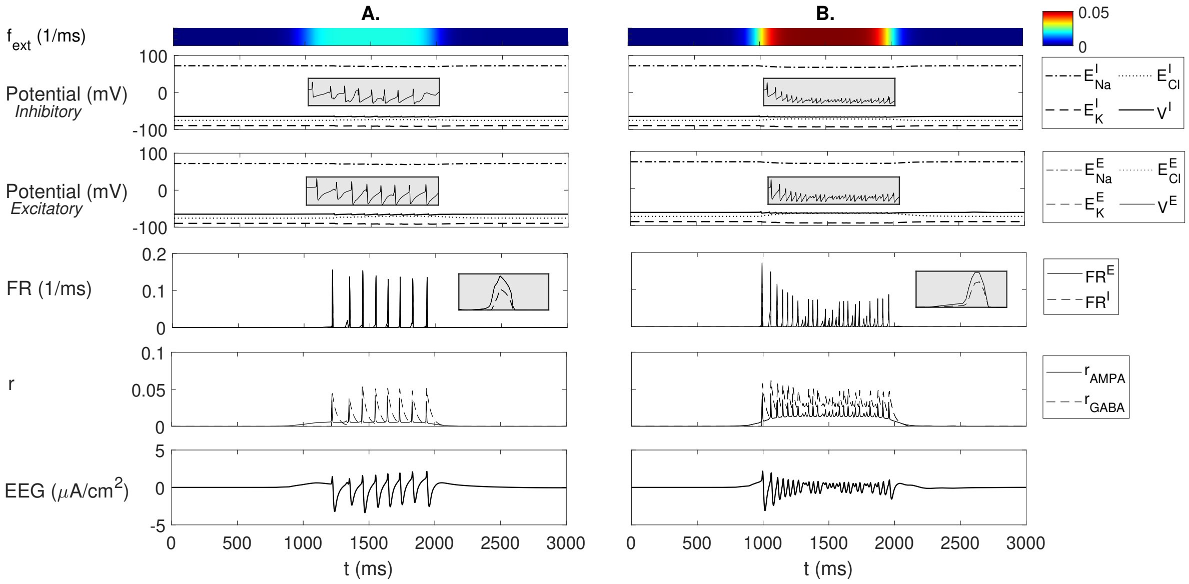

Figure 5.2: **Response of NMM to external input.** The color bar indicates the strength of the external, excitatory input. The upper panels show the behaviour of the inhibitory mass and the panels on the second row show the behaviour of the excitatory mass. The panels on the third and fourth row show the behaviour of the firing rate and the fraction of open AMPA and GABA$_A$ receptors, respectively. The bottom panels show the simulated EEG signal. Insets display a zoomed-in view of the periodic behaviour. A. Response to an external input of 0.02 ms^{-1} applied between 1000 en 2000 ms. The frequency of the oscillations is 11.1 Hz. B. Response to an external input of 0.05 ms^{-1} applied between 1000 en 2000 ms. The frequency of the oscillations is 21.8 Hz.

5.2 ATP depletion

Network model

In this second experiment, the amount of available ATP was lowered during simulation. During a 50% deprivation of ATP, the resting membrane potential of all neurons increases to approximately -63.5 mV, making the neurons slightly more excitable. When the amount of available ATP drops below 24%, depolarization of the membrane potentials occurs. In addition, an almost immediate increase of the membrane potentials of approximately 7 mV is observed when the amount of ATP is below 24%. Lowering the ATP supply to 10% of baseline value results in depolarization of the membrane potentials approximately 650 ms after ATP depletion (Figure 5.3A). Complete cessation of ATP supply accelerates the time till depolarization, which now occurs 380 ms after ATP depletion (Figure 5.3B). After depolarization, the membrane potentials settle at a new equilibrium of approximately -13 mV. Changes in E_{Cl} are delayed and difficult to see. These changes are more clearly visible in subsection 5.4. Moreover, a wave-like pattern can be observed in the simulated EEG signals during depolarization of the membrane potentials. Again, this is more clearly visible during recovery, as discussed in subsection 5.4.

NMM

We also lowered the ATP levels during simulation of the NMM. Decreasing the amount of ATP to 10% of baseline leads to a minor increase of the membrane potentials, E_K and E_{Cl} of both neural populations (Figure 5.4A). A small decrease of E_{Na} is observed as well. There is no increase of the firing rate as the receptors of AMPA and GABA$_A$ do not open and the corresponding EEG signal is flat. When no ATP is left, the receptors of AMPA and GABA$_A$ open, which results in a fast increase of the firing rate. This leads to depolarization of the membrane potential. Soon after, the receptors close, the firing rate becomes zero and the membrane potentials, including the Nernst potentials, of both neural masses settle at a new, GD equilibrium of approximately -19 mV (Figure 5.4B). Furthermore, the simulated EEG signal shows a large amplitude wave when the membrane potentials depolarize.

Comparison

Both models meet the requirements: the membrane potentials settle at a nonzero GD equilibrium after depolarization following ATP deprivation and the simulated EEG signals show a high amplitude slow wave after complete ATP cessation. Comparison of both models shows that depolarization of the membrane potentials occurs already at ATP levels of 24% or lower in the network model of coupled spiking single cells, but only at 0% in the NMM.

5.3 External input plus ATP depletion

Network model

Applying external input and simultaneously lowering the amount of available ATP can show how neural activity is affected by ATP depletion. We applied an external input of 0.9 μA/cm^2 to the network of coupled spiking single cells. Lowering the amount of ATP to 80% of normal values leads to an increase of the spike frequency from 11.5 Hz to 26.2 Hz (Figure 5.5A). Complete cessation of ATP supply leads initially to an increase of the spike frequency from 11.5 Hz to 30.2 Hz. This is followed by depolarization of the membrane potential and flattening of the simulated EEG signal (Figure 5.5B).

NMM

Lowering the amount of available ATP to 80% hardly has an effect on (the frequency of) the oscillations (Figure 5.6A). Only a complete stop of ATP supply results in depolarization of the membrane potentials of both neural masses and a resulting depolarization block (Figure 5.6B).

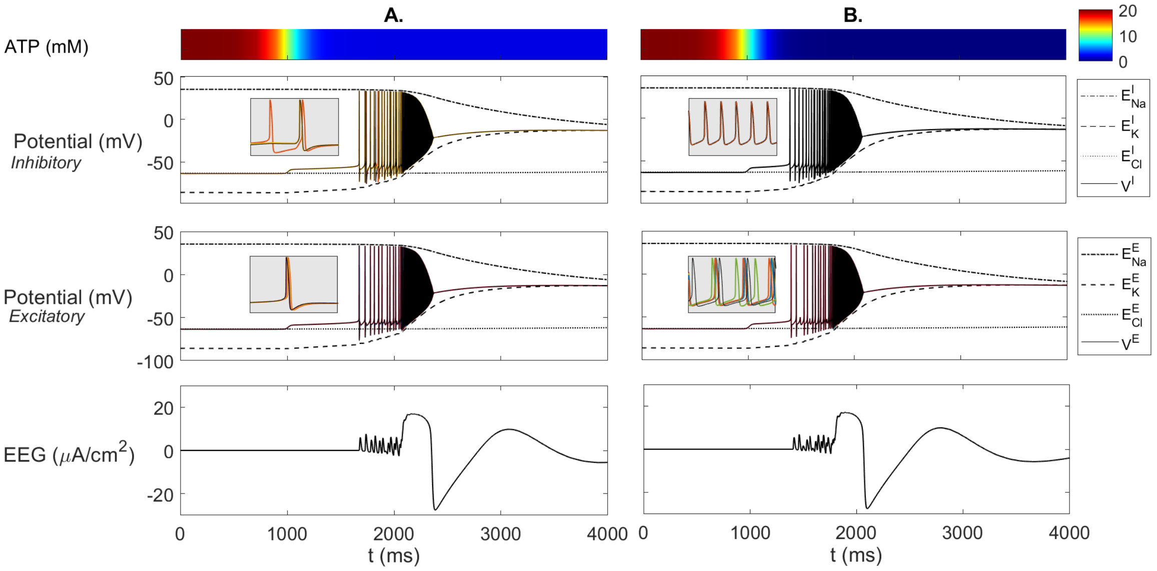

Figure 5.3: **Response of network model to ATP depletion.** The color bar indicates the amount of available ATP. The initial (baseline) value of ATP was 20 mM. The upper panels show the behaviour of the inhibitory neurons, the middle panels show the behaviour of the excitatory neurons and the bottom panels show the simulated EEG signal. The membrane potential of each single neuron is plotted. The mean values of E_{Na}, E_K and E_{Cl} of the inhibitory and excitatory neurons are shown. The insets show a zoomed-in view of the spiking behaviour at approximately 1800 ms. A. The amount of ATP was lowered to 10% at 1000 ms. Depolarization occurs at 1650 ms. A large wave is visible in the EEG signal during depolarization. B. The amount of ATP was lowered to 0% at 1000 ms. Depolarization occurs at 1380 ms. A large wave is visible in the EEG signal during depolarization.

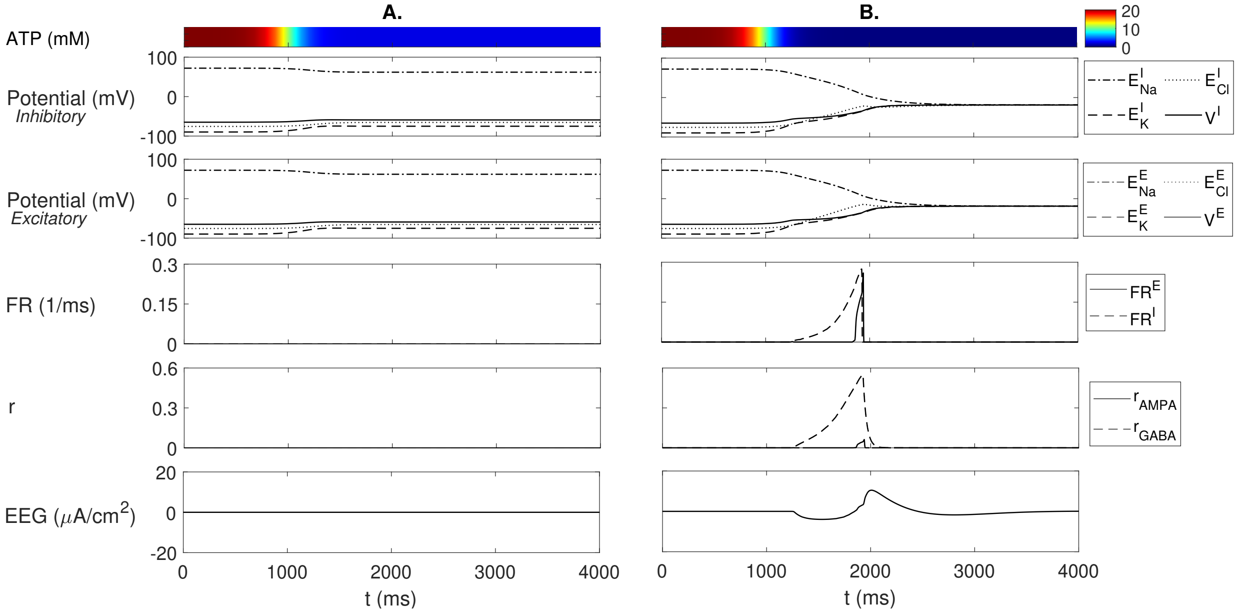

Figure 5.4: **Response of NMM to ATP depletion.** The color bar indicates the amount of available ATP. The initial (baseline) value of ATP was 20 mM. The upper panels show the behaviour of the inhibitory mass and the panels on the second row show the behaviour of the excitatory mass. The panels on the third and fourth row show the behaviour of the firing rate and the fraction of open AMPA and GABA$_A$ receptors, respectively. The bottom panels show the simulated EEG signal. A. The amount of ATP was lowered to 10% at 1000 ms. B. The amount of ATP was lowered to 0% at 1000 ms. This results in depolarization of the membrane potentials. A large wave is visible in the EEG signal during depolarization.

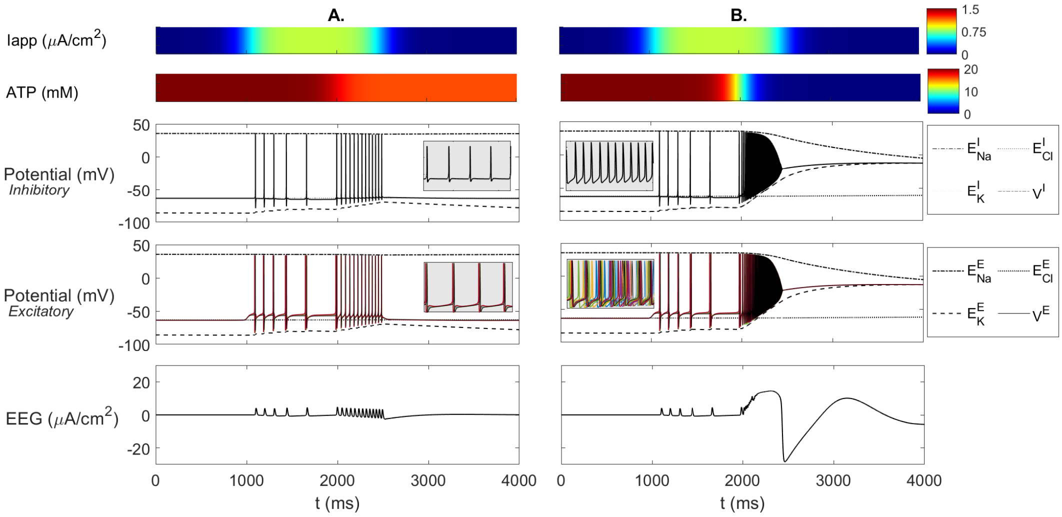

Figure 5.5: **Response of network model to external input during ATP deprivation.** The first color bar indicates the strength of the external input. In both figures, an external input of 0.9 μA/cm^2 was applied for $t \in [1000{,}2500]$. The second color bar indicates the level of available ATP. The initial (baseline) value of ATP was 20 mM. The upper panels show the behaviour of the inhibitory neurons, the middle panels show the behaviour of the excitatory neurons and the bottom panels show the resulting EEG signal. The insets show a zoomed-in view of the spiking behaviour after ATP deprivation at approximately 2100 ms. A. The amount of ATP was lowered to 80% at 2000 ms. The spike frequency increases from 11.5 to 26.2 Hz. B. The amount of ATP was lowered to 0% at 2000 ms. The spike frequency increases from 11.5 Hz to 30.2 Hz. This is followed by depolarization of the potentials.

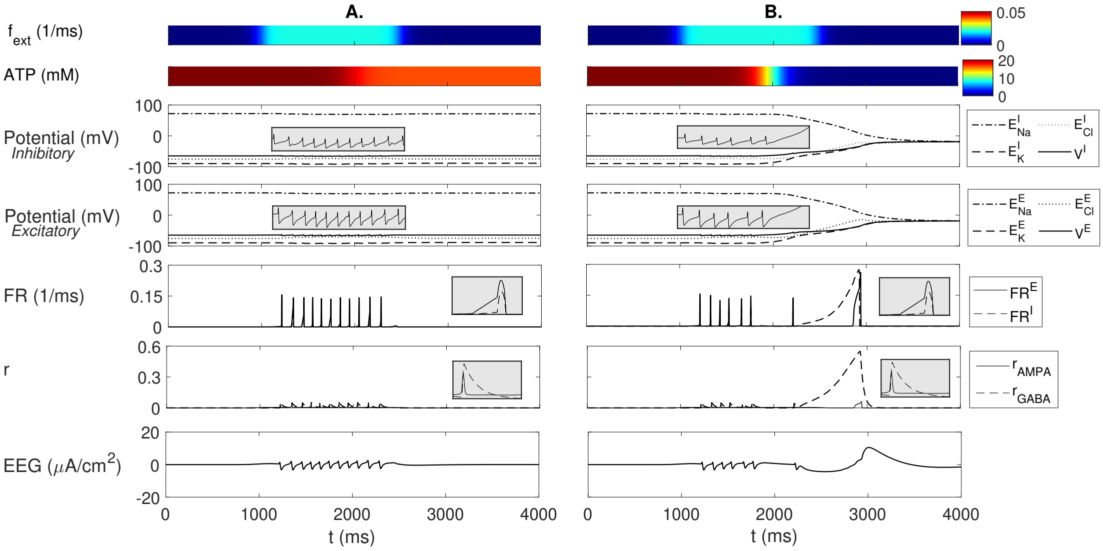

Figure 5.6: **Response of NMM to external input during ATP deprivation.** The first color bar indicates the strength of the external input. In both figures, an external input of 0.02 ms^{-1} was applied for $t \in [1000{,}2500]$. The second color bar indicates the level of available ATP. The initial (baseline) value of ATP was 20 mM. The upper panels show the behaviour of the inhibitory mass and the panels on the second row show the response of excitatory mass. The panels on the third and fourth row show the behaviour of firing rate and the fraction of open AMPA and GABA$_A$ receptors, respectively. The bottom panels show the simulated EEG signal. A zoomed-in view of the periodic behaviour is displayed in the grey insets. A. The amount of ATP was lowered to 80% at 2000 ms. This does not change the frequency of the oscillations. B. The amount of ATP was lowered to 0% at 2000 ms. This results in depolarization of the membrane potentials. A large wave is visible in the EEG signal during depolarization.

Comparison

Similar to the results of the second test, the network of coupled spiking single cells is more sensitive to a change in ATP supply compared to the NMM. During complete ATP cessation, both models show similar results regarding the frequency of the periodic behaviour. The next paragraph explains this in more detail.

Comparison to real EEG signal

A second cardiac arrest was captured during EEG recordings, as shown in Figure 5.7. The dotted red lines indicate transitions in the EEG rhythm. After the first line, slowing of the EEG rhythm is observed. This is followed by silencing of the signal, visible after the second line. The electrocardiogram signal, indicating the electrical activity of the heart, was measured as well. However, the signal is not shown here as the electrodes were probably not properly attached, resulting in a signal with many artifacts.

Neither the simulated EEG signal of the network of single cells, nor the simulated EEG signal of the NMM during full ATP depletion shows a result comparable to the real EEG signal. The variation of frequency over time during cessation of ATP is shown in Figure 5.8. The frequency of both the network model and NMM initially increases when ATP levels drop, while slowing was expected based on the real EEG signal. Silencing of the simulated EEG signals of both models is eventually also visible.

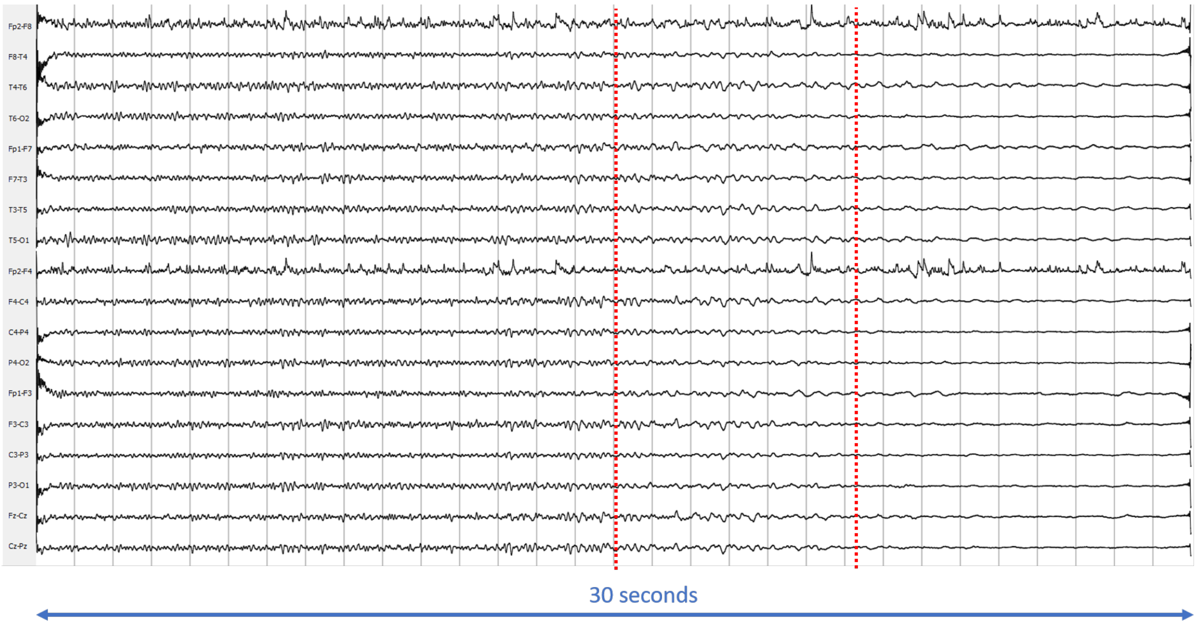

Figure 5.7: **EEG recording of a (second) cardiac arrest.** Changes in EEG rhythm are indicated by the dotted red lines. Slowing of the EEG signal is observed (first line), which is followed by suppression of the signal (second line). The first and ninth channel contain artifacts, mainly visible after the second red line.

5.4 Recovery after ATP depletion

Network model

The network of coupled spiking single neurons shows that the membrane potentials do not return to their resting state when ATP levels are fully restored and the pumps have regained their original strength (Figure 5.9A). A delayed increase of E_{Cl} up to the new equilibrium of approximately -13 mV is now more clearly visible. Additionally, the model does not respond to an external input of 1.0 μA/cm^2 which was applied after recovery of ATP levels. According to Dijkstra et al. (2016), (partial) depolarization of

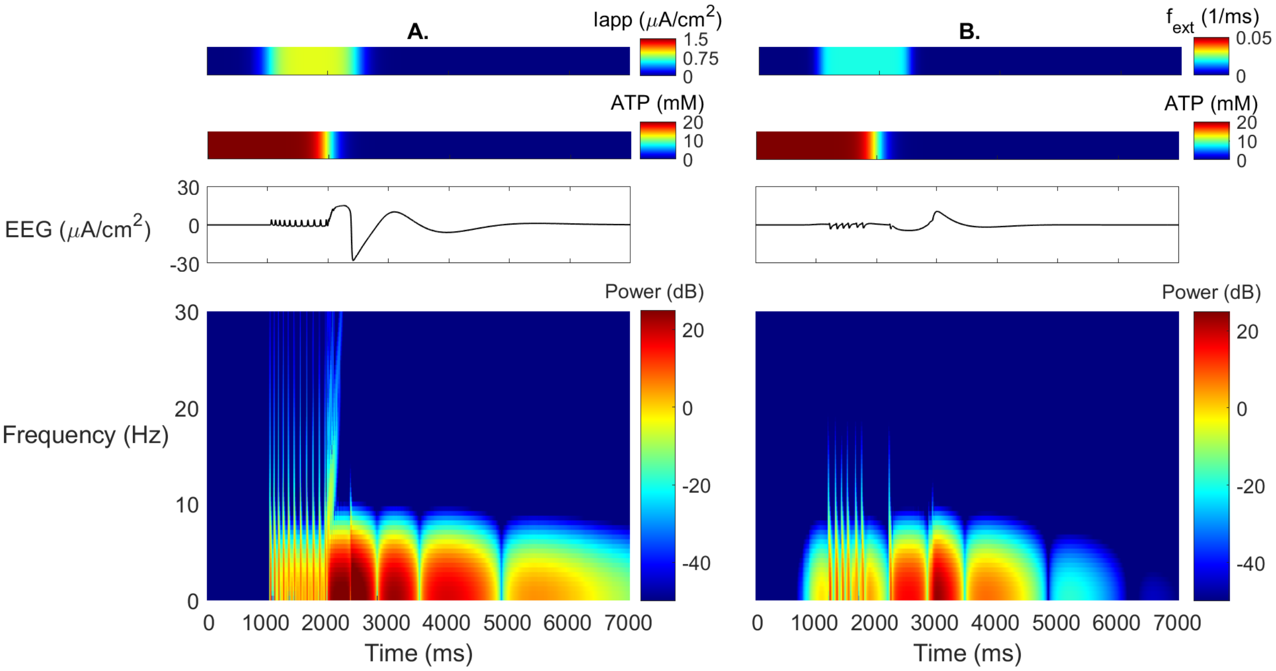

Figure 5.8: **Effect of complete ATP depletion on EEG frequency.** The time-frequency plots have a frequency resolution of 0.82 Hz and a time resolution of 313 ms. In both plots, the power of higher frequencies initially increases after ATP depletion. This is followed by a decrease of the EEG frequency and silencing of the simulated EEG signal. A. Frequency response of network of coupled spiking single cells. An external input of 0.9 μA/cm^2 was applied. B. Frequency response of NMM. An external input of 0.02 ms^{-1} was applied.

the membrane potential is associated with an increased sodium permeability. The NKAs might not be able to overcome the resulting sodium current[17]. The recovery of membrane potentials is stimulated by blocking the voltage-gated sodium channels. The membrane potentials return to their resting value of -65 mV after a temporal, but complete blockade of the transient sodium current. Thereby we mimicked the effect of administering a sodium channel blocker like tetrodotoxin. After removing the blockade, we observe a response to an external current of 1.0 μA/cm^2 (Figure 5.9B). Furthermore, a large slow wave is observed on the simulated EEG of the network model during ATP depletion which resembles the "Wave of Death" as simulated by Zandt et al. (2011) (See Figures 3.4 and 5.9)[79].

NMM

Restoring the ATP supply in the NMM leads to an immediate response of the system (Figure 5.10A). The membrane potentials of both neural masses hyperpolarize, due to a dip in E_K, before they settle at the resting value of -65 mV. Applying an external input of 0.02 ms^{-1} after restoring ATP levels, results in a response of the NMM. Recovery of the membrane potential already happens without blocking voltage-gated sodium channels. Blocking the channels does not result in a different response and so, no result of this test is shown. Instead, we applied an external input of 0.02 ms^{-1} while the membrane was depolarized (Figure 5.10B). As expected from the result of the network model, the NMM shows no response to this stimulus. Furthermore, a "Wave of Death"-like signal is observed on the simulated EEG of the NMM during depolarization of the membrane potential. This is visible on the bottom panels of Figure 5.10.

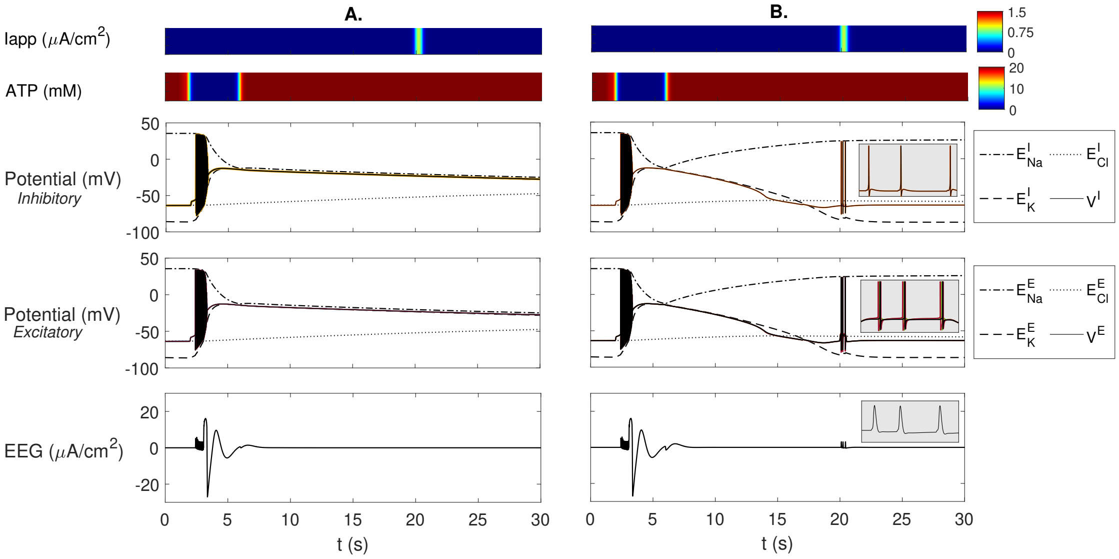

Figure 5.9: **Recovery of network model after complete ATP depletion.** The first color bar indicates the strength of the external input and the second color bar indicates the level of available ATP. The upper panels show the behaviour of the inhibitory neurons, the middle panels show the behaviour of the excitatory neurons and the bottom panels show the resulting EEG signal. A. The amount of ATP is fully restored after $t = 6$ s. No response to an external input applied for $t \in$ [20,20.5] is visible. B. Together with fully restoring the amount of ATP after $t = 6$ s, the effect of e.g. tetrodotoxin is simulated by blocking voltage-gated sodium channels for $t \in$ [6,17]. The membrane potentials return to their baseline values and a response to an external input applied between $t \in$ [20,20.5] is visible. The insets show a zoomed-in view of the response to the external input.

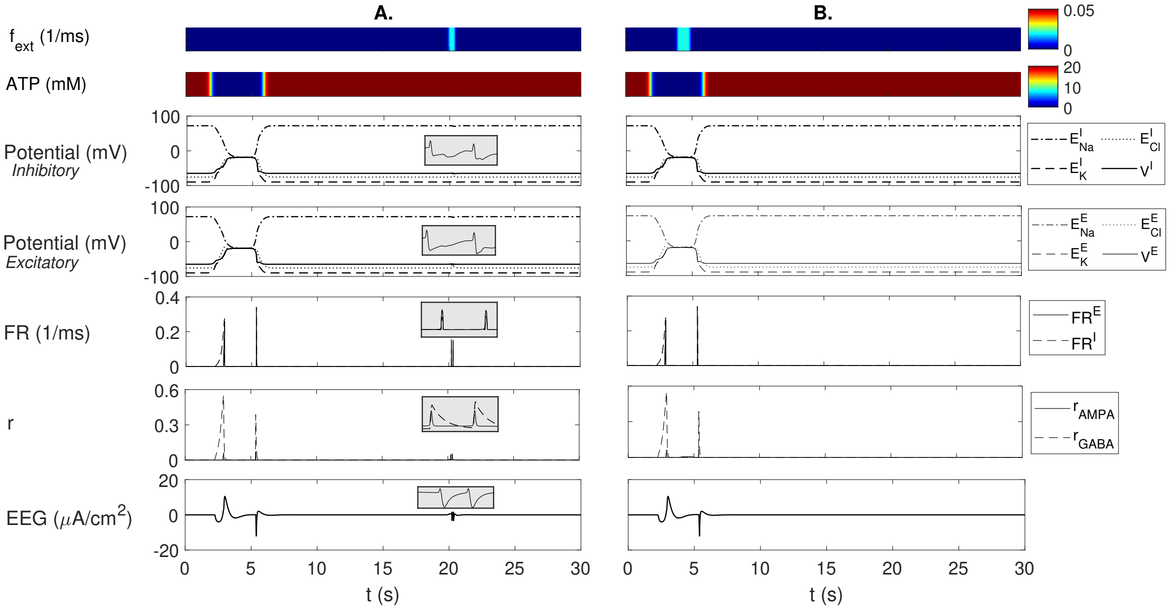

Figure 5.10: **Recovery of NMM after complete ATP depletion.** The first color bar indicates the strength of the external input and the second color bar indicates the level of available ATP. The upper panels show the response of the excitatory mass and the panels on the second row show the response of inhibitory mass. The panels on the third row show the behaviour of the firing rate and the bottom panels show the fraction of open AMPA and GABA$_A$ receptors. A. An external input of 0.02 ms^{-1} is applied after recovery of the membrane potential. The insets show a zoomed-in view of the response to this external input. B. An external input of 0.02 ms^{-1} is applied while the membrane potentials are still depolarized. No response is visible.

Comparison
The initial response of both models to ATP depletion is similar. However, the models respond differently to restoration of the ATP supply. An immediate recovery of the membrane potentials of the NMM is visible, while the membrane potentials of the network of coupled spiking single cells only recover when voltage-gated sodium channels are temporarily blocked.

In both models, a large slow wave can be observed on the simulated EEG signal during depolarization of the membrane potentials. The membrane potentials can still recover after occurrence of this wave.

5.5 Model analysis

Figure 5.11 shows the response frequency of the network model of coupled spiking single cells and the NMM to external input. Both models react to an external input when this input exceeds a threshold value of approximately 0.85 μA/cm^2 for the network of coupled spiking single cells and approximately 0.016 ms^{-1} for the NMM. The shapes of the graphs are similar: an increase of the external input leads to an increase of the response frequency. A more rapid increase of the response frequency is visible when the input is higher than 2.0 μA/cm^2 for the network of coupled spiking single cells and approximately 0.052 ms^{-1} for the NMM. Furthermore, the response frequency becomes zero after reaching a maximal input value, indicating the occurrence of a depolarization block.

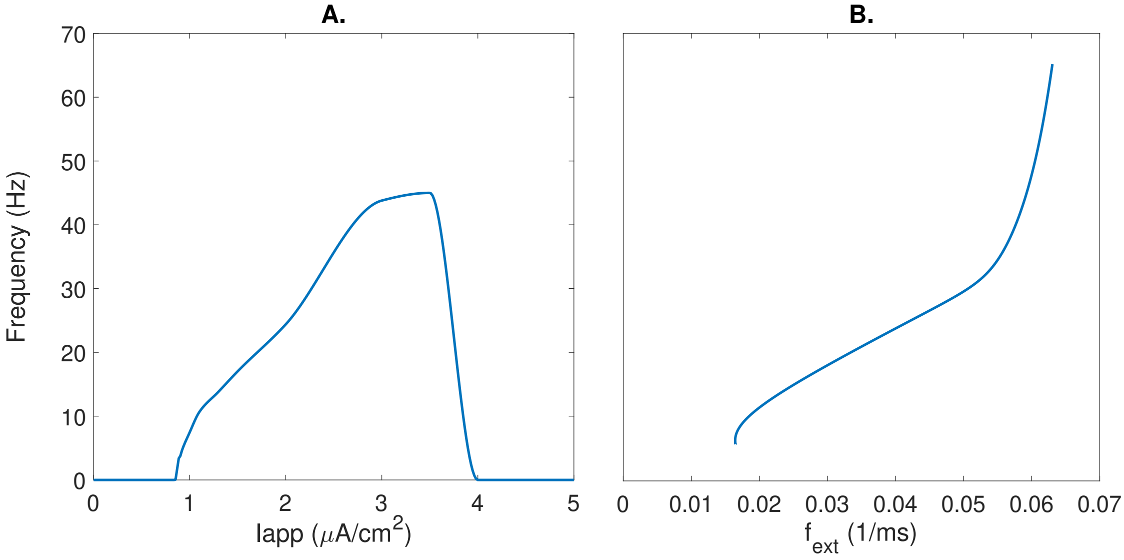

Figure 5.11: **Response frequency to external input.** ATP levels are at baseline value of 20 mM. When the external input exceeds a specific threshold, the models react to this input. After reaching a maximal input value, the response frequency becomes zero and a depolarization block occurs. A. (Mean) response frequency of excitatory cells in network of spiking single cells. B. Response frequency of NMM.

We studied the dependency of the NMM on the external input using bifurcation analysis. Figure 5.12 shows the corresponding bifurcation diagram with f_{ext} as a free parameter. The strength of external input f_{ext} determines the qualitative dynamics of the model. Three possible responses of the membrane potentials are observed when external input is applied. These responses, plus the observed simulated EEG signals, are:

1. a small increase of the membrane potential,	simulated EEG is flat,
2. continuous periodic behaviour,	simulated EEG shows continuous periodic behaviour,
3. transient periodic behaviour,	simulated EEG shows transient periodic behaviour.

The continuous, periodic behaviour arises from a supercritical Hopf bifurcation. The closer f_{ext} is to the Hopf bifurcation, the smaller the amplitude of the periodic behaviour. When f_{ext} exceeds the corresponding value of the Hopf bifurcation, transient periodic behaviour is visible.

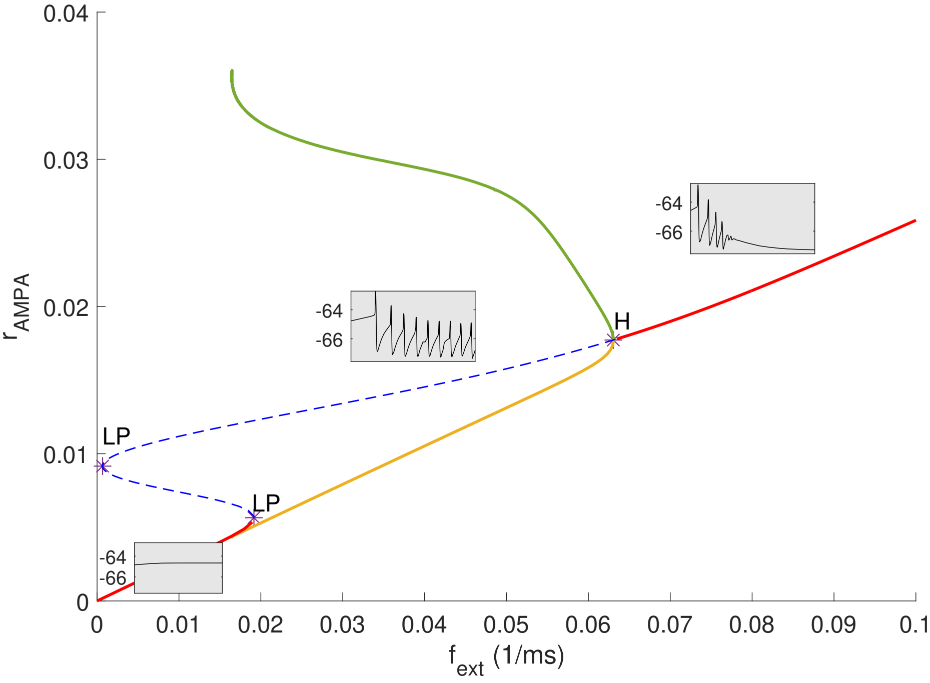

Figure 5.12: **Bifurcation diagram of ATP-dependent NMM with f_{ext} as free parameter.** Stable equilibria are denoted by a solid red line, and unstable equilibria are denoted by a dashed blue line. The green and yellow lines indicate the maximum and minimum values of r_{AMPA} at the stable limit cycle, respectively. The H indicates a supercritical Hopf bifurcation, giving rise to a stable limit cycle. At an external input of 0.196 ms^{-1} or higher, the system shows periodic behaviour. The insets show qualitative dynamics of the membrane potential of the excitatory mass with the y-axis in mV at different positions in the bifurcation diagram. Transient periodic behaviour is visible when f_{ext} is higher than the value corresponding to the Hopf bifurcation.

6 | Discussion

To the best of our knowledge, we are the first to construct a network model of coupled spiking single cells and NMM including NKAs. This is achieved by an ion-based formulation. Our models offer the possibility to tune the amount of available ATP, and thus, the strength of the NKAs, during simulations to examine the effect of ATP depletion on the neural activity at macroscopic scale. We derived a new equation for this firing rate based on the dynamics of a single cell as the Nernst potentials of sodium and potassium influence the population firing rate.

A lot of computational models exist in the field of neuroscience, but models focusing on ATP deprivation are scarce. Our models show similar behaviour as the single cell models of Zandt et al. (2011)[79] and Dijkstra et al. (2016)[17] during deprivation of ATP. The so-called "Wave of Death" is visible in our network model and NMM. Furthermore, both models show depolarization of the cell membrane towards a GD equilibrium as well. However, several differences between our models and other computational models exist as well. First, it is possible to tune the amount of ATP during the simulations with our models which is not possible in the model of Zandt et al. (2011). Hence, the behaviour of our model prior to complete cessation of ATP can be investigated. Secondly, there is a difference in scale. Our models provide a unique extension by including the NKA and ATP dependency at a macroscopic scale, while the two previously mentioned models are both at microscopic scale. Thirdly, a big difference between our NMM and previously constructed NMMs is the fact that ion concentrations are the base instead of average membrane potentials. This paves the road for a new kind of models and their study. Section 6.2 further discusses the clinical relevance of this approach.

As shown in Figure 3.5A, the physiological state disappears in the network of coupled spiking single cells when the amount of available ATP drops below 24% and the membrane potential depolarizes. This is similar to the model behaviour described by Dijkstra et al. (2016). The membrane potential settles at a new (pathological) equilibrium potential. This corresponds to the GD equilibrium state, which is also named a 'state of free energy-starvation' due to the almost complete dissipation of energy[17]. Only the change in E_{Cl} is much slower compared to changes in E_K and E_{Na}. Hence, it takes longer before E_{Cl} equals the GD equilibrium potential. Possible causes of this delayed E_{Cl} are the smaller permeability of chloride and a less dominant influence of the KCL cotransporters compared to the NKAs. In accordance with Dijkstra et al. (2016), we show with our network of single cells that membrane potentials return to physiological values after blocking the voltage-gated sodium channels[17]. Without blocking these channels, NKAs are not able to compensate for the sodium currents. Initially, no difference is visible on the simulated EEG signal between the situations with and without blocking the channels. By applying an external current, the underlying differences become visible as the neurons only respond to the stimulus when membrane potentials have returned to their physiological baseline. This corresponds to the clinical use of electrophysiological brain responses to a stimulus. These responses are used for assessing the brain function and predicting the outcome of comatose patients as they may be indicative of recovery after (postanoxic)coma[71]. Furthermore, it is remarkable that the NMM shows a mild response when ATP levels reach 10% of baseline. Only complete cessation of ATP leads to a depolarization block in the NMM and settling of the potentials at a GD equilibrium. The membrane potentials and Nernst potentials of both neural populations recover as soon as ATP increases. Blocking voltage-gated sodium channels does not provide different results. A potential cause of these deviant responses are the strengths of the NKAs. In contrast to the pumps of the network of single spiking cells, the pumps of the NMM are strong enough to overcome the sodium current. As explained in Appendix C, the strength of the pumps influences the leak permeabilities as well. By decreasing the pump strengths, the constraints ($P_{Na}^L > 0$, $P_K^L > 0$ and $P_{Cl}^L > 0$) could not be satisfied. Moreover, lowering the ATP levels to 10% has less impact on these stronger pumps compared to the ones of the network. During other, yet unpublished, research at the University of Twente, it was shown that the size of the ECS influences the response of the neuron during recovery of ATP levels. The smaller the ECS, the harder it is for a neuron to recover. We investigated if the size of the ECS had influence on our model as well. Changing the size of the ECS resulted in no difference at all or a (numerical) error which could not be resolved. The results are therefore not published in this report. In addition, an initial increase of the membrane potential was visible when the ATP levels dropped below 24% in the network model or when the ATP levels were 0% in the NMM. This value corresponds to the direct electrogenic contribution of NKAs to the membrane potential which is approximately 5 to 10 mV[1].

As required, both models show normal neural activity under physiological conditions. The network of coupled spiking single cells responds to an external input current by producing spikes. The spike frequency depends on the strength of the input current. This spiking behaviour cannot be simulated with the NMM as it requires fast dynamics of the activation and inactivation gates m, n and h, whose steady-state versions were used in the NMM. In our NMM model, continuous periodic behaviour of the membrane potential are observed in response to an external input. This behaviour arises once the system undergoes a (supercritical) Hopf bifurcation. During such a bifurcation, the stability of the system switches and a limit cycle is born. This behaviour was also observed in the HH cell used to determine the new firing rate curve. The periodic behaviour becomes transient when the input exceeds the value corresponding to the Hopf bifurcation.

Similar to Zandt et al. (2011), we did not consider any ATP buffers[79]. Incorporating these reserves would postpone the response of the models to ATP depletion. It is thought that this does not change the dynamics of the model. Moreover, the strength of the NKAs is immediately affected by a decrease of ATP. However, it is questionable if the maximal pump strengths are reached under normal ATP levels and normal activity levels or if the pump strengths can (temporarily) become higher when necessary, e.g. during ATP depletion. This could potentially postpone depolarization of the membrane potentials. It is thought that this has no impact on the model behaviour.

Although the network of spiking cells and the NMM show behaviour comparable to each other and other computational models, their outcome does not correspond to the real EEG signal shown in Figure 5.7. An initial increase of the firing frequency is observed in the computational models, while the EEG shows slowing of the frequencies. Also literature reports that slowing of the EEG signal is expected (see Figure 2.1)[20]. We ascribe the increased firing rate to an increased neural excitability. This happens due to a decrease of the strength of the NKAs resulting in an increase of E_K and a decrease of E_{Na}. Apparently, a decreased function of the NKAs alone, does not result in the expected behaviour. Hence, the question remains which underlying mechanisms are responsible for the slowing of the EEG rhythm. Mild to moderate ischemia can result in synaptic failure[28]. This failure might result from presynaptic damage associated with impaired transmitter release and is a potential candidate for the slowing of the EEG signal. We have shortly tested this with our network of single neurons by diminishing the fraction of open (AMPA) receptors during ATP depletion. As none of the outcomes shows a decrease in firing rate, the results are not published in this report. It is recommended to investigate the mechanisms behind loss of fast frequencies and increase of slower frequencies further. Suggestions are changes in the synaptic coupling strengths and the loss of synchrony between neurons. According to Coombes and Byrne (2019), a change in power of the EEG signal can be due to variation of synchrony within a neural mass[12]. Moreover, ATP depletion has a similar effect on all inhibitory and all excitatory neurons in our models. However, different types of neurons have different sensitivity to ischemia which can play a role in the slowing of EEG as well[20].

We observe a large slow wave in both of our models. As the neurons can still recover once ATP is restored, we agree with Zandt et al. (2011) that calling this wave ‘cerebral anoxic depolarization’ might be more appropriate than ‘Wave of Death’[79]. The wave occurs much earlier in our models compared to the one of Zandt et al. (2011). This difference can be ascribed to differences is parameter values, e.g. the ratio between ICS and ECS. The connections between the neurons might play a role in accelerating depolarization as well. Remarkably, during previous (unpublished) research at Medisch Spectrum Twente, it was concluded that the "Wave of Death" is not visible in real EEG signals after cardiac arrest. It is speculated that simultaneous loss of resting membrane potential causes the wave[73]. As suggested earlier, loss of synchrony might be the reason why the wave is not visible on the human EEG. However, it is yet unknown why the human EEG does not show this behaviour, while experimental (animal) studies confirm the existence of the wave.

6.1 Limitations

One of the obvious limitations of our models, and computational models in general, is simplification of the neural network. First, we only considered temporal aspects and disregarded all spatial aspects. We assumed a spatially homogeneous model to be appropriate as a cardiac arrest results in diffusely disturbed CBF[58]. Extending the NMM to a spatio-temporal NMM offers the opportunity to use the model for research regarding local CBF-related conditions like cerebral infarction. Secondly, only the NKA was considered while many more ATP-dependent processes are affected during ATP depletion. Due to the extensiveness of the project, this was out of the scope of this research. We elaborate on this topic in Section 6.3.

Furthermore, experimental data for calibration and validation of our NMM were scarce. This complicated finding proper values for our variables. Therefore, we determined several values based on empirical findings. The computational models were also compared to EEG data of only one patient. More EEG data of patients during a cardiac arrest are difficult to acquire as the occurrence of such an event is unpredictable and rare. Chances are small that a second cardiac arrest is captured on the EEG of patients in postanoxic coma who still have rhythmic output. Nevertheless, the EEG is in accordance with literature and thus, we consider it useful for our research[20]. Other options to acquire more data for further research are to compare the outcome of this study to EEG data of patients undergoing carotid surgery, undergoing a tilt table test or with the outcome of animal studies. Besides, we assumed that our excitatory and inhibitory neuron are representative to simulate the mean behaviour of an excitatory and inhibitory population in the NMM. Moreover, the firing rate curve is based on one single HH neuron only. By smoothing the curve, we did not only avoid numerical instabilities, but we also introduced spreading in the behaviour of the neural population and thus, heterogeneity, to correct for this limitation.

Although we based parts of our models on the cytotoxic cell swelling model of Dijkstra et al. (2016), we have chosen not to incorporate cell swelling itself to limit the complexity of the model. However, a strong predictor of functional outcome of comatose patients after cardiac arrest is the occurrence and severity of cerebral edema[66]. Therefore, we recommend to implement cell swelling mechanisms in the model during future research.

6.2 Clinical relevance

The network of single neurons and the NMM provide insight in the neural activity during ATP deprivation following cardiac arrest. This contributes to understanding the underlying pathophysiological mechanisms, which is of great importance for improving the outcome prediction and treatment of several medical conditions like cardiac arrest. However, we cannot (yet) match the computational models to the real EEG signal and the NMM should be optimized to produce the desired behaviour. Therefore, the gap between the NMM and clinical use is still quite big. Nevertheless, its clinical potential is large. Not only can it lead to new research possibilities in the medical field concerning cardiac arrests, it can also be of major benefit for research regarding ischemic cerebral infarction, brain hemorrhage and other medical conditions in which a lack of oxygen and glucose causes serious problems to the brain.

As far as we know, this is not only the first NMM containing NKAs, but also the first NMM based on ion concentrations. This model provides a base for studying neural activity in diseases in which ion concentrations deviate from normal, e.g. in Alzheimer's Disease. In this disease, a decreased level of NKAs together with impaired clearance of glutamate can result in an impairment of cellular ion homeostasis[74]. Moreover, we tested the effect of blocking the voltage-gated sodium currents during restoration of ATP levels. The ion-based NMM can be used to simulate the effect of drugs targeting ion channels or channelopathies on neural activity.

6.3 Recommendations

We focused on the effects of ATP deprivation on NKAs and the resulting effects of failure of these pumps. However, ATP depletion affects many more processes in the brain. As we have not yet uncovered the underlying mechanisms responsible for slowing of the EEG rhythm during cardiac arrest, we recommend to extend the model by incorporating other ATP-dependent processes as well. Synaptic failure can occur, which might be caused by presynaptic malfunctioning and impaired release of neurotransmitters[27]. Moreover, the effects of extracellular glutamate can be considered as well. Approximately 90% of all extracellular glutamate is removed by astrocytes. This clearance happens after glutamate diffuses from the synaptic cleft to the ECS and requires ATP[44]. According to Orfila et al. (2018), there is an enormous increase of extracellular glutamate within minutes after the onset of ischemia. Reverse glutamate uptake by astrocytes occurs in isolated Müller cells. This happens after strong membrane depolarization due to failure of the NKA in tissue exposed to ischemia[57]. Excessive amounts of extracellular glutamate induces so called ischaemic long-term potentiation. This is the strengthening of the connection between neurons[52]. Ruijter et al. (2017) incorporated long-term potentiation in their model[58]. The new NMM might eventually even be linked to this previously published NMM to gain additional insights in the response of neuronal populations to ATP depletion and the aftermath of this depletion. A final extension of the model is modelling the neurovascular coupling (NVC). Neural activity and CBF are linked by a mechanism known as NVC. Although it is suggested that brain integrity and functionality can be compromised due to failure of the NVC caused by low oxygen levels during cardiac arrest, the effect of hypoxia on the NVC is not fully known, neither are the possibilities to restore the coupling mechanism.

Furthermore, we have chosen to construct a NMM consisting of only two neural populations. This is the minimum representation of a NMM. We did not make a distinction within the excitatory nor inhibitory population as was done in the Jansen-Rit model[33]. They included a population of excitatory interneurons. The Wendling model, which is an extension of the Jansen-Rit model, even has two inhibitory populations: slow and fast inhibitory interneurons. More types of activity can be simulated with these models. We recommend to investigate if this improves the NMM.

Our last recommendation is to perform a more extensive bifurcation analysis on the NMM. This can be of added value to expose underlying dynamics and further deepen the understanding of the model behaviour. To show slowing of the frequencies, as seen in the real EEG signal, we expect to find a homoclinic bifurcation. We recommend a slow-fast analysis to investigate this hypothesis. The NMM can be divided in a slow and fast subsystem: ion dynamics of the NMM are much slower than the synaptic dynamics. By regarding the ions as slow parameters, it might be possible to find a homoclinic bifurcation or other bifurcations in the fast subsystem. As the slow manifold is six dimensional, this will probably be a difficult task.

7 | Conclusion

In conclusion, our models fill a gap in the field of computational neuroscience. We constructed two macroscopic models consisting of ATP-dependent NKAs. Moreover, the NMM was based on ion concentrations. We showed how the models react to external input and ATP depletion and investigated the response to recovery of ATP levels. The behaviour of the models is similar to the behaviour of other computational models. However, their behaviour during cessation of ATP does not correspond to a real EEG signal and thus, the underlying mechanisms responsible for slowing of the EEG rhythm during cardiac arrest remain unknown. We recommend to perform further research to discover these mechanisms, e.g. expanding the models by incorporating more ATP-dependent processes and implementing cell swelling. Although we acknowledge several limitations in our research, this study is a starting point for future models to investigate and understand underlying pathophysiological mechanisms of neural diseases influenced by ATP deprivation and/or an imbalance of ion concentrations.

Bibliography

[1] T.R. Anderson, J.R. Huguenard, and D.A. Prince. Differential effects of Na+-K+ ATPase blockade on cortical layer V neurons. *Journal of Physiology*, 588(22):4401–4414, 2010. ISSN 00223751. doi: 10.1113/jphysiol.2010.191858.

[2] A. Banerjee, K.E. Borgmann-Winter, R. Ray, and C.G. Hahn. The PSD: A Microdomain for Converging Molecular Abnormalities in Schizophrenia. In *The neurobiology of Schizophrenia*, pages 125–147. Elsevier, 2016.

[3] E. Barreto and J.R. Cressman. Ion concentration dynamics as a mechanism for neuronal bursting. *Journal of Biological Physics*, 37(3):361–373, 2011. ISSN 00920606. doi: 10.1007/s10867-010-9212-6.

[4] S.B. Blumberg. *Model Fitting and Parameter Estimation of Neural Mass Models*. PhD thesis, Vrije Universiteit Amsterdam and Universiteit van Amsterdam, 2015.

[5] I. Bojak and D.T.J. Liley. Modeling the effects of anesthesia on the electroencephalogram. *Physical Review E - Statistical, Nonlinear, and Soft Matter Physics*, 71(4):1–22, 2005. ISSN 15393755. doi: 10.1103/PhysRevE.71.041902.

[6] I. Bojak, Z.V. Stoyanov, and D.T.J. Liley. Emergence of spatially heterogeneous burst suppression in a neural field model of electrocortical activity. *Frontiers in Systems Neuroscience*, 9(FEB):1–20, 2015. ISSN 16625137. doi: 10.3389/fnsys.2015.00018.

[7] C. Börgers, S. Epstein, and N.J. Kopell. Background gamma rhythmicity and attention in cortical local circuits: A computational study. *Proceedings of the National Academy of Sciences of the United States of America*, 102(19):7002–7007, 2005. ISSN 00278424. doi: 10.1073/pnas.0502366102.

[8] L. S. Borkowski. Bistability and resonance in the periodically stimulated Hodgkin-Huxley model with noise. *Physical Review E - Statistical, Nonlinear, and Soft Matter Physics*, 83(5):1–8, 2011. ISSN 15393755. doi: 10.1103/PhysRevE.83.051901.

[9] W.F. Boron and E.L. Boulpaep. The nervous system. In *Medical Physiology*, pages 265–426. Saunders Elsevier, second edition, 8 2009. ISBN 9781416031154.

[10] I. Chamma, Q. Chevy, J.C. Poncer, and S. Lévi. Role of the neuronal K-Cl co-transporter KCC2 in inhibitory and excitatory neurotransmission. *Frontiers in Cellular Neuroscience*, 6(JAN.):1–15, 2012. ISSN 16625102. doi: 10.3389/fncel.2012.00005.

[11] B.S. Chander and V.S. Chakravarthy. A Computational Model of Neuro-Glio-Vascular Loop Interactions. *PLoS ONE*, 7(11):1–11, 2012. ISSN 19326203. doi: 10.1371/journal.pone.0048802.

[12] S. Coombes and A. Byrne. Next Generation Neural Mass Models. In *Nonlinear Dynamics in Computational Neuroscience*, pages 1–16. Springer, 2019. doi: 10.1007/978-3-319-71048-8{_}1.

[13] S. Coombes and C. Laing. Delays in activity-based neural networks. *Philosophical Transactions of the Royal Society A: Mathematical, Physical and Engineering Sciences*, 367(1891):1117–1129, 2009. ISSN 1364503X. doi: 10.1098/rsta.2008.0256.

[14] P. Dayan and L.F. Abbott. *Theoretical Neuroscience: Computational and Mathematical modeling of neural systems*. MIT press, 2001. ISBN 0262041995. doi: 10.1086/461850.

[15] A. Destexhe and T.J. Sejnowski. The Wilson-Cowan model, 36 years later. *Biological Cybernetics*, 101(1):1–2, 2009. ISSN 03401200. doi: 10.1007/s00422-009-0328-3.

[16] A. Dhooge, W. Govaerts, Y.A. Kuznetsov, H.G.E. Meijer, and B. Sautois. New features of the software MatCont for bifurcation analysis of dynamical systems. *Mathematical and Computer Modelling of Dynamical Systems*, 14(2):147–175, 2008. ISSN 13873954. doi: 10.1080/13873950701742754.

[17] K. Dijkstra, J. Hofmeijer, S.A. van Gils, and M.J.A.M. van Putten. A Biophysical Model for Cytotoxic Cell Swelling. *The Journal of Neuroscience*, 36(47):11881–11890, 2016. ISSN 0270-6474. doi: 10.1523/JNEUROSCI.1934-16.2016.

[18] J. Elmer and Cl.W. Callaway. The brain after cardiac arrest. *Seminars in Neurology*, 37(1):19–24, 2017. ISSN 10989021. doi: 10.1055/s-0036-1597833.

[19] G.B. Ermentrout and D.H. Terman. The Hodgkin – Huxley Equations. In *Mathematical Foundations of Neuroscience*, chapter 3, pages 1–28. Springer, 2010. ISBN 9780387877082. doi: 10.1007/978-0-387-87708-2.

[20] B. Foreman and J. Claassen. Quantitative EEG for the Detection of Brain Ischemia. In *Annual Update in Intensive Care and Emergency Medicine 2012*, pages 746 – 758. Springer, 2012. ISBN 9783642257162. doi: 10.1007/978-3-642-25716-2.

[21] A.A. Gorshkov, S.A. Plotnikov, and A.L. Fradkov. Bifurcation and synchronization analysis of neural mass model subpopulations. *IFAC-PapersOnLine*, 50(1):14741–14745, 2017. ISSN 24058963. doi: 10.1016/j.ifacol.2017.08.2577.

[22] J.T. Gräsner, R. Lefering, R.W. Koster, S. Masterson, B.W. Böttiger, J. Herlitz, J. Wnent, I.B.M. Tjelmeland, F.R. Ortiz, H. Maurer, M. Baubin, P. Mols, I. Hadžibegović, M. Ioannides, R. Škulec, M Wissenberg, A. Salo, H. Hubert, N.I. Nikolaou, G. Lóczi, H. Svavarsdóttir, F. Semeraro, P.J. Wright, C. Clarens, R. Pijls, G. Cebula, V.G. Correia, D. Cimpoesu, V. Raffay, S. Trenkler, A. Markota, A. Strömsöe, R. Burkart, G.D. Perkins, and L.L. Bossaert. EuReCa ONE—27 Nations, ONE Europe, ONE Registry: A prospective one month analysis of out-of-hospital cardiac arrest outcomes in 27 countries in Europe. *Resuscitation*, 105:188–195, 2016. ISSN 18731570. doi: 10.1016/j.resuscitation.2016.06.004.

[23] F. Grimbert and O. Faugeras. Analysis of Jansen's model of a single cortical column. *[Research Report]*, RR-5597(INRIA):34. inria–00070410, 2006.

[24] Hartstichting. Hartstilstand, 2020. URL `https://www.hartstichting.nl/hart-en-vaatziekten/hartstilstand`.

[25] W.M. Hascheck, C.G. Rousseaux, M.A. Wallig, B. Bolon, and R. Ochoa. *Haschek and Rousseauch's handbook of toxicologic*

pathology. Academic Press Inc., 3rd edition, 2013. ISBN 9780124157590.

[26] A.L. Hodgkin and A.F. Huxley. A quantitative description of membrane current and its application to conduction and excitation in nerve. *The Journal of Physiology*, 117(4):500–544, 1952. doi: 10.1109/ICCCT2.2017.7972284.

[27] J. Hofmeijer and M.J.A.M. van Putten. Ischemic cerebral damage: An appraisal of synaptic failure. *Stroke*, 43(2):607–615, 2012. ISSN 00392499. doi: 10.1161/STROKEAHA.111.632943.

[28] J. Hofmeijer, M.C. Tjepkema, N. Gaspard, and M.J.A.M. van Putten. EEG binnen 24 uur na hartstilstand is een betrouwbare voorspeller van uitkomst van postanoxisch coma. *Tijdschrift voor Neurologie en Neurochirurgie*, 117(2):55–62, 2016.

[29] N. Hübel and M.A. Dahlem. Dynamics from Seconds to Hours in Hodgkin-Huxley Model with Time-Dependent Ion Concentrations and Buffer Reservoirs. *PLoS Computational Biology*, 10(12), 2014. ISSN 15537358. doi: 10.1371/journal.pcbi.1003941.

[30] N. Hübel, E. Schöll, and M.A. Dahlem. Bistable Dynamics Underlying Excitability of Ion Homeostasis in Neuron Models. *PLoS Computational Biology*, 10(5), 2014. ISSN 15537358. doi: 10.1371/journal.pcbi.1003551.

[31] E.M. Izhikevich. *Dynamical systems in neuroscience: The geometry of excitability and bursting*. MIT press, 2007. ISBN 9780262514200.

[32] B.H. Jansen and V.G. Rit. Electroencephalogram and visual evoked potential generation in a mathematical model of coupled cortical columns. *Biological Cybernetics*, 73(4):357–366, 1995. ISSN 03401200. doi: 10.1007/BF00199471.

[33] B.H. Jansen, G. Zouridakis, and M.E. Brandt. A neurophysiologically-based mathematical model of flash visual evoked potentials. *Biological Cybernetics*, 68(3):275–283, 1993. ISSN 03401200. doi: 10.1007/BF00224863.

[34] H.Y. Jeong and B. Gutkin. Synchrony of neuronal oscillations controlled by GABAergic reversal potentials. *Neural Computation*, 19(3):706–729, 2007. ISSN 08997667. doi: 10.1162/neco.2007.19.3.706.

[35] P. Johns. Stroke. In *Clinical Neuroscience E-Book: An illustrated Colour Text*, chapter 10, pages 115–128. Elsevier Health Sciences, 2014. ISBN 9780702057137.

[36] A.R. Kay. How cells can control their size by pumping ions. *Frontiers in Cell and Developmental Biology*, 5(MAY):1–14, 2017. ISSN 2296634X. doi: 10.3389/fcell.2017.00041.

[37] P.D. King, J. Zylberberg, and M.R. Deweese. Inhibitory interneurons decorrelate excitatory cells to drive sparse code formation in a spiking model of V1. *Journal of Neuroscience*, 33(13):5475–5485, 2013. ISSN 02706474. doi: 10.1523/JNEUROSCI.4188-12.2013.

[38] C. Koch and I. Segev. Kinetic Models. In *Methods in neuronal modeling: from ions to networks*, chapter 1, pages 1–25. MIT press, 1998. ISBN 9780262112314.

[39] P. Kumar and M.L. Clark. Cardiovascular disease. In *Clinical Medicine*, pages 681–811. Elsevier Health Sciences, seventh ed edition, 2009.

[40] D. Liang, S. Bhatta, V. Gerzanich, and J.M. Simard. Cytotoxic edema: mechanisms of pathological cell swelling. *Neurosurgical focus*, 22(5):1–9, 2007. ISSN 10920684. doi: 10.3171/foc.2007.22.5.3.

[41] D.T.J. Liley, P.J. Cadusch, and M.P. Dafilis. A spatially continuous mean field theory of electrocortical activity. *Network: Computation in Neural Systems*, 13(1):67–113, 2002. ISSN 0954898X. doi: 10.1088/0954-898X/13/1/303.

[42] V. Lopantsev and P.A. Schwartzkroin. GABAA-Dependent Chloride Influx Modulates GABAB-Mediated IPSPs in Hippocampal Pyramidal Cells. *Journal of Neurophysiology*, 82(3):1218–1223, 9 1999. ISSN 0022-3077. doi: 10.1152/jn.1999.82.3.1218.

[43] F.H. Lopes da Silva, A. Hoeks, H. Smits, and L.H. Zetterberg. Model of brain rhythmic activity - The alpha-rhythm of the thalamus. *Kybernetik*, 15(1):27–37, 1974. ISSN 03401200. doi: 10.1007/BF00270757.

[44] S. Mahmoud, M. Gharagozloo, C. Simard, and D. Gris. Astrocytes Maintain Glutamate Homeostasis in the CNS by Controlling the Balance between Glutamate Uptake and Release. *Cells*, 8(2):184, 2019. doi: 10.3390/cells8020184.

[45] J. Malmivuo and R. Plonsey. *Bioelectromagnetism - Principles and Applications of Bioelectric and Biomagnetic Fields*. Oxford University Press, 10 1995. ISBN 9780195058239. doi: 10.1093/acprof:oso/9780195058239.001.0001.

[46] R. Moran, D.A. Pinotsis, and K. Friston. Neural masses and fields in dynamic causal modelling. *Frontiers in Computational Neuroscience*, 7(APR 2013):1–12, 2013. ISSN 16625188. doi: 10.3389/fncom.2013.00057.

[47] G. Mukandala, R. Tynan, S. Lanigan, and J.J. O'Connor. The effects of hypoxia and inflammation on synaptic signaling in the CNS. *Brain Sciences*, 6(1), 2016. ISSN 20763425. doi: 10.3390/brainsci6010006.

[48] A. Myat, K.J. Song, and T. Rea. Out-of-hospital cardiac arrest: current concepts. *The Lancet*, 391(10124):970–979, 2018. ISSN 1474547X. doi: 10.1016/S0140-6736(18)30472-0.

[49] A.H.O. Olde Engberink, J.H. Meijer, and S. Michel. Chloride cotransporter KCC2 is essential for GABAergic inhibition in the SCN. *Neuropharmacology*, 138:80–86, 2018. ISSN 18737064. doi: 10.1016/j.neuropharm.2018.05.023.

[50] A.C.E. Onslow, M.W. Jones, and R. Bogacz. A canonical circuit for generating phase-amplitude coupling. *PLoS ONE*, 9(8), 2014. ISSN 19326203. doi: 10.1371/journal.pone.0102591.

[51] CNX OpenStax. Neurons and Glial Cells, 2013. URL `http://cnx.org/content/col11448/latest/`.

[52] J.E. Orfila, N. McKinnon, M. Moreno, G. Deng, N. Chalmers, R.M. Dietz, P.S. Herson, and N. Quillinan. Cardiac Arrest Induces Ischemic Long-Term Potentiation of Hippocampal CA1 Neurons That Occludes Physiological Long-Term Potentiation. *Neural Plasticity*, 2018:1–9, 2018. ISSN 2090-5904. doi: 10.1155/2018/9275239.

[53] T.J. Petros and S.A. Anderson. Tangential Migration. In *Cellular Migration and Formation of Neuronal Connections*, chapter 20, pages 363–376. Elsevier, first edition, 2013. doi: 10.1016/B978-0-12-397266-8.00031-4.

[54] D.A. Pinotsis, M. Leite, and K.J. Friston. On conductance-based neural field models. *Frontiers in Computational Neuroscience*, 7 (NOV):1–9, 2013. ISSN 16625188. doi: 10.3389/fncom.2013.00158.

[55] D.A. Pinotsis, P. Robinson, P.B. Graben, and K. Friston. Neural masses and fields: Modeling the dynamics of brain activity. *Frontiers in Computational Neuroscience*, 8(NOV):2013–2015, 2014. ISSN 16625188. doi: 10.3389/fncom.2014.00149.

[56] C. Rink and S. Khanna. Significance of Brain Tissue Oxygenation and the Arachidonic Acid Cascade in Stroke. *Antioxidants & Redox Signaling*, 14(10):1889–1903, 2010. ISSN 1523-0864. doi: 10.1089/ars.2010.3474. URL `http://www.liebertonline.com/doi/abs/10.1089/ars.2010.3474`.

[57] C.R. Rose, L. Felix, A. Zeug, D. Dietrich, A. Reiner, and C. Henneberger. Astroglial Glutamate Signaling and Uptake in the Hippocampus. *Frontiers in Molecular Neuroscience*, 10(January):1–20, 1 2018. ISSN 1662-5099. doi: 10.3389/fnmol.2017.00451.

[58] B.J. Ruijter, J. Hofmeijer, H.G.E. Meijer, and M.J.A.M. van Putten. Synaptic damage underlies EEG abnormalities in postanoxic encephalopathy: A computational study. *Clinical Neurophysiology*, 128(9):1682–1695, 2017. ISSN 18728952. doi: 10.1016/j.clinph.2017.06.245.

[59] R.L. Rungta, H.B. Choi, J.R. Tyson, A. Malik, L. Dissing-Olesen, P.J.C. Lin, S.M. Cain, P.R. Cullis, T.P. Snutch, and B.A. Macvicar. The cellular mechanisms of neuronal swelling underlying cytotoxic edema. *Cell*, 161(3):610–621, 2015. ISSN 10974172. doi: 10.1016/j.cell.2015.03.029.

[60] P. Sanz-Leon, S.A. Knock, A. Spiegler, and V.K. Jirsa. Mathematical framework for large-scale brain network modeling in The Virtual Brain. *NeuroImage*, 111:385–430, 2015. ISSN 10959572. doi: 10.1016/j.neuroimage.2015.01.002.

[61] M.S. Sekhon, P.N. Ainslie, and D.E. Griesdale. Clinical pathophysiology of hypoxic ischemic brain injury after cardiac arrest: A "two-hit" model. *Critical Care*, 21(1):1–10, 2017. ISSN 1466609X. doi: 10.1186/s13054-017-1670-9.

[62] L.A. Shimoda and J. Polak. Hypoxia. 4. Hypoxia and ion channel function. *American Journal of Physiology - Cell Physiology*, 300 (5), 2011. ISSN 03636143. doi: 10.1152/ajpcell.00512.2010.

[63] H. Singh and I. Singh. Nerve Muscle Physiology. In *Fundamentals of Medical Physiology*, chapter 7, pages 391–433. Elsevier, 2018. ISBN 978-81-312-5409-7.

[64] L. Sondag, B.J. Ruijter, M.C. Tjepkema-Cloostermans, A. Beishuizen, F.H. Bosch, J.A. van Til, M.J.A.M. van Putten, and J. Hofmeijer. Early EEG for outcome prediction of postanoxic coma: Prospective cohort study with cost-minimization analysis. *Critical Care*, 21(1), 2017. ISSN 1466609X. doi: 10.1186/s13054-017-1693-2.

[65] R.C. Sotero. Modeling the Generation of Phase-Amplitude Coupling in Cortical Circuits: From Detailed Networks to Neural Mass Models. *BioMed Research International*, 2015(December), 2015. ISSN 23146141. doi: 10.1155/2015/915606.

[66] J.A. Stokum, V. Gerzanich, and J.M. Simard. Molecular pathophysiology of cerebral edema. *Journal of Cerebral Blood Flow and Metabolism*, 36(3):513–538, 2016. ISSN 15597016. doi: 10.1177/0271678X15617172.

[67] I.I. Stoyanova, J. Hofmeijer, M.J.A.M. van Putten, and J. le Feber. Acyl Ghrelin Improves Synapse Recovery in an In Vitro Model of Postanoxic Encephalopathy. *Molecular Neurobiology*, 53(9):6136–6143, 2016. ISSN 15591182. doi: 10.1007/s12035-015-9502-x.

[68] M.C. Tjepkema-Cloostermans, C. da Silva Lourenço, B.J. Ruijter, S.C. Tromp, G. Drost, F.H.M. Kornips, A. Beishuizen, F.H. Bosch, J. Hofmeijer, and M.J.A.M. van Putten. Outcome Prediction in Postanoxic Coma With Deep Learning. *Critical care medicine*, 47 (10):1424–1432, 2019. ISSN 15300293. doi: 10.1097/CCM.0000000000003854.

[69] C.L. Torborg and C.J. McBain. INTERNEURONS | Properties of Interneurons and their Relation to Epilepsy. In *Encyclopedia of Basic Epilepsy Research*, pages 625–630. Elsevier, 2009. doi: 10.1016/B978-012373961-2.00125-9.

[70] J. Touboul, F. Wendling, P. Chauvel, and O. Faugeras. Neural Mass Activity, Bifurcations, and Epilepsy. *Neural Computation*, 23 (12):3232–3286, 12 2011. ISSN 0899-7667. doi: 10.1162/NECO{_}a{_}00206.

[71] A. Tzovara, A. Simonin, M. Oddo, A.O. Rossetti, and M. De Lucia. Neural detection of complex sound sequences in the absence of consciousness. *Brain*, 138(5):1160–1166, 2015. ISSN 14602156. doi: 10.1093/brain/awv041.

[72] M.J.A.M. Van Putten, J. Hofmeijer, B.J. Ruijter, and M.C. Tjepkema-Cloostermans. Deep learning for outcome prediction of postanoxic coma. In *IFMBE Proceedings*, volume 65, pages 506–509. Springer Verlag, 2017. ISBN 9789811051210. doi: 10.1007/978-981-10-5122-7{_}127.

[73] C.M. van Rijn, H. Krijnen, S Menting-Hermeling, and A.M.L. Coenen. Decapitation in rats: Latency to unconsciousness and the 'wave of death'. *PLoS ONE*, 6(1):1–6, 2011. ISSN 19326203. doi: 10.1371/journal.pone.0016514.

[74] V.M. Vitvitsky, S.K. Garg, R.F. Keep, R.L. Albin, and R. Banerjee. Na + and K + ion imbalances in Alzheimer's disease. *Biochimica et Biophysica Acta - Molecular Basis of Disease*, 1822(11):1671–1681, 2012. ISSN 09254439. doi: 10.1016/j.bbadis.2012.07.004.

[75] F. Wendling, F. Bartolomei, J.J. Bellanger, and P. Chauvel. Epileptic fast activity can be explained by a model of impaired GABAergic dendritic inhibition. *European Journal of Neuroscience*, 15(9):1499–1508, 2002. ISSN 0953816X. doi: 10.1046/j.1460-9568.2002.01985.x.

[76] H.R. Wilson and J.D. Cowan. Excitatory and Inhibitory Interactions in Localized Populations of Model Neurons. *Biophysical Journal*, 12(1):1–24, 1972. ISSN 00063495. doi: 10.1016/S0006-3495(72)86068-5.

[77] W. Yang and Q.Q. Sun. Circuit-specific and neuronal subcellular-wide E-I balance in cortical pyramidal cells. *Scientific Reports*, 8 (1):1–15, 2018. ISSN 20452322. doi: 10.1038/s41598-018-22314-9.

[78] B.J. Zandt. *Neuronal activity and ion homeostasis in the hypoxic brain*. PhD thesis, University of Twente, 2014.

[79] B.J. Zandt, B. ten Haken, J.G. van Dijk, and M.J.A.M. van Putten. Neural dynamics during anoxia and the "wave of death". *PLoS ONE*, 6(7):3–8, 2011. ISSN 19326203. doi: 10.1371/journal.pone.0022127.

[80] B.J. Zandt, T. Stigen, B. ten Haken, T. Netoff, and M.J.A.M. van Putten. Single neuron dynamics during experimentally induced anoxic depolarization. *Journal of Neurophysiology*, 110(7):1469–1475, 2013. ISSN 00223077. doi: 10.1152/jn.00250.2013.

[81] B.J. Zandt, S. Visser, M.J.A.M. van Putten, and B. ten Haken. A neural mass model based on single cell dynamics to model pathophysiology. *Journal of Computational Neuroscience*, 37(3):549–568, 2014. ISSN 15736873. doi: 10.1007/s10827-014-0517-5.

[82] L.H. Zetterberg, L. Kristiansson, and K. Mossberg. Performance of a model for a local neuron population. *Biological Cybernetics*, 31(1):15–26, 1978. ISSN 03401200. doi: 10.1007/BF00337367.

A Model Parameters

The physiological interpretation of the parameters and their values are given in Table A.1 for the network model and Table A.2 for the NMM.

Table A.1: Overview of model parameters, symbols and values of network of single cells

Parameter	Description	Value	Unit
V_0	Resting membrane potential	-65	mV
W_i / W_e	Intracellular / extracellular volume	2160 / 720[30]	μm^3
F	Faraday's constant	96485.333[17]	C·mol^{-1}
R	Universal gas constant	8.3144598[17]	C·V·mol^{-1}K^{-1}
T	Absolute temperature	310[17]	K
g_{KCl}	Flux parameter of KCl cotransporter	7e-3[E]	Ω^{-1}·cm^{-2}
τ_r^E / τ_r^I	Rise constant of excitatory / inhibitory synapse	0.2 / 0.5[7]	ms
τ_d^E / τ_d^I	Decay constant of excitatory / inhibitory synapse	2 / 10[7]	ms
k_s	Slope parameter	10[E]	mV
C_m	Specific membrane capacitance	1[79]	μF·cm^{-2}
g_{Na}	Maximum gated sodium conductance	100[79]	mS·cm^{-2}
g_{NaL}	Sodium leak conductance	0.0175[79]	mS·cm^{-2}
g_K	Maximum gated potassium conductance	40[79]	mS·cm^{-2}
g_{KL}	Potassium leak conductance	0.05[79]	mS·cm^{-2}
g_{ClL}	Chloride leak conductance	0.05[79]	mS·cm^{-2}
ϵ^{EE}	Coupling strength (from excitatory to excitatory neuron)	0.01[7]	mS·cm^{-2}
ϵ^{EI}	Coupling strength (from excitatory to inhibitory neuron)	1.0[7]	mS·cm^{-2}
ϵ^{IE}	Coupling strength (from inhibitory to excitatory neuron)	0.5[7]	mS·cm^{-2}
ϵ^{II}	Coupling strength (from inhibitory to inhibitory neuron)	0.1[7]	mS·cm^{-2}
N^E / N^I	Number of excitatory / inhibitory neurons	4 / 16[E]	-
ϕ	Time constant of gating variables	3[79]	ms^{-1}
ATP_0	Initial neuronal ATP concentration	20[11]	mM
K_{ATP}	Dissociation constant of ATP binding with NKA	170[11]	mM
ρ_p	NKA rate	36.73[E]	μA·cm^{-2}
$[Na^+]_i^0$	Initial intracellular sodium concentration	29.36[E]	mM
$[Na^+]_e^0$	Initial extracellular sodium concentration	111.33[E]	mM
$[K^+]_i^0$	Initial intracellular potassium concentration	125.99[E]	mM
$[K^+]_e^0$	Initial extracellular potassium concentration	5.02[E]	mM
$[Cl^+]_i^0$	Initial intracellular chloride concentration	10.72[E]	mM
$[Cl^+]_e^0$	Initial extracellular chloride concentration	115.51[E]	mM

superscript [E] indicates that the value was found empirically.

Table A.2: Overview of model parameters, symbols and values of NMM.

Parameter	Description	Value	Unit
V^E	mean excitatory soma membrane potential	n.a.	mV
V^I	mean inhibitory soma membrane potential	n.a.	mV
r	radius of spherical neuron	7.82	μm
A	membrane surface of neuron	767.66	μm^2
W_i	Volume of neuron / Volume of intracellular space	2000[17]	μm^3
W_e	Volume of extracelllular space	478.92	μm^3
C	membrane capacitance	20[17]	pF
F	Faraday's constant	96485.333[17]	$\text{C}\cdot\text{mol}^{-1}$
R	universal gas constant	8.3144598[17]	$\text{C}\cdot\text{V}\cdot\text{mol}^{-1}\text{K}^{-1}$
T	absolute temperature	310[17]	K
ATP_0	initial neuronal ATP concentration	20[11]	mM
K_{ATP}	dissociation constant of the ATP binding with NKA	170[11]	mM
ρ_p	NKA rate	54.5[17]	pA
α_A / β_A	opening / closing rate of AMPA receptor	2 / 0.5[E]	ms^{-1}
$\bar{g}_A^E$	maximal conductance of AMPA (to AMPA)	0.17[E]	nS
$\bar{g}_A^I$	maximal conductance of AMPA (to GABA_A)	0.1[38]	nS
α_G / β_G	opening / closing rate of GABA_A receptor	14 / 0.03[E]	ms^{-1}
$\bar{g}_G^E$	maximal conductance of GABA_A (to AMPA)	0.1[E]	nS
$\bar{g}_G^I$	maximal conductance of GABA_A (to GABA_A)	0.05[E]	nS
N_{EE}	number of synaptic connections from E to E population	3000[58]	-
N_{EI}	number of synaptic connections from E to I population	3000[58]	-
N_{IE}	number of synaptic connections from I to E population	500[58]	-
N_{II}	number of synaptic connections from I to I population	500[58]	-
g_{KCl}	Flux parameter of KCl cotransporter	125.43[E]	$\Omega^{-1}\cdot\text{cm}^{-2}$
$[\text{A}^-]_i$	Intracellular impermeant anion concentration	148.0067[E]	mM
$[\text{A}^-]_e$	Extracellular impermeant anion concentration	35[E]	mM
$[\text{Na}^+]_i^{E,0}$	Initial intracellular sodium concentration of E population	10	mM
$[\text{Na}^+]_i^{I,0}$	Initial intracellular sodium concentration of I population	10	mM
$[\text{Na}^+]_e^0$	Initial extracellular sodium concentration	150	mM
$[\text{K}^+]_i^{E,0}$	Initial intracellular potassium concentration of E population	145	mM
$[\text{K}^+]_i^{I,0}$	Initial intracellular potassium concentration of I population	145	mM
$[\text{K}^+]_e^0$	Initial extracellular potassium concentration	5	mM
$[\text{Cl}^-]_i^{E,0}$	Initial intracellular chloride concentration of E population	7	mM
$[\text{Cl}^-]_i^{I,0}$	Initial intracellular chloride concentration of I population	7	mM
$[\text{Cl}^-]_e^0$	Initial extracellular chloride concentration	120	mM
P_{Na}^L	sodium leak permeability	1132[E]	$\mu\text{m}^3\cdot\text{s}^{-1}$
P_K^L	potassium leak permeability	13555[E]	$\mu\text{m}^3\cdot\text{s}^{-1}$
P_{Cl}^L	chloride leak permeability	1931[E]	$\mu\text{m}^3\cdot\text{s}^{-1}$
P_{Na}^T	Maximal transient sodium permeability	800[17]	$\mu\text{m}^3\cdot\text{s}^{-1}$
P_K^D	Maximal delayed rectifier potassium permeability	400[17]	$\mu\text{m}^3\cdot\text{s}^{-1}$
P_{Cl}^G	Maximal voltage-gated chloride permeability	19.5[17]	$\mu\text{m}^3\cdot\text{s}^{-1}$
σ	standard deviation	1[E]	ms^{-1}

superscript [E] indicates that the value was found empirically.

Table A.3: Coefficients of polynomials I_{th}, κ and I_{th2}

Coefficient (I_{th})	**Value**	**Coefficient (κ)**	**Value**	**Coefficient (I_{th2})**	**Value**
p_{00}	-213.8	q_{00}	0.287	r_{00}	-185.9
p_{10}	-8.404	q_{10}	0.01094	r_{10}	-4.877
p_{01}	-3.007	q_{01}	0.001027	r_{01}	-3.674
p_{20}	-0.1111	q_{20}	0.0001692	r_{20}	-0.002785
p_{11}	-0.07862	q_{11}	-8.42e-6	r_{11}	-0.1044
p_{02}	-0.001213	q_{02}	-4.839e-5	r_{02}	0.01561
p_{30}	-0.0005002	q_{30}	8.167e-7	r_{30}	-1.17e-5
p_{21}	-0.0005221	q_{21}	-3.156e-7	r_{21}	1.897e-5
p_{12}	-1.483e-6	q_{12}	-4.421e-7	r_{12}	0.0006927
p_{03}	3.779e-5	q_{03}	2.764e-7	r_{03}	0.0001089

B | Additional information: network of coupled spiking single cells

Here we provide additional information about creating heterogeneity in the network of coupled spiking single cells. We created a heterogeneous neural population by varying the external input per neuron. To maintain this heterogeneity if no external input was applied, each neuron had a slightly different pump strength. The mean values used, can be found in Table A.1. The variations per neuron are summarized below in Table B.1.

Table B.1: Variations per neuron relative to the mean external current and mean pump strength.

Neuron	External current	Pump strength
1	-	+0.1
2	-	-0.1
3	-	+0.2
4	-	-0.2
5	+0.0010	+0.1
6	-0.0010	-0.1
7	+0.0015	+0.2
8	-0.0015	-0.2
9	+0.0020	+0.3
10	-0.0020	-0.3
11	+0.0025	+0.4
12	-0.0025	-0.4
13	+0.0030	+0.5
14	-0.0030	-0.5
15	+0.0035	+0.6
16	-0.0035	-0.6
17	-0.0040	+0.7
18	-0.0040	-0.7
19	+0.0045	+0.8
20	-0.0045	-0.8

C | Additional information: ATP-dependent neural mass model

Here we provide additional information on determining the size of the leak currents in the NMM. The NMM should settle at the resting membrane potential of -65 mV when ATP levels are normal and no external current is applied. To guarantee this, we determined the leak currents based on the strength of NKAs, the strength of the KCL cotransporters and the size of the voltage-gated currents. We started by setting the DEs of K_i^E, Na_i^E and Cl_i^E of Equation 4.52 to zero. Next, we assume that all AMPA and GABA$_A$ receptors are closed at $t = 0$ and so, both r_A and r_G are initially zero. This leads to

$$\begin{aligned}
I_{Na}^{L,E} &= -I_{Na}^{T,E} - 3\delta I_p^E, \\
I_K^{L,E} &= -I_K^{D,E} + 2\delta I_p^E \ - FJ_{KCL}^I, \\
I_{Cl}^{L,E} &= -I_{Cl}^{G,E} + FJ_{KCL}^E.
\end{aligned}$$

Solving this equations leads to the values of P_{Na}^L, P_K^L and P_{Cl}^L, required for equilibrium of the system. Thereby, the following constraints have to be kept in mind: $P_{Na}^L > 0$, $P_K^L > 0$ and $P_{Cl}^L > 0$. The outcome is the same for the inhibitory population as the initial conditions are similar to those of the excitatory population.

D | Additional background information: cell biology

We start by providing a general introduction to the structure of the human brain and neurons. Next, we provide more background information about cell biological topics used in this research. We focus on neural activity and the contributing role of ion channels, NKA, KCL cotransporter KCC2 and transmembrane receptors AMPA and GABA.

D.1 Introduction to human brain and neurons

The human brain contains approximately 10^{11} neurons and even more glial cells. Four different domains can be distinguished in the structure of neurons, namely: dendrites, cell body (or soma), axon and presynaptic terminals. Figure D.1 shows the structure of a typical neuron. All four parts play a specific role in the neural communication by sending signals to and receiving signals from other neurons. The neural information flows from the dendrites to the cell body to the axon. There it is passed on to target cells via synapses. A synapse contains the presynaptic terminal, the postsynaptic membrane (of the target cell) and the synaptic cleft (space between two cells)[9].

The intra- and extracellular solution of a neuron are electroneutral. However, a potential difference across the neuronal membrane exists due to separation of charge near both sides of the membrane itself. This potential difference across the neuronal membrane is referred to as membrane potential. A neuron has a resting membrane potential of approximately -65 mV.

D.2 Nernst potentials

Transmission of electrical signals and propagation of signals depends on ionic currents through the neuronal membrane. Some ion channels, called leak channels, are opened in resting neurons. Permeable ions can cross the neuronal membrane via these channels which results in leak currents. Besides the leak currents, there are voltage-gated currents. A change in membrane potential near the voltage-gated channel can open or close the channel, thereby allowing or blocking ions to flow in or out of the cell[31]. Ions move through open membrane channels depending on the ion concentrations on both sides of the membrane and electrical potential gradients. Diffusion of ions happens down-gradient. However, neurons also contain impermeable anions. If positively charged ions diffuse out of the cell, the ICS has a net negative charge. Now an electrical potential gradient across the membrane is created due to accumulation of positive and negative charges on both sides sides of the membrane surface. This transmembrane potential results in attraction of positive ions to the negatively charged membrane interior and repulsion from the positively charged membrane exterior. The net-cross membrane current becomes zero when the

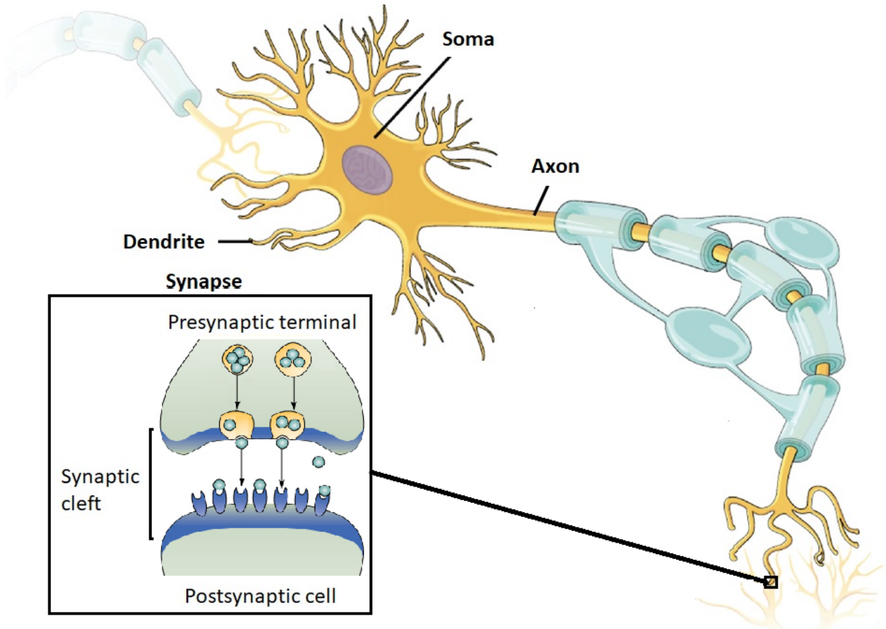

Figure D.1: **Structure of neuron**. The structure of the neuron can be divided into four domains: dendrites, cell body (= soma), axon and presynaptic terminals. The synapse exists of the presynaptic terminal, the postsynaptic membrane and the synaptic cleft. Here, signals are transmitted from one neuron to the target cell. Modified figure from [51].

electrical potential gradient and the concentration gradient counterbalance each other and an equilibrium is reached. This point is called the Nernst equilibrium potential [31]. The intracellular and extracellular ion concentrations and the Nernst equilibrium potentials of typical mammalian neurons are listed in Table D.1.

D.3 Action potentials

Voltage-gated channels play a role during generation of action potentials. Action potentials are brief electrical impulses causing the membrane potential to rise by approximately 100 mV. When the membrane depolarizes, voltage-gated sodium channels open and sodium ions can enter the cell. This results in a rapid increase of the membrane potential. Shortly after, these channels close and voltage-gated potassium channels open. Potassium rushes out of the cell and the membrane potential drops quickly (repolarisation). The membrane potential even becomes slightly more negative than its resting potential as voltage-gated potassium channels close slowly. This is called after-hyperpolarisation.

Table D.1: **Ion concentrations and Nernst equilibrium potentials.** The intracellular and extracellular concentrations of typical mammalian neurons and the corresponding Nernst equilibrium potentials at a temperature of 37°C. Impermeant anions do not have an equilibrium potential as this is only applicable to permeant ions. $[X]$ denotes the concentration of ion X with $X \in \{Na^+, K^+, Cl^-, A^-\}$. Values from Izhikevich (2007) [31].

Ion species	Intracellular [X] (mM)	Extracellular [X] (mM)	Equilibrium potential (mV)
Sodium (Na$^+$)	5 to 15	145	61 to 90
Potassium (K$^+$)	140	5	-90
Chloride (Cl$^-$)	4	110	-89
Anions (A$^-$)	147	25	x

D.4 Neurotransmitters

During chemical synaptic transmission, neurotransmitters are released from the presynaptic terminal. These molecules bind to receptors of the postsynaptic cell after diffusion across the synaptic cleft. Due to the generation of ion flow, this process results in a change in the membrane potential at the side of the postsynaptic cell, called a postsynaptic potential (PSP). Excitatory neurotransmitters generate an inward current across the membrane which leads to depolarization. A PSP produced this way is called an excitatory postsynaptic potential (EPSP). An inhibitory postsynaptic potential (IPSP) is created by inhibitory neurotransmitters. They generate an outward current leading to a more negative membrane voltage (hyperpolarization). If the incoming signals lead to significant PSPs, amplification of the signals by voltage-gated channels can occur and action potentials are generated[31]. The fast EPSPs in the brain are mediated by AMPA receptors. These receptors have a rise time between 0.4 and 0.8 ms in cortical pyramidal cells and a decay time constant of approximately 5 ms[38]. AMPA receptors have an almost equal permeability to both potassium and sodium. This result in an equilibrium potential near 0 mV as it is driven equally towards the Nernst potential of potassium (-90 mV) and sodium (60 to 90 mV)[31]. GABA$_A$ receptors mediate the fast IPSP and are sensitive to chloride. The equilibrium potential of the GABA$_A$ receptors is thus equal to the Nernst equilibrium potential of chloride[31,34].

D.5 Types of neurons

We focused on pyramidal neurons and interneurons in this research. Pyramidal neurons are the principal excitatory neurons in the cortex. These cells receive both excitatory and inhibitory input. Interneurons are mostly inhibitory, although there exist excitatory interneurons as well. Approximately 20-30% of the cortical neurons are inhibitory neurons. These neurons connect to pyramidal cells and other interneurons. Moreover, they play an important role in the regulation of the dynamics of neuronal networks[53,69].

E | General principles of neural mass model

Conversion of the average membrane potentials and average pulse densities is performed with two operators: the synaptic response and the potential-to-rate function. Figure E.1 shows a schematic overview of the conversion operators of a neural mass and the order of usage.

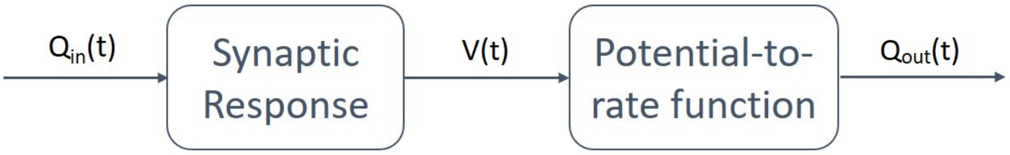

Figure E.1: **Schematic overview of the conversion operators of a neural mass model.** The synaptic response transforms the mean pre-synaptic firing rate Q_{in} into an average membrane potential $V(t)$. The potential-to-rate function, or activation function, converts the average membrane potential into a mean firing rate Q_{out}.

The mean pre-synaptic firing rate $Q_{in}(t)$ transforms into an average post-synaptic potential $V(t)$ by linear convolution with the impulse response of the synapses:

$$V(t) = h * Q_{in}(t), \tag{E.1}$$

where $*$ denotes the convolution operator and h denotes the impulse response.

Characteristics of the impulse response are a rapid rise and a slow decay. Common choices for $h(t)$ are a difference of exponentials (h_d) or the α-function (h_α):

$$\begin{aligned} h_d(t) &= \left(\frac{1}{\alpha} - \frac{1}{\beta}\right)^{-1} \left[e^{-\alpha t} - e^{-\beta t}\right] H(t), \\ h_\alpha(t) &= \alpha^2 t e^{-\alpha t} H(t), \end{aligned}$$

for $t \geq 0$, where $\alpha > 0$ and $\beta > 0$ are the synaptic decay and rise rate, respectively. In case $\alpha = \beta$, we get h_α instead of h_d. $H(t)$ denotes a Heaviside step function. Figure E.2A shows an example of the impulse response function h_d.

The differential equation (DE) corresponding to the impulse response function of the convolution (Equation E.1) is:

$$\left(1 + \frac{1}{\alpha}\frac{d}{dt}\right)\left(1 + \frac{1}{\beta}\frac{d}{dt}\right) V = Q_{in}.$$

The second operator, the potential-to-rate function $S(V)$, transforms the average membrane potential to a mean firing rate. This function is also known as the activation function. It is a non-linear function and typically, has the following properties:

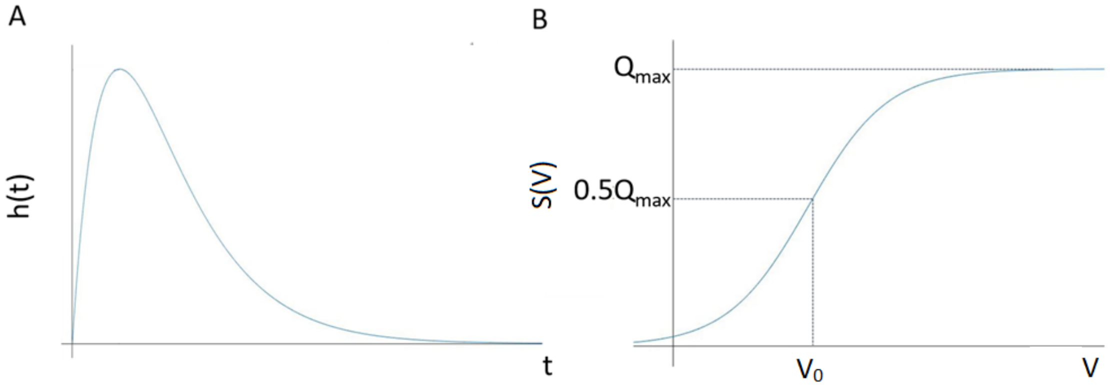

Figure E.2: **Examples of both conversion operators of a neural mass model**. A. Second order impulse response function $h_d(t)$. B. Sigmoid function $S(V)$ with Q_{max} the asymptotic maximal value and V_0 the potential at which half of the population fires. For $V = V_0$ we get $S(V_0) = 0.5Q_{max}$.

- It is non-decreasing, so $S'(V) > 0$.
- It converges to zero as $V \to -\infty$, so $\lim\limits_{V\to-\infty} S(V) = 0$.
- It is bounded from above by the maximum firing rate Q_{max}, so $\lim\limits_{V\to\infty} S(V) = Q_{max}$.

The population firing rate is often modelled by a sigmoid function:

$$S(V) = \frac{Q_{max}}{1 + e^{r(V_0 - V)}}, \tag{E.2}$$

where r is the slope of the sigmoid and V_0 is the potential at which half of the population fires. An example of this sigmoid function is plotted in Figure E.2B.